Chem Soc Rev

REVIEW ARTICLE

View Article Online
View Journal | View Issue

Cite this: *Chem. Soc. Rev.*, 2025, **54**, 10654

Scanning probe microscopy of metal–organic coordination systems: characterization of monolayers, single crystals, discrete architectures

Antonino Cucinotta, Jack A. Davies, Kunal S. Mali * and Steven De Feyter *

Metal–organic coordination is omnipresent in a number of functional materials. Such systems are highly diverse in terms of their composition, complexity, and dimensionality. They include two-dimensional (2D) and three-dimensional (3D) structures ranging from monolayers of metal–organic coordination networks (MOCNs) physisorbed on solid surfaces, to crystalline metal–organic frameworks (MOFs), to discrete metallosupramolecular architectures (DMSAs). The use of these metal–organic materials in a wide variety of applications has been demonstrated, showing promise for their incorporation into emerging technologies. Several design strategies have been developed for the fabrication of MOCNs, MOFs, and DMSAs exhibiting a diverse array of structures, enabling precise control over their functional properties. As these strategies are designed at the molecular level, there has been considerable interest in the nanoscale resolution imaging of metal–organic coordination systems across different length scales. This review provides a glimpse of recent progress in the nanoscale characterization of metal–organic coordination systems using scanning probe microscopy (SPM). Systems ranging from surface-confined MOCN monolayers, to MOF thin films, surfaces of MOF single crystals, and DMSAs are discussed. Specifically, we discuss the contribution of scanning tunneling microscopy (STM), atomic force microscopy (AFM), and techniques that combine SPM with spectroscopic methods to obtain high-resolution chemical information, toward the nanoscale structural characterization of multinuclear metal–organic assemblies.

Received 10th July 2025

DOI: 10.1039/d4cs01303d

rsc.li/chem-soc-rev

Division of Molecular Imaging and Photonics, Department of Chemistry, KU Leuven, Celestijnenlaan 200F, 3001 Leuven, Belgium. E-mail: kunal.mali@kuleuven.be, steven.defeyter@kuleuven.be

Antonino Cucinotta

Antonino Cucinotta obtained his MSc in chemistry at the Università degli Studi di Messina (Italy) in 2020. In 2025, he obtained his PhD at KU Leuven (Belgium), under the supervision of Prof. Steven De Feyter and Dr. Kunal S. Mali. His doctoral research focused on the development of new strategies for the on-surface fabrication of metal–organic coordination networks and metal–organic frameworks and the investigation of their formation, growth, structure, and properties in two and three dimensions using scanning probe microscopy at the liquid–solid interface. He is currently a postdoctoral researcher in the De Feyter group.

Jack A. Davies

Jack A. Davies completed his PhD in 2022, at the University of Cambridge, UK. This doctoral work, under the supervision of Prof. Jonathan R. Nitschke, elucidated design principles underpinning the formation of discrete metal–organic architectures. Since joining the group of Prof. Steven De Feyter at KU Leuven in 2023, his research has focused on investigating the local structure in extended two-dimensional metal–organic coordination networks, primarily employing scanning probe microscopy to do so.

1. Introduction

The coordination bond represents a highly versatile interaction, playing a pivotal role across various domains. The coordination of organic ligands to metal ions is ubiquitous in natural systems, with numerous proteins employing metal binding to perform diverse functions such as structural support, storage, electron transfer, dioxygen binding, and catalytic activity.[1,2] However, metal ions are also prevalent pollutants in natural environments, and their complexation by organic ligands serves as an effective strategy for sequestration.[3–5]

Over the past decades, the field of coordination chemistry has advanced significantly from the study of simple metal complexes, and coordination bonds have been incorporated into the design and synthesis of novel materials. Directionality is a key characteristic of coordination bonds, and the specific coordination geometries of d- and f-block metals enable the construction of scaffolds with well-defined architectures. By combining metal ions or clusters with a diverse array of organic ligands, a wide variety of structures can be formed with both extended and discrete structures. Examples of such structures include metal–organic frameworks (MOFs), surface-confined metal–organic coordination networks (MOCNs), and discrete metallosupramolecular architectures (indicated as DMSAs in this review).

MOFs are self-assembled polymeric coordination compounds consisting of metal ions or clusters connected by organic ligands, exhibiting exceptional porosity and tunable pore sizes.[6–13] Although early reports on coordination polymers date back to the mid-20th century, the synthesis of the first crystalline MOFs in the late 1980s and 1990s marked a major breakthrough in coordination chemistry.[12,13] This milestone laid the foundation for reticular chemistry, a field dedicated to the design of porous crystalline materials stabilized by strong bonds between molecular building blocks.[14] Reticular chemistry also includes covalent organic frameworks (COFs), which are structurally analogous to MOFs but consist entirely of organic components linked by covalent bonds.[15] Hydrogen-bonded organic frameworks (HOFs) represent porous reticular frameworks comprising ordered arrangements of organic linkers connected *via* hydrogen bonds, although they frequently derive additional stability from other complementary non-covalent interactions.[16] In contrast to these designed reticular frameworks, zeolites are purely inorganic porous materials, which are characterized by relatively small pore sizes (<2 nm).[17]

A wide range of MOFs has been synthesized through the strategic combination of various metal centers and organic linkers.[8] Notably, d-block transition metals offer predictable coordination geometries dictated by their electronic configuration, which result in a diverse array of framework geometries. This structural diversity is further expanded with the incorporation of f-block elements, particularly lanthanides, which typically form coordination complexes with high coordination numbers. These lanthanide-based complexes are generally labile, and their coordination chemistry is considered to be predominantly governed by electrostatic interactions.

In coordination polymers, the metal centers are typically referred to as primary building units (PBUs), which are linked by organic ligands to form the material's scaffold. Secondary building units (SBUs) are metal-containing clusters or coordination complexes that serve as nodes in the extended framework, connecting to organic linkers with a predictable geometry.[18–20] The connectivity within the SBUs provides a stable scaffold, enhancing both the thermal and mechanical robustness of the overall network.[19,20] Moreover, the use of SBUs in MOF design and synthesis enables the predictability of the final structure due to their well-defined geometry and connectivity.[18,19]

MOF classification may take into account several structural features, such as the dimensionality of the SBUs or of the crystals, among others.[20,21] For the scope of this review, it is convenient to classify MOFs according to the connectivity of the building blocks. Therefore, MOFs which exhibit coordination bonds that extend in two dimensions are categorized as two-dimensional (2D) MOFs, while those with a periodic

Kunal S. Mali

Kunal S. Mali obtained his PhD in 2008 from the University of Mumbai in India, while working at the Bhabha Atomic Research Centre, where he investigated polymer colloids and ionic liquids using time-resolved fluorescence spectroscopy. He then joined the group of Prof. Steven De Feyter at KU Leuven as a postdoctoral researcher, focusing on molecular self-assembly on surfaces studied by scanning tunneling microscopy. His current research interests span covalent and supramolecular chemistry at solid surfaces, explored using advanced scanning probe microscopy techniques with high spatial and chemical resolution. He is presently a research manager at KU Leuven.

Steven De Feyter

Steven De Feyter is a professor at KU Leuven, Belgium. He earned his PhD at KU Leuven in 1997 and subsequently pursued postdoctoral research at Caltech. His team explores both non-covalent, via self-assembly, and covalent modification of graphite and 2D materials, including graphene and transition metal dichalcogenides. A central focus of the work is the on-surface synthesis of covalent organic frameworks (COFs) and metal–organic frameworks (MOFs). At the core of the research lies high-resolution scanning probe microscopy, which enables real-space nanoscale characterization, with particular emphasis on processes occurring at the liquid–solid interface.

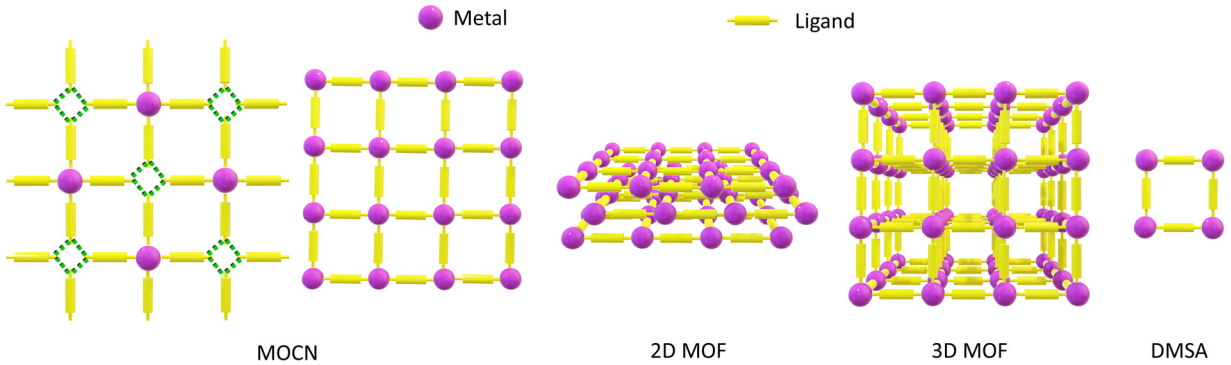

Scheme 1 Schematic representation of the classification of metal–organic coordination systems discussed in this review. MOCNs: in this review, they include surface-supported 2D coordination networks stabilized by other directional supramolecular interactions, indicated by the green dashed lines, in combination with metal–ligand coordination. A porous MOCN featuring only coordination bonds within its structure can be conceptually regarded as a 2D MOF monolayer. 2D MOFs: MOFs exhibiting coordination bonds extending in two dimensions. 3D MOFs: MOFs exhibiting coordination bonds extending in three dimensions. Both 2D and 3D MOFs can be fabricated in the form of thin films, with the former presenting characteristic layered structures. DMSA: coordination compounds containing a specific number of metal ions and organic ligands that do not have extended structures.

arrangement of coordination bonds throughout all three spatial dimensions are classified as three-dimensional (3D) MOFs (Scheme 1).[8,10,22,23] MOFs can be fabricated as thin films with thicknesses ranging from several to a few hundred nanometers. Some 2D MOF thin films exhibit characteristic layered structures.[22,24]

The uniform pore distribution, exceptional surface area, and incorporation of metal centers account for the extensive applications of MOFs in therapeutics and catalysis,[25–27] as well as in gas storage,[26,28,29] separation processes,[26,30,31] sensing technologies,[26] and charge transport and storage.[26,32–34] When deposited onto solid surfaces, MOF thin films are more easily integrated into functional devices.[35–37]

MOFs are the porous subclass of coordination networks.[6] However, in this review, the term MOCNs is used in reference to surface-confined metallosupramolecular monolayers extending in 2D (Scheme 1).[38] We include in this definition 2D assemblies held together purely by metal–ligand coordination, as well as those held together by coordination bonds in combination with other directional interactions such as hydrogen bonding. MOCNs are examples of self-assembled molecular networks (SAMNs)—surface-confined supramolecular architectures consisting of individual molecules held together by various supramolecular interactions. While a variety of SAMNs containing coordination bonds in their scaffold has been reported, the term MOCN is mainly used specifically in reference to SAMNs featuring metal coordination in two dimensions.[39] Surface-confined MOCNs featuring porous structures are indicated as porous MOCNs.

A distinctive feature of surface-confined MOCNs is their propensity toward planar coordination geometries, potentially resulting in coordination sites at metal centers that remain either unoccupied or occupied by labile ligands, such as solvent molecules.[38] These open reactive sites can be utilized for catalytic or sensing applications, leveraging the unique electronic and magnetic properties of these materials.[40–43] Additionally, given their crystalline nature, surface patterning with MOCNs presents a convenient method for templating the supramolecular organization of guest molecules in periodic arrangements.[44]

We distinguish between MOFs and MOCNs due to the structural differences arising from surface confinement. Crystals grown in 3D can be categorized into 230 3D space groups, whereas only 17 2D plane groups are possible for monolayered crystals.[45] Additionally, substrate–adsorbate interactions can stabilize 2D structures that have no direct bulk counterparts, and analogous precursors can originate different structures from in-solution and on-surface processes. Furthermore, surface adsorption is associated with reduced symmetry in 2D crystals with consequences on the chirality of the assemblies, as will be discussed in the related sections. Therefore, surface-confined MOCNs are not necessarily the single-layered counterparts of 2D and 3D MOFs, and it is important to maintain a distinction between these two classes of materials.

Self-assembled materials that do not have extended structures can also be realized, including DMSAs (Scheme 1). Through the combination of carefully selected metal ions and ligands, discrete metal–organic architectures, consisting of a given number of metal ions and ligand units, can be selectively assembled, instead of extended frameworks.[46–49]

Given the inherent structural differences between MOFs, MOCNs, and DMSAs, these materials are studied using different techniques. The characterization of MOF morphology involves describing their crystal structure, size, shape, and porosity. To obtain a comprehensive understanding of MOF materials, a combination of complementary techniques is required.[50–52] Due to their often crystalline nature, MOFs are typically characterized using X-ray diffraction techniques such as single-crystal X-ray diffraction (SC-XRD) and powder X-ray diffraction (PXRD). These techniques provide space- and time-averaged information about the unit cell of crystal samples with atomic resolution.[53–55] Scanning electron microscopy (SEM) and transmission electron microscopy (TEM) are valuable for investigating the shape of MOF particles. Additionally, the latter allows for nanometer or sub-nanometer resolution characterization on a

particle-by-particle basis. This technique requires the samples to be typically under 200 nm thin and sufficiently resistant to the high-energy electron beam.[56–58] The development of low-dose techniques and liquid cell TEM (LCTEM) holds promise for studying MOFs under dynamic conditions.[59]

Although the pore size can be calculated from the crystal structure determined by the aforementioned techniques, the accurate measurement of pore size distribution, surface area, and accessible volume is achieved by recording adsorption and desorption isotherms.[60] Additionally, the hysteresis observed between adsorption and desorption isotherms can be an indirect indication of the occurrence of a reversible framework transformation upon guest adsorption, a characteristic feature of so-called third-generation MOFs.[61,62]

To elucidate the structure–function relationship in MOFs, examine their responsiveness to external stimuli, and directly visualize structural changes and phase transitions, utilizing local, spatially-resolved techniques is imperative. As previously discussed, LCTEM constitutes a promising methodological approach toward this objective. Ideally, minimally invasive analytical techniques that facilitate the characterization of material surfaces with molecular and sub-molecular resolution in real space would complement these TEM techniques.

As stated above, MOCNs are conceptually similar to MOFs. However, the aforementioned structural differences between the two classes of materials render structural characterization of MOCNs using analogous methods to those used for (bulk) MOFs challenging. Therefore, alternative techniques that enable molecular-resolution imaging of surface-confined monolayers are needed for investigating MOCNs.

It is common practice that the structures of DMSAs are elucidated using a combination of nuclear magnetic resonance (NMR) spectroscopy, mass spectrometry (MS), and SC-XRD.[63] Solid-state structure determination by SC-XRD methods can become challenging when a metal–organic species exists as a mixture of distinct isomers. Techniques capable of structurally characterizing individual species in a mixture would thus be valuable in the thorough characterization of mixtures containing structurally different individual components.

As discussed, several challenges remain in the characterization of metal–organic systems, despite the wide range of techniques available. These include the need for nanoscale local characterization, also under dynamic experimental conditions and in the presence of external stimuli. Particularly in the case of MOCNs, the ability to image material surfaces with (sub)-molecular resolution is also required. To this end, scanning probe microscopy (SPM) offers a set of low-invasive, surface-sensitive characterization techniques that may provide complementary information to the insights obtained with the methods described above. SPM techniques also offer the capability to conduct imaging procedures in liquid environments and under dynamic experimental conditions.[64,65]

These techniques include scanning tunneling microscopy (STM) and atomic force microscopy (AFM). STM enables the analysis with (sub)-molecular resolution of single molecular species and extended single-layered (or few-layered) assemblies adsorbed on conductive surfaces.[66,67] While AFM is also suitable for the study of atom-thick species on solid substrates, it is widely employed for the study of the surface of thicker samples, including thin films and nanoparticles.[68–70] Both techniques can be operated under ultra-high vacuum (UHV) and ambient conditions (at the air–solid and liquid–solid interface), allowing for studies under dynamic conditions, as well as in the presence of external stimuli. In any instance, the firm immobilization of samples on solid substrates is essential for implementing SPM investigations.

Early works on the use of SPM for the characterization of metal–organic coordination systems date back to the early 2000s. Pivotal UHV-STM studies targeted the investigation of coordination complexes[71,72] and MOCNs adsorbed on solid substrates,[39,73] exploring ligand control strategies[73] and designing chiral networks that incorporated coordination bonds.[74] The fabrication of extended surface-confined MOCNs with large pore sizes demonstrated the stabilizing role exerted by solid substrates.[75] Works targeting the STM characterization of coordination systems, including DMSAs, under ambient conditions emerged almost in parallel with UHV studies.[76–78] However, MOCNs fabricated at the liquid–solid interface were reported 10 years later than UHV analogues,[79] and only recently have in-depth investigations into the structural control and the design of chiral MOCNs at the liquid–solid interface been carried out.[80,81] Initial AFM studies on MOF surfaces targeted the elucidation of nucleation and growth processes through the imaging of surface features such as defects and step heights.[82,83] The use of functionalized substrates for MOF thin films and crystals growth was a significant contribution to the development of the field, as will be discussed in Section 4.[84] In recent years, molecular-resolution AFM imaging of MOF surfaces was achieved,[69] and the mechanism of complex surface dynamics was elucidated.[68]

This review examines the current status and methodological challenges associated with the characterization of MOCNs, MOFs, and DMSAs *via* SPM techniques, with particular emphasis on elucidating molecular structures, local features, and dynamic processes. Initially, the fundamental operating principles of the main SPM techniques will be briefly described (Section 2). Following this, a critical description of the characterization of MOCNs, MOFs, and DMSAs transversal to the length scale (monolayers, thin films, and crystal surfaces) performed using SPM will be provided. The experimental conditions used for materials preparation and the SPM techniques suitable for their characterization often vary based on the class of the material. In this review, categorization into three sections (Sections 3–5) is thus on the basis of material class. The characterization of MOCNs using STM in UHV and at the liquid–solid interface will be reviewed in Section 3. The characterization of MOF thin films and single crystals using AFM will then be discussed in Section 4. Finally, SPM characterization of self-assembled networks of DMSAs, and the use of SPM for the structural characterization of the metallosupramolecules themselves, will be addressed in Section 5. Throughout the review, the inherent challenges associated with achieving molecular-resolution imaging of MOCNs, MOFs, and DMSAs

will be emphasized, and a perspective on the future developments in SPM characterization of these materials will be presented in the conclusions of this review.

2. SPM techniques

As discussed previously, MOFs, MOCNs, and DMSAs can be effectively characterized using SPM. STM and AFM have emerged as foundational SPM techniques for characterizing the aforementioned classes of materials. These techniques rely on the use of a physical probe that scans over the surface of the materials, providing information about their structure arising from the probe–sample interactions. One limitation of STM and AFM is their lack of chemical sensitivity, which can be overcome by combining them with spectroscopic techniques. In this regard, the combination of AFM with infrared spectroscopy (AFM-IR) has recently been applied to the study of MOFs.[85] In this section, we present a concise overview of the key operational aspects of these analytical techniques that are relevant for the characterization of MOCNs, MOFs, and DMSAs. More detailed technical details can be found in the references contained in this section.

2.1 Scanning tunneling microscopy

STM operates on the principle of quantum mechanical tunneling. In an STM setup (Scheme 2(a)), a sharp conducting tip is positioned very close (<1 nm) to a conducting substrate, and a bias voltage is applied between the two. Electrons tunnel through the gap, generating a measurable current. This tunneling current is exponentially dependent on the tip-sample distance, allowing for extraordinary vertical resolution down to picometer scales. The current is also proportional to the local density of states (LDOS) of the sample surface, enabling STM to provide information not only about the topography but also about the electronic structure of the sample.[86–90] During STM measurements, the tip raster-scans the surface, as illustrated in Scheme 2(b), and a signal is recorded. In constant height mode, the tip-sample distance is maintained constant, and the variation in tunneling current is measured (Scheme 2(c)). In contrast, in constant current mode, the tip-sample distance varies to maintain the tunneling current constant (Scheme 2(d)). In scanning tunneling spectroscopy (STS), current–voltage measurements are performed to quantitatively study the electronic structure of the surface.[91]

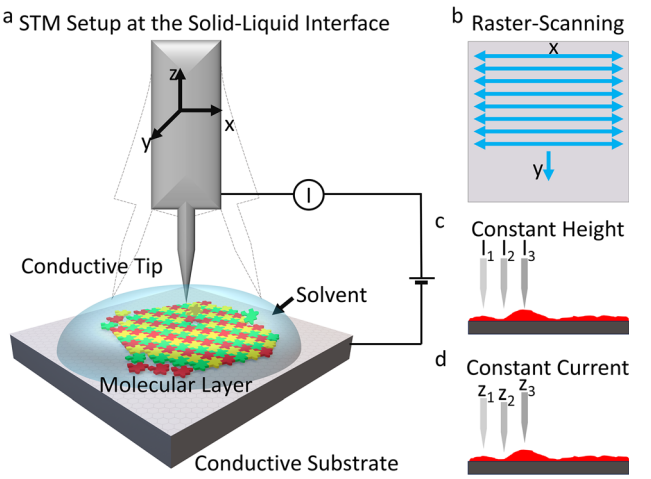

Scheme 2 Representation of STM at the liquid–solid interface. (a) Machine setup. (b) Illustration of the tip movements. (c), (d) STM imaging modes.

In STM performed at the liquid–solid interface, the solvent permittivity significantly influences the tunneling process. In polar solvents with high relative permittivity, such as water, an applied electric field induces molecular dipoles to orient parallel to the field, generating an induced electric field that opposes the external one. Furthermore, if the solvent is electrochemically active, the applied bias potential may trigger redox reactions that contribute to a background current, which can potentially dominate the tunneling current. Therefore, apolar solvents are selected, and low-volatile solvents are preferred to reduce solvent evaporation during imaging.[92]

Typical substrates employed in UHV processes include gold, copper, and silver surfaces, whereas gold and highly oriented pyrolytic graphite (HOPG) are preferred for studies conducted in air and at the liquid–solid interface due to their chemical inertness under ambient conditions.[93]

UHV *vs.* in-solution methods. UHV conditions enable the investigation of a wide range of temperatures, which is relevant for studying temperature-induced structural changes and thermal stability of the networks, whereas the solvent vapor pressure and boiling points determine the upper temperature limit in experiments carried out at the liquid–solid interface. The lower limit is governed by the solvent melting point and the possibility of water condensation.

Nevertheless, MOFs are often fabricated using solution-based processes, in which the solvent is selected to enable control over crystal nucleation and growth, thereby determining the morphology of the products. MOCN fabrication and characterization at the liquid–solid interface offers the opportunity to gain molecular insights into the effect that different solvents play during the synthesis process directly in their growth solution. Moreover, as already stated, the liquid–solid interface is a dynamic environment, where *in situ* changes, including temperature-induced phase transitions and guest adsorption processes, can be monitored in real time for monolayers, thin films, and single crystals.

2.2 Atomic force microscopy

AFM overcomes STM's limitation of requiring conductive samples by measuring the forces between a sharp tip mounted on a cantilever and the sample surface. These interatomic forces, typically in the range of 10^{-8} to 10^{-9} N, follow the Lennard-Jones potential, and are attractive at longer distances due to van der Waals interactions and repulsive at shorter distances due to electrostatic repulsion and Pauli exclusion principle. As the tip raster-scans across the surface, cantilever deflections are detected by monitoring the reflection of a laser beam onto a position-sensitive photodiode (Scheme 3).[88,89,94]

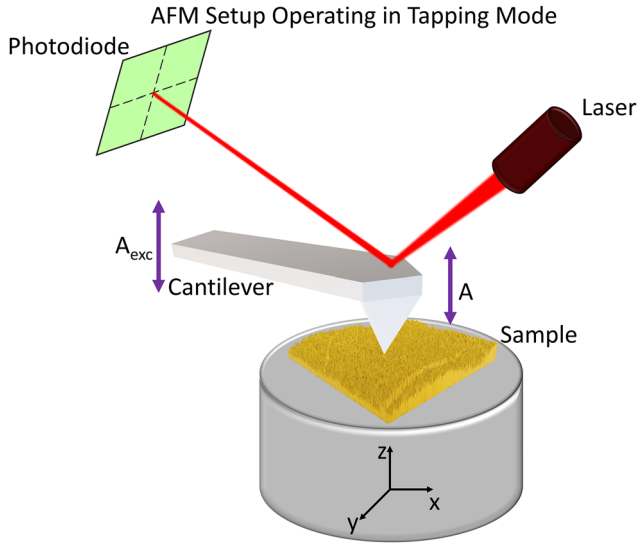

Scheme 3 Representation of the AFM setup operating in AM mode. A_{exc} represents the oscillation amplitude of the drive, whereas A is the oscillation amplitude of the cantilever.

AFM offers multiple operational modes: contact mode, where the tip directly interacts with the surface in the repulsive regime; amplitude modulation (AM) mode, where the cantilever oscillation is driven at a constant excitation frequency near resonance and the amplitude changes are measured; and frequency modulation (FM) mode, which maintains the cantilever oscillation continuously at its resonance frequency through a phase-locked loop. Non-contact AFM (nc-AFM) is a special case of AFM that operates with sufficiently large amplitudes to avoid entering the repulsive regime.

AFM imaging at the liquid–solid interface enables *in situ* studies of dynamic processes, including crystallization, adsorption, and conformational changes in their native solution environments with molecular resolution.

2.3 Combining SPM with spectroscopy techniques

While not yet extensively employed, the use of AFM-IR in the field of metal–organic coordination systems is emerging. It represents a powerful integration of AFM with IR spectroscopy, overcoming the diffraction limit of conventional IR microscopy and the lack of chemical sensitivity of SPM. This technique often measures the local photothermal expansion caused by the absorption of mid-IR laser pulses, transduced by the AFM cantilever. When a wavelength-tunable IR laser pulse illuminates the sample region beneath the AFM tip, absorption leads to thermal expansion, causing the cantilever to oscillate with an amplitude proportional to the absorption coefficient (Scheme 4). Both "ringdown" detection (recording the cantilever oscillation after excitation by a single pulse) and resonance-enhanced detection (synchronizing the laser pulse repetition rate with a cantilever resonance frequency) are employed, with the latter dramatically enhancing sensitivity.[95,96] Further operational details of AFM-IR, including discussion of the different available modes, have been recently reviewed.[97]

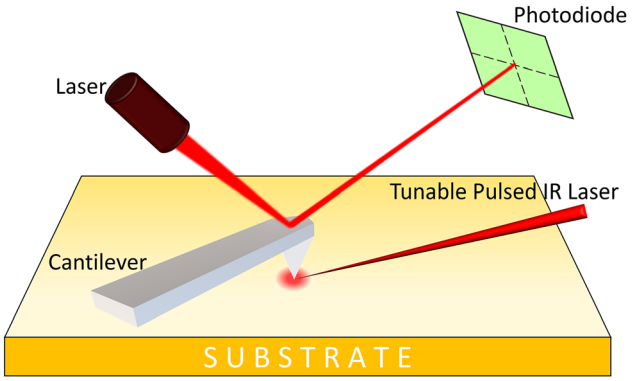

Scheme 4 Illustration depicting AFM-IR.

AFM-IR achieves chemical mapping with spatial resolution of 10–20 nm,[95] far beyond the diffraction limit of conventional IR microscopy, enabling the nanoscale investigation of chemical composition, molecular conformation, and polymorphic states across diverse research fields including polymer science, biology, and materials science.

Another technique which can provide very high-resolution chemical information for metal–organic materials is synchrotron X-ray STM (SX-STM). In SX-STM, the STM tip acts as a detector for both photoejected electrons and the tunnelling current modulated by the absorption of X-rays.[98]

3. STM characterization of MOCNs

Surface-confined MOCN monolayers are typically obtained through the self-assembly of precursors in UHV conditions or at the liquid–solid interface.[38,99] Several reviews have been published describing the various metal–organic architectures that can be fabricated on surfaces, detailing the variety of lattice geometries and electronic properties, investigated using mainly UHV-STM.[38,100–105] Surfaces exert a significant influence on determining the outcome of the self-assembly process.[75] In UHV, the formation of crystalline structures is governed by a balance between intermolecular and molecule–substrate interactions.

Although rarer, MOCN synthesis and characterization at the liquid–solid interface have also been reported. Interactions between solvent molecules and the substrate, as well as between solvent and solute, actively modulate self-assembly processes at liquid–solid interfaces.[93,106–110] The interrelated and occasionally competing intermolecular and molecule–substrate interactions, as well as interactions involving solvent or guest molecules, may facilitate the formation of distinct polymorphs on different substrates and/or when a different solvent is employed.[107,108,111–113]

In this section, we analyze the strategies for imparting structural control in MOCNs. Furthermore, investigation of substrate effect, phase transitions, stimuli-responsiveness, chirality, and network porosity will be discussed. While the selection of papers presented here does not aim to provide an exhaustive collection of works carried out on coordination

systems on surfaces, it showcases how molecular-resolution imaging of local features achieved *via* STM characterization under UHV and at the liquid–solid interface provides unique insights into our understanding of MOCNs.

3.1 MOCNs fabricated and characterized in UHV

MOCN structures synthesized under UHV using different functional groups, including carboxylates, pyridyls, nitriles, and carbonyl-containing ligands, have been explored in the literature.[114–118] Organic molecular beam deposition (OMBD) is a common technique used to fabricate monolayers containing small organic molecules. In this method, sublimated molecules either react with metal surface adatoms or with metal species generated by electron beam heating in a UHV chamber.[119] This approach enables precise control over the deposition process, as both the molecular concentration and deposition rate can be finely tuned. However, some building blocks may have limited stability during sublimation.

Early works relied on the use of UHV-STM to explore: novel supramolecular architectures obtained through metal coordination-induced phase transitions,[120,121] the fabrication of cavities with tunable size,[75,122] and the *in situ* examination of coordination dynamics.[72] Following these foundational works, the field evolved to the study of surface-confined MOCNs aimed at elucidating their structure, the effect of experimental parameters, and the organizational properties of the assembly. Structural characterization enables structures to be distinguished based on the connectivity of the metal and ligand building blocks, and for their local chirality to be assigned. Experimental parameters, including the concentration, the temperature, and the choice of substrate, are shown to directly influence the outcome of the self-assembly process and the stability of the resulting networks. Leveraging on these insights, a high degree of control during the fabrication of surface-confined MOCNs is possible, and the high spatial resolution of STM enables different phases to be distinguished. Furthermore, quantitative information on the crystallinity of the networks can be obtained. Finally, the structural variability accessible in surface-confined MOCNs, and revealed by STM, is associated with functional variability. These aspects are discussed below.

Direct visualization of the connectivity of the building blocks. The fabrication of extended crystalline networks often requires screening and optimization of various experimental parameters to obtain the desired architectures. Different coordination geometries can be favored for different metal ions; on the other hand, a given metal ion may display a variability in preferred coordination geometry under different experimental conditions. Both instances lead to networks with different structures. In addition, different ligands can promote different coordination geometries around the same metal center.[123] Additionally, ligand control has been demonstrated to be critical to obtain defect-free networks.[124] Different networks or amorphous structures can also be formed through control of metal and ligand concentrations.[125]

The use of polytopic ligands carrying a different number of analogous coordinating groups also allows the synthesis of MOCNs with different crystal structures.[126] Ligands with analogous core structures and different peripheral functional groups have been shown to form different architectures upon metal coordination on surfaces.[127] Pre-organization of the ligands on the surface *via* supramolecular interaction is a useful strategy to readily access crystalline structures.[128]

Exotic phases, such as Kagome lattices, have also been fabricated using metal–organic coordination.[115,129–132] Moreover, the use of f-block metals in MOCN synthesis expands the range of accessible coordination geometries, enabling the design of networks with higher coordination numbers at the metal nodes and distinct structural properties. Several examples have been reported that make use of lanthanides,[104,105,127,133–135] whereas only discrete actinide complexes have been studied.[136]

A particularly striking example of structural control in MOCN fabrication is demonstrated by quasicrystalline (QC) coordination networks, which are ordered structures lacking translational symmetry. Through precise stoichiometric control of Eu centers and ditopic linear *para*-quaterphenyl-dicarbonitrile (**QDC**) molecular linkers (Fig. 1(a)) on Au(111) surfaces, 2D metal–organic quasicrystals exhibiting dodecagonal symmetry

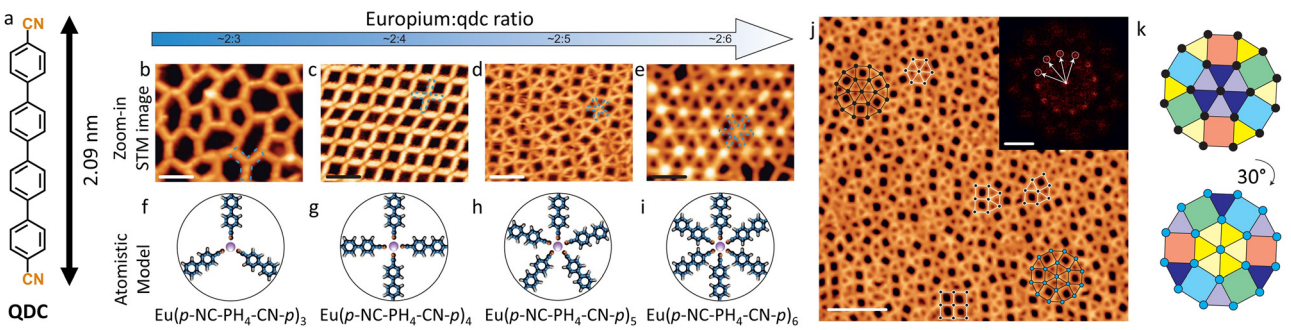

Fig. 1 Random tiling in QC-MOCNs. (a) Molecular structure of ligand **QDC**. (b)–(e) High-resolution STM images of the distinct Eu-**QDC** MOCNs fabricated by controlling the Eu : **QDC** stoichiometric ratios and (f)–(i) molecular models of the corresponding coordination geometries. Scale bar: 5 nm. (j) Large-scale STM image of the ddQC structure observed at Eu : **QDC** 2 : 5 stoichiometric ratio. Inset: 2D-FFT depicting the 12-fold symmetry of the network. (k) Different orientations with respect of the surface of the square-triangle tessellation in the dodecagonal tiling. Adapted with permission from ref. 137. Copyright©2016, Springer Nature Limited.

were successfully synthesized (Fig. 1).[137] This breakthrough achievement utilized the large and flexible coordination sphere of lanthanide centers to generate three-coordinated, four-coordinated, five-coordinated, and six-coordinated vertices by controlling the Eu : **QDC** stoichiometric ratio (Fig. 1(b)–(i)). Notably, a random square-triangle tessellation, featuring simultaneous four-coordinated, five-coordinated, and six-coordinated coordination geometries, with quasiperiodic order, was obtained at an Eu : **QDC** stoichiometric ratio of approximately 2 : 5, as shown in Fig. 1(d), (j) and (k). The formation of this dodecagonal quasicrystal (ddQC) structure was facilitated by the careful balance of adlayer–substrate interactions and entropic surface tessellation effects. UHV-STM characterization revealed a nanoporous structure with 12-fold fast Fourier transform (FFT) symmetry (Fig. 1(j)), representing a distinct manifestation of quasicrystallinity in surface-confined MOCNs. This work not only expands the structural diversity achievable through metal–organic coordination but also introduces f-block elements into QC architectures, opening pathways for functional surface nanoarchitectures that combine quasiperiodic order with the unique properties of lanthanide centers.

These examples demonstrate that spatially-localized imaging provided by STM enables visualization and distinction of such different geometries.

Assigning local chirality. Molecules that do not have any chiral centers can become chiral once adsorbed on a surface.[138,139] This occurs because interfaces lack an inversion center and a symmetry plane parallel to the surface, and these symmetry elements are broken in molecules upon adsorption. Notably, mirror planes perpendicular to the surface are not disrupted, so not all molecules become chiral upon adsorption. Surface adsorption is a symmetry-breaking process, and molecules that become chiral through this process are referred to as prochiral. In this case, each molecule represents a point chirality element on the surface.[140] Achiral molecules that remain achiral upon surface adsorption may form supramolecular assemblies through asymmetric intermolecular interactions, resulting in organizational chirality.[141,142] Additionally, another form of organizational chirality can arise from the relative orientation of the building blocks and the symmetry axes of the surface.[143,144]

The study of chiral expression and amplification in 2D coordination networks has gained significant attention due to potential applications in chiral resolution and enantioselective catalysis. The sub-molecular resolution imaging power of STM enables differentiation between opposite orientations of the ligands in chiral complexes adsorbed on a surface. The earliest examples of chiral coordination compounds on metal surfaces are complexes of 1,3,5-benzenetricarboxylic acid (trimesic acid, **BTC**) and Fe metal centers.[71,74,145] **Fe(BTC)$_4$** complexes are prochiral, and two opposite enantiomers are distinguished on the surface. Their investigation on Cu(100) represents the first direct observation of a chiral metal–organic coordination complex on a surface. Annealing of such structures at higher temperatures facilitates the hierarchical formation of extended chiral MOCNs featuring chiral nanocavities.

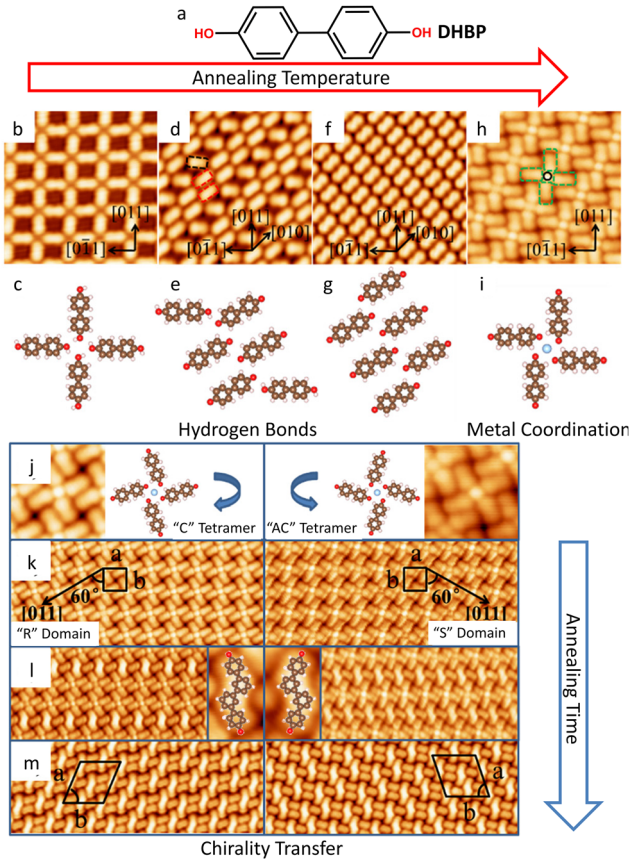

Fig. 2 Chiral **DHBP** assemblies on Ag(100). (a) Molecular structure of **DHBP**. (b)–(i) Representative high-resolution STM images of the temperature-induced phase transition in **DHBP** self-assembly and corresponding molecular structures. Annealing temperatures: (b), (c) 200 K; (d), (e) 300 K; (f), (g) 370 K; (h), (i) 490 K. Metal-coordinated chiral quartets form at 490 K (h)–(j). (k) Homochiral domains of **(DHBP)$_4$Ag** chiral quartets. (l) Mixed phase comprising of **(DHBP)$_4$Ag** chiral quartets and C–C-coupled dimers, obtained after annealing at 520 K for 10 minutes. The molecular structures of the dimers are shown in the insets. (m) Enantiomorphous assemblies of C–C-coupled dimers obtained after annealing at 520 K for 30 minutes. The image sizes are: (b), (d), (f), (h) 7 nm × 7 nm; (k)–(m) 19 nm × 7 nm. Adapted with permission from ref. 146. Copyright©2019 American Chemical Society.

Recent studies on the self-assembly of 4,4′-dihydroxybiphenyl (**DHBP**, Fig. 2(a)) on Ag(100) revealed that thermal annealing promotes phase transition in the hydrogen-bonded networks (Fig. 2(b)–(g)) and leads to coordination of the ligand to the surface adatoms at 490 K (Fig. 2(h) and (i)), resulting in the formation chiral windmill **(DHBP)$_4$Ag** quartets (Fig. 2(j)).[146] Enantiomeric quartets phase-separate into homochiral domains (Fig. 2(k)). Further annealing to 520 K for 10–30 minutes promotes C–C coupling between *trans*-positioned **DHBP** molecules in **(DHBP)$_4$Ag** quartets, and the chirality of the windmill complexes is transferred to the assembly of C–C-coupled dimers (Fig. 2(l) and (m)). A true MOCN is not formed here, but rather a SAMN of metal complexes. Stepwise annealing and the formation of chiral **(DHBP)$_4$Ag** metal complexes before the C–C coupling reaction are necessary to obtain an ordered arrangement of covalent dimers and the formation of chiral phases.

These works underscore how sub-molecular resolution imaging *via* STM enables differentiation of enantiomers and distinct chiral phases of assembled coordination complexes through direct visualization of their local structures. However, several critical gaps remain in our understanding of chiral MOCNs compared to the extensive body of work on non-metal-containing self-assembled supramolecular networks. Despite decades of research on purely organic chiral networks where phenomena such as chiral amplification, spontaneous resolution, and sergeant-and-soldiers effects have been extensively documented, analogous systematic studies in metal-coordinated systems have not yet been reported. Detailed investigations into chiral selection processes and the influence of metal coordination strength on chiral expression in UHV-fabricated MOCNs have not been described. More critically, the functional implications of chirality in these metal–organic networks, such as their potential for enantioselective adsorption of chiral guests or chiral recognition in general, remain largely unexplored. The field would benefit from systematic comparative studies examining how metal coordination influences chiral amplification mechanisms and from functional demonstrations of these chiral MOCNs in applications that exploit their inherent asymmetry, especially given that fixed binding geometries within the cavities of porous MOCNs could enhance chiral discrimination.

Nanoscale insights into the effect of concentration. In the above discussion, examples aimed at highlighting the possibility of local imaging with UHV-STM were presented. This feature is of primary importance for the direct investigation of dynamic changes. Such studies can provide insights into nucleation, growth mechanisms, error correction, and defect formation that are also directly relevant to understanding bulk MOF crystallization processes.

Tuning the concentration of the precursors is an effective strategy to promote the formation of different phases starting from the same building blocks.[125] A particularly instructive example of density-driven structural evolution is provided by the systematic study of **TPB**-Cu coordination networks on Au(111) as a function of molecular coverage.[147] By incrementally increasing **TPB** sublimation while maintaining Cu excess, the authors observed a remarkable sequence of structural transformations driven by what they termed ''intrinsic in-plane compression pressure'', as shown in Fig. 3. Starting from an open honeycomb network at low dosage (**TPB** concentration of 0.31 **TPB** per nm^2, Fig. 3(b) and (c)), progressive density increases led to the sequential formation of pentagonal networks (0.34 **TPB** per nm^2, Fig. 3(d) and (e)), rhombic structures (0.38 **TPB** per nm^2, Fig. 3(f) and (g)), and finally two phases labelled as mixed honeycomb-rhombic and triangular phases (0.59 **TPB** per nm^2, Fig. 3(h)–(k)). The corresponding molecular packing densities are indicated under the molecular models of each polymorph in Fig. 3. Most remarkably, this structural evolution was accompanied by a change in coordination chemistry: while at low **TPB** concentration only linear **TPB$_2$Cu** complexes are observed (Fig. 3(b)–(g)), at the highest ligand concentration trigonal **TPB$_3$Cu** complexes are also formed

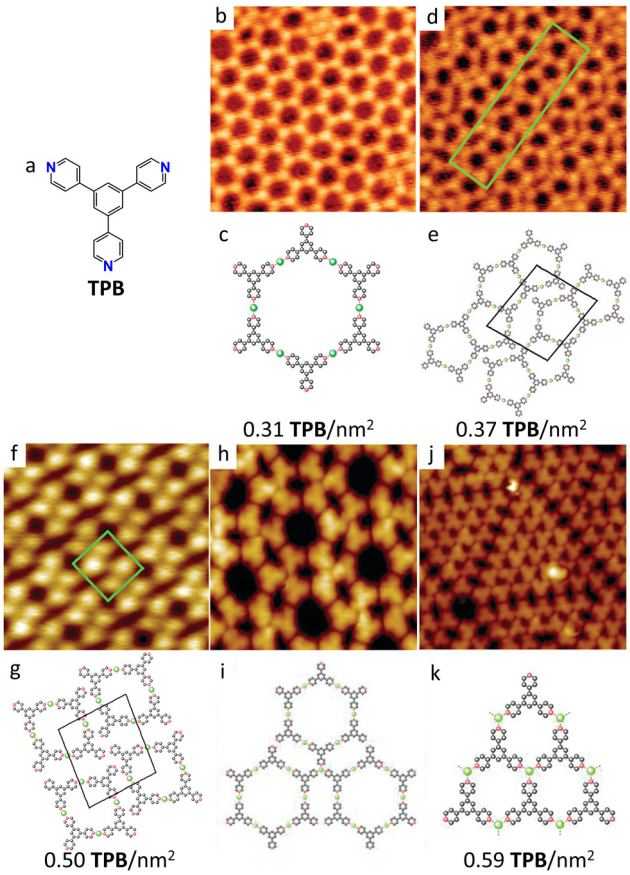

Fig. 3 **TPB-Cu** polymorphs on Au(111). (a) Molecular structure of **TPB**. (b), (d), (f), (h), (j) high-resolution STM images and (c), (e), (g), (j), (k) corresponding molecular models of the different **TPB-Cu** MOCN polymorphs formed on Au(111) at different **TPB** densities, reported underneath the models. Models color code: grey: carbon, red: nitrogen, green: copper. The molecular packing densities of Cu and **TPB** are: (b) 0.46 Cu per nm^2; 0.31 **TPB** per nm^2. (d) 0.50 Cu per nm^2; 0.37 **TPB** per nm^2. (f) 0.50 Cu per nm^2; 0.50 **TPB** per nm^2. (j) 0.59 Cu per nm^2; 0.59 **TPB** per nm^2. The image sizes are: (b), (d), (f) 20 nm × 20 nm. (h) 10 nm × 10 nm. (j) 15 nm × 15 nm. Adapted with permission from ref. 147. Copyright©2011 American Chemical Society.

(Fig. 3(h)–(k)), demonstrating that compression can alter the preferred coordination geometry of metal nodes.

This work provides valuable molecular-level insights into the role of ligand concentration as a control parameter in the synthesis of surface-supported MOCNs. The on-surface ligand concentration effects could be considered analogous to pressure effects in 3D MOF systems. The unique insights obtained by UHV-STM molecular resolution imaging may thus provide insights into bulk MOF-related dynamic phenomena.

Nanoscale insights into the effect of temperature. Temperature is a key parameter that determines the outcome of the self-assembly process and the high-resolution power of STM can be used to track temperature-induced structural changes. A technically rigorous UHV-STM investigation of MOCN stimuli-responsiveness is provided by the study of the surface-mediated coordination chemistry of 2,3,6,7,10,11-hexaaminotriphenylene (**HATP**, or **HITP** in its fully deprotonated form) on Cu(111), with

and without co-deposited Ni adatoms (Fig. 4).[148] A key strength of the work lies in its direct visualization of coordination structures using high-resolution STM, which elucidates the role of surface chemistry and thermal activation in the hierarchical self-assembly of **HATP** molecules, as illustrated in Fig. 4. The STM data provide compelling evidence for stimuli-responsive behavior: the system exhibits distinct structural transitions upon thermal annealing, reflecting a deprotonation-triggered switch from van der Waals-stabilized assemblies, shown in Fig. 4(b) and (c), to well-defined Cu_3-coordinated trimers in the absence of Ni atoms, as presented in Fig. 4(d)–(f). However, these trimers fail to grow into fully reticulated networks, which is attributed to the smaller strength of intertrimer bonds compared to intratrimer ones, as computed through density functional theory (DFT) calculations.

Upon Ni co-deposition, STM images show a dramatic shift in coordination behavior even at room temperature, with partial deprotonation and the emergence of bis(diimino)-Ni motifs (Fig. 4(g)–(j)). Despite the higher reactivity of Ni and the formation of local honeycomb-like features, extended networks were again not observed. This was attributed to the reduced reversibility of the **HITP**–Ni coordination bonds, which hinders network evolution by kinetically trapping the sub-units.

By correlating morphological evolution with stimuli such as temperature and metal identity, the authors not only provide an atomistic picture of coordination motifs but also reveal mechanistic insight into the reversibility and scalability of MOCNs under UHV. Moreover, they offer a critical perspective on how UHV conditions diverge from liquid-phase coordination environments, particularly by providing a less dynamic environment where reversibility is reduced and rearrangement processes are hindered.

It is important to note that such conclusions are relative to the specific experimental conditions used in this work. As a matter of fact, an extended crystalline MOCN formed by **HITP**–Ni complexes was obtained on Au(111),[149] and a bimetallic **HITP**–Ni/Co network has recently been reported.[150] Notably, in this latter work, the location of the different metals in the MOCN lattice was determined by differences in STM contrast at the metal nodes.

The ability to visualize dynamic processes in 2D networks may help elucidate how local coordination environments, metal–ligand binding preferences, and structural flexibility translate to bulk MOF properties. This may be particularly valuable for understanding how defects propagate, how different polymorphs form, and how structural transformations occur.

Nanoscale insights into the MOCNs stability. Thermal annealing could accelerate the conversion of kinetic, fast-forming polymorphs into thermodynamic polymorphs by providing thermal energy.[151,152] Additionally, the equilibrium composition changes as a function of temperature.

Coordination to different metals can also lead to different thermodynamic and kinetic stability, as demonstrated by the coordination of 1,3,5-tris(4-pyridyl)benzene (**TPB**, Fig. 3(a)) with Cu and Fe on Au(111).[153] In the **TPB**-Cu MOCN, the ligands form linear complexes with the metal centers, whereas trigonal complexes are observed in the **TPB**-Fe MOCN. When the metals are deposited together and the ligand is added afterward, both networks are formed, with the **TPB**-Fe one to a larger extent. Annealing of this sample results in the **TPB**-Fe network dominating over the **TPB**-Cu one already at 400 K. Conversely, successive deposition of Fe onto a pre-formed **TPB**-Cu MOCN

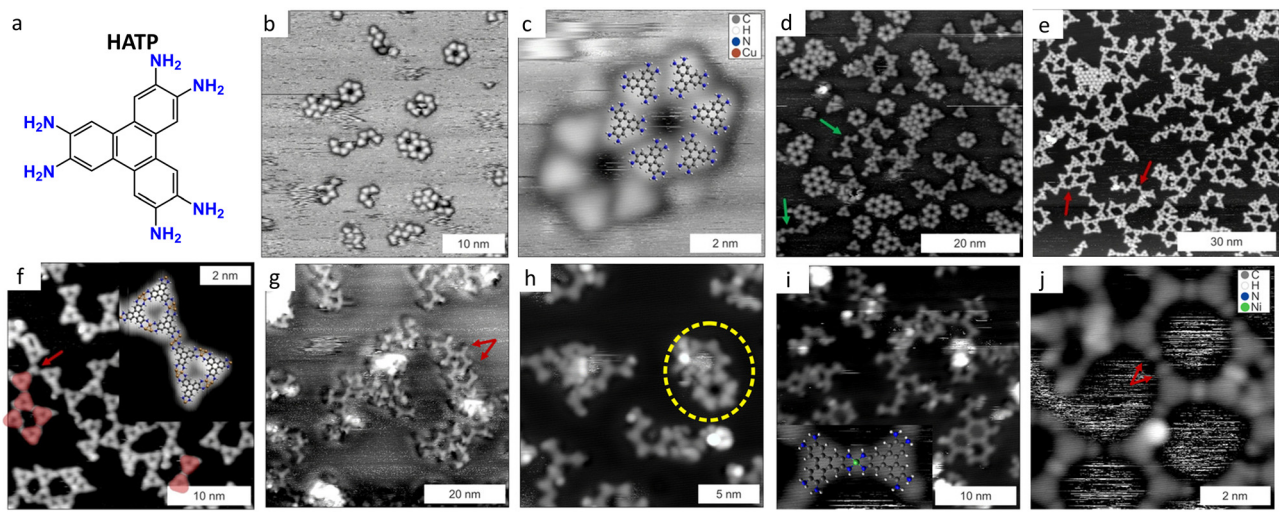

Fig. 4 **HATP** and **HITP** supramolecular (metallo-)assemblies on Cu(111). (a) Molecular structure of **HATP**. (b), (c) STM images acquired after room-temperature deposition depicting incomplete and fused **HATP** hexamers stabilized by van der Waals interactions. (d) STM image captured after annealing at 375 K, showing Cu-coordinated cyclic triangular assemblies, van der Waals-stabilized hexamers, and interlinked dimers (indicated by the green arrows). (e), (f) STM images obtained after annealing at 475 K, showing the prevalence of aggregates consisting of Cu-coordinated trimers (highlighted in red), interlinked or terminated by single **HATP** molecules (red arrows). The inset in (f) is a molecular model of two linked trimers. (g)–(j) STM images of the **HATP-Ni** complexes on Cu(111). (g) STM image of the coordination oligomers formed by **HATP** and Ni on Cu(111) at room temperature. (h) STM image of the **HATP + Ni** system after annealing at 375 K showing partial Ni-coordination and pure **HATP** hexamers (yellow dashed oval). (i), (j) STM images of the **HATP + Ni** system after complete deprotonation at 475 K leading to Ni-coordinated hexamers (the red arrows indicate Ni atoms at the periphery of incomplete hexamers). Adapted with permission from ref. 148. Copyright©2019 Wiley-VCH Verlag GmbH & Co. KGaA, Weinheim.

leaves the network almost unchanged, and the **TPB**-Fe network forms only after annealing, resulting in the complete disappearance of the **TPB**-Cu assembly at 500 K. Based on these observations, it was suggested that the **TPB**-Fe network is the thermodynamically most stable one and has a higher formation rate constant, whereas the **TPB**-Cu displays a low dissociation rate and is therefore kinetically stable up to higher temperatures if it forms first. These results highlight the significant influence of synthetic routes and kinetic *vs.* thermodynamic control on the MOCNs architecture.

Elucidation of the substrate effect. In addition to being the source of metal centers, substrates can promote the formation of structures that cannot be accessed through solution-phase methods thanks to stabilizing substrate–monomer interactions as well as geometric constraints provided by the interface. Early works showed how surfaces could promote coordination geometries that are rarely observed in bulk MOFs and determine the orientation of the MOCNs.[114,154]

The different affinities of ligand functional groups toward different metals may lead to different outcomes when ligands are deposited on different substrates. For instance, 1,3,5-tris(4-mercaptophenyl)benzene (**TMB**) was shown to coordinate to Cu adatoms on Cu(111) and form crystalline MOCNs upon annealing, whereas analogous experimental conditions on Ag(111) resulted in the formation of amorphous assemblies containing dimers connected through disulfide bridges.[151]

Interestingly, exceptions to the substrate effect may arise when coordination bonds are sufficiently strong to overcome possible orienting effects from the surface,[155] whereas network flexibility may enable the formation of extended structures across surface defects.[156]

A comparative example is provided by the different coordination structures formed by 1,4,5,8,9,12-hexaazatriphenylene (**HAT**, Fig. 5(a)) in solution and on different substrates. In solution, **HAT** has been shown to form staircase-like coordination chains due to the steric hindrance that would result from

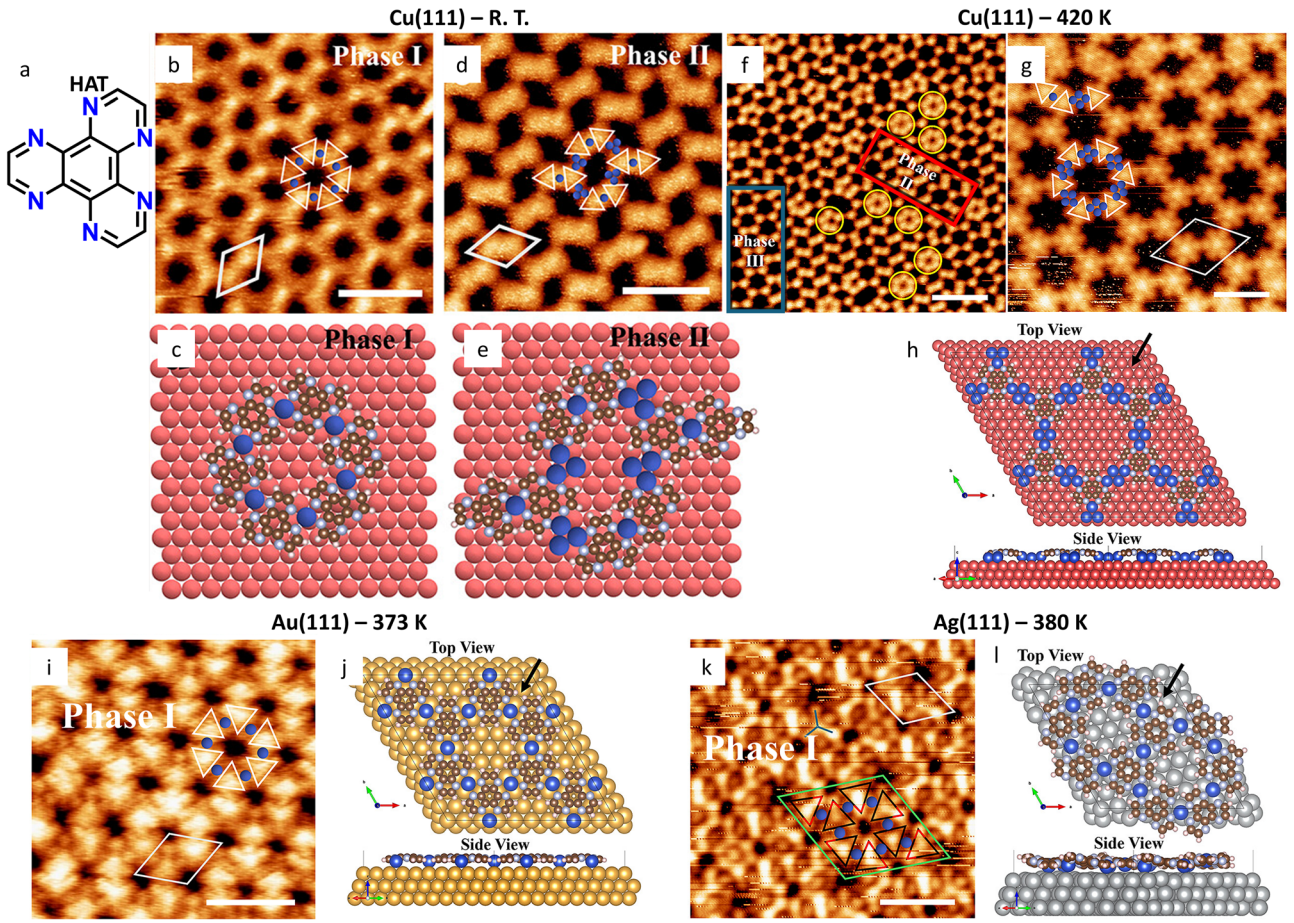

Fig. 5 Substrate effect on the **HAT-Cu** MOCN revealed by UHV-STM. (a) Molecular structure of **HAT**. (b), (d) Small-scale STM images of the two polymorphs observed on Cu(111) without annealing treatment and (c), (e) corresponding molecular models. (f) Large-scale and (g) small-scale STM images of the Cu(111) sample after annealing at 420 K. The red and blue rectangles highlight phase II and phase III polymorphs, respectively. (h) DFT-optimized top and side views of phase III, depicting the $(Cu_4)_3HAT_2$ stoichiometry. (i) Small-scale STM image of the Cu_3HAT_2 MOCN formed on Au(111) after annealing and (j) DFT-optimized top and side view of the corresponding molecular structure. (k) Small-scale STM images of the Cu_3HAT_2 MOCN formed on Ag(111) after annealing and (l) DFT-optimized top and side views of the corresponding molecular structure, depicting the buckled conformation. Scale bars (b) 2.4 nm; (d) 3 nm; (f) 5 nm; (g) 2 nm; (i) 2 nm (k) 2 nm. Adapted with permission from ref. 152. Copyright©2024 American Chemical Society.

the coordination of two bidentate sites around a metal center with square planar coordination geometry.[157] In contrast, the deposition of **HAT** along with Ni, Fe, or Co atoms on Au(111) and Ag(111), followed by annealing at 450 K, leads to the formation of a porous hexagonal network *via* in-plane coordination geometries.[41] Notably, the ligands are tilted out of the framework plane by up to 15° on Au(111), and consequently, the network has a buckled conformation, as indicated by the variation in contrast observed in the STM images and supported by DFT calculations. DFT calculations further indicated that the tilt angle reaches 23° in the gas phase to minimize the steric hindrance, and a flattening effect occurs upon surface absorption, highlighting the relevance of substrate–molecule interactions in controlling the morphology of adsorbed networks.

This substrate effect was explored in subsequent studies, where **HAT** was deposited on Cu(111) and, in combination with Cu, on Au(111), Ag(111), and MoS_2 (Fig. 5).[152] The same $\mathbf{Cu_3HAT_2}$ stoichiometry was observed after depositing the precursors on Au(111), Ag(111), and MoS_2 and annealing the samples (Fig. 5(i)–(l)). In contrast, two distinct polymorphs were observed on Cu(111) at room temperature, with the one denoted as phase I in Fig. 5(b) and (c) corresponding to the $\mathbf{Cu_3HAT_2}$ stoichiometry (Fig. 5(b)–(e)). Annealing experiments at 420 K led to the disappearance of phase I and the formation of a new polymorph, denoted as phase III, featuring complexes with $\mathbf{(Cu_4)_3HAT_2}$ stoichiometry (Fig. 5(f)–(h)). This phase transition has been attributed to the different thermodynamic stability of the two phases. Moreover, the buckled network conformation was observed only on Ag(111) and MoS_2, whereas higher adsorption energies on Cu(111) and Au(111) favor flatter conformations (Fig. 5(h), (j) and (l)).

In summary, **HAT** was demonstrated through UHV-STM to form extended MOCNs by coordinating metals on surfaces, in contrast with the 3D staircase structures observed in solution. Moreover, even when coordinating the same metals, adsorption on different substrates promotes different conformations and stoichiometries, underscoring the critical role of substrate-building blocks interactions in determining MOCN architecture.

Quantification of crystallinity. From these examples emerges the ability of STM local, molecular-resolution imaging to distinguish and characterize diverse MOCN nanostructures. However, alongside the advantage of probing local features, the small scale at which STM operates raises the question of how representative the information collected through STM imaging is of the entire surface, and how quantitative statistical information can be extracted. In fact, image analysis aimed at identifying local structural features is often performed manually, making the assessment of network quality somewhat subjective. To overcome this limitation, the principles of persistent homology (PH) were applied to the analysis of SPM images, providing an objective method for evaluating the quality of covalent porous networks.[158] By computing the points scattering in the PH diagrams obtained from binarized SPM images, a numerical parameter is derived, termed the PH score, which ranges from 0 to 1. A PH score approaching 1 indicates a more uniform pore size distribution, reflecting a higher degree of crystallinity in the network.

This method was subsequently applied to quantitatively assess the crystallinity in an MOCN containing a mixture of two homologous ligands as a function of their stoichiometric ratio.[159] The selected ligands are 2,4,6-tri(4-pyridinyl)-1,3,5-triazine (**TPT**, Fig. 6(a), top) and 4,4′-(5′-(4-(4-pyridyl)phenyl)-[1,1′:3′,1″-terphenyl]-4,4″-diyl)dipyridine (**TPBT**, Fig. 6(a), bottom), both of which form crystalline isoreticular hexagonal networks by coordinating Cu adatoms on Cu(111) over a temperature range between 300 K and 500 K (Fig. 6). Notably, 1 : 1 mixtures of the two ligands led to the formation of distinct structures depending on the annealing temperature: at lower temperatures, the ligands exhibited a tendency to segregate into separate crystalline phases, whereas annealing promoted the formation of a mixed, disordered phase, as illustrated in Fig. 6(b) and (c). Similarly, annealing samples prepared with **TPT : TPBT** stoichiometric ratios different from 1 : 1 results in amorphous phases with diverse morphologies, as shown in the series of images presented in Fig. 6(d). While no direct correlation between the PH score and other statistical parameters (Fig. 6(e)–(h)) could be established, PH remains a promising method for distinguishing between crystalline and amorphous phases. Furthermore, this study highlights the potential of STM imaging not only for visualizing different structural phases but also for identifying and quantifying amorphous domains with a high degree of precision.

Structure–function relationship. Structural control in MOCNs can be associated with fine-tuning the properties of the supramolecular networks, and such properties may differ from the ones observed in analogous frameworks of higher dimensionality. Magnetic anisotropy has long been observed in single-layered coordination networks. A notable example is provided by the extensively-studied MOCN formed by 1,4-benzenedicarboxylate (**BDC**) ligands and Fe centers on Cu(111).[73,160,161] Several polymorphs could be formed by modulating deposition parameters such as temperature and concentration, comprising Fe centers or Fe pairs coordinated to **BDC** ligands in planar geometries. The bulk analogue of these Fe-**BDC** MOCNs is **MIL101-Fe**, in which octahedral Fe(III) centers form trimers connected through the **BDC** linkers, forming a cubic structure.[162] Compared to bulk **MIL101-Fe** crystals, the on-surface array exhibits high sensitivity to chemisorption. UHV-STM images reveal O_2 adsorption near the open Fe(III) sites, which can be used to control the preferred Fe spin orientation.

The above example concerns the formation of an MOCN formed from components that ordinarily form a 3D MOF. In the case of layered 2D MOFs, it would be intuitive that the single-layer surface-supported MOCN would be analogous to a single-layer of the stacked material. However, MOCNs with structures deviating from those matching single sheets of the layered 2D MOFs formed from the same building blocks have been reported. One such example is an MOCN obtained through the sequential deposition of 2,3,6,7,10,11-hexahydrocytriphenylene ($\mathbf{H_6HOTP}$) and Co on Au(111).[163] A layered 2D MOF was previously fabricated using these precursors, consisting of an

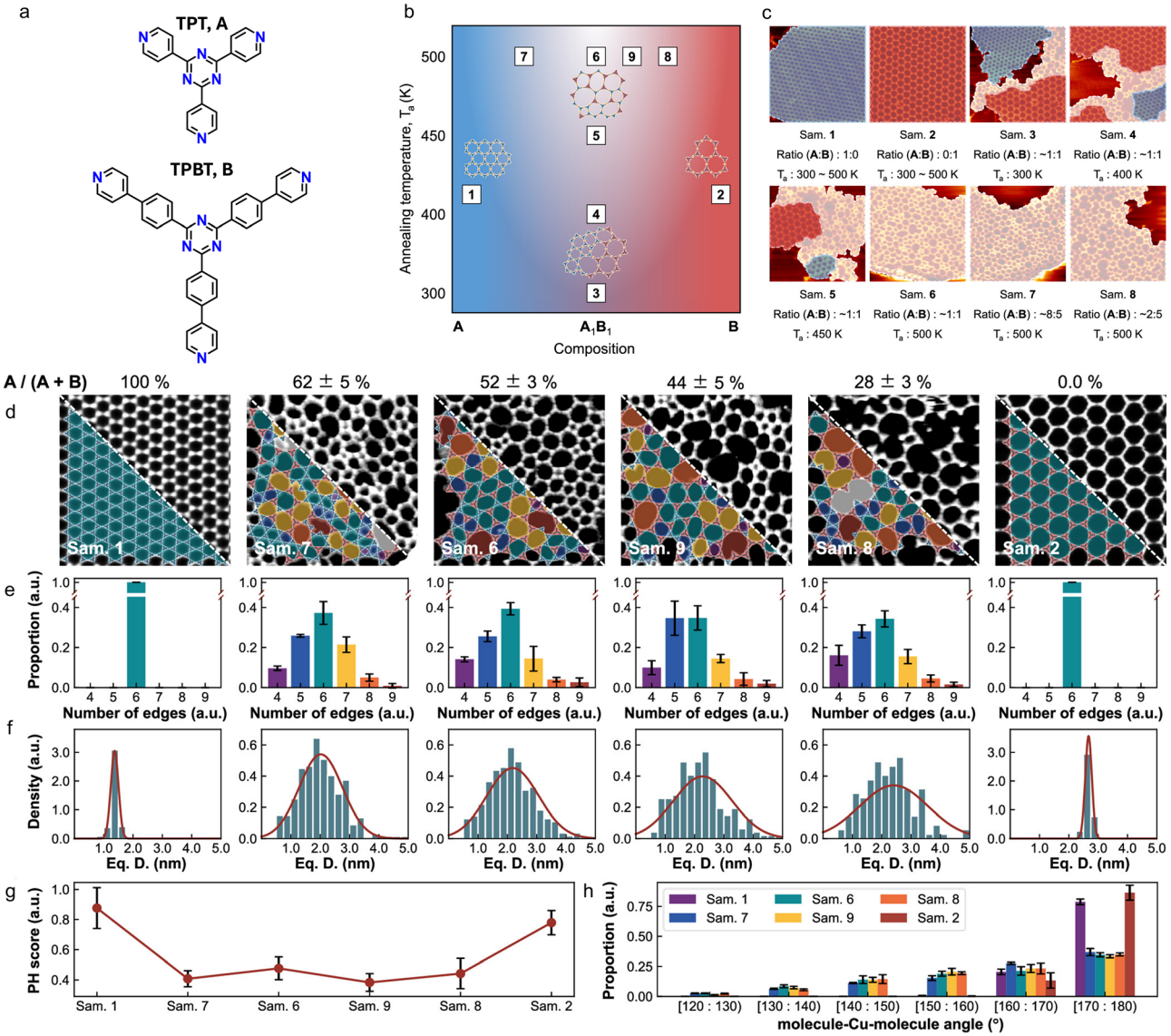

Fig. 6 Amorphous and crystalline phases in a bi-ligand MOCN on Cu(111). (a) Molecular structures of **TPT** (**A**) and **TPBT** (**B**). (b) Composition diagram of the different phases observed as a function of the **A** : **B** stoichiometric ratio and of the annealing temperature. (c) Representative STM images of some of the samples marked in (b). The **TPT** crystalline phase is marked by the blue overlays; the **TPBT** crystalline phase is marked by the red overlays. (d)–(h) Statistical data for quality assessment. (d) Representative STM images of the samples marked in (b). The overlays indicate pores of various shapes: blue: tetragons, green: hexagons, yellow: heptagons, orange: octagons, red: higher order polygons. (e) Polygons distribution for each sample. On the *x*-axis, the number of edges of the polygon is reported. (f) Pore diameter distribution for each sample. The red line depicts a Gaussian distribution fit. (g) PH score values for each sample. (h) Molecule–Cu–molecule angle distribution for each sample. Adapted with permission from ref. 159. Copyright©2023 American Chemical Society.

alternate stacking of two different layers. One layer is an extended honeycomb with Co_3(**HOTP**)$_2(H_2O)_6$ stoichiometry that features hexagonal pores, whereas the other layer contains discrete Co_3(**HOTP**)$(H_2O)_{12}$ complexes.[164] In contrast, surface confinement promotes a unique architecture in which each metal center is coordinated to three different **HOTP** ligands, as opposed to one or two in the layered material. STS measurements supported by DFT calculations showed that the **HOTP**-Co MOCN exhibits a smaller bandgap than the one that was previously reported for the layered 2D MOF thin film analog.[165] The magnetic anisotropy displayed by the **HOTP**-Co MOCN, coupled with the evidence of antiferromagnetic interactions, opens up new opportunities for integrating such assemblies into spintronic applications.[166]

The use of organic radicals as ligands presents an effective strategy to promote strong magnetic coupling between metal nodes. In contrast to traditional diamagnetic linkers, radical ligands can serve as active spin carriers, enabling π–d interactions that enhance magnetic exchange and circumvent the requirement of using short linkers. A recent study demonstrates this approach through the on-surface synthesis of a large-scale, atomically precise MOCN using asymmetric radical

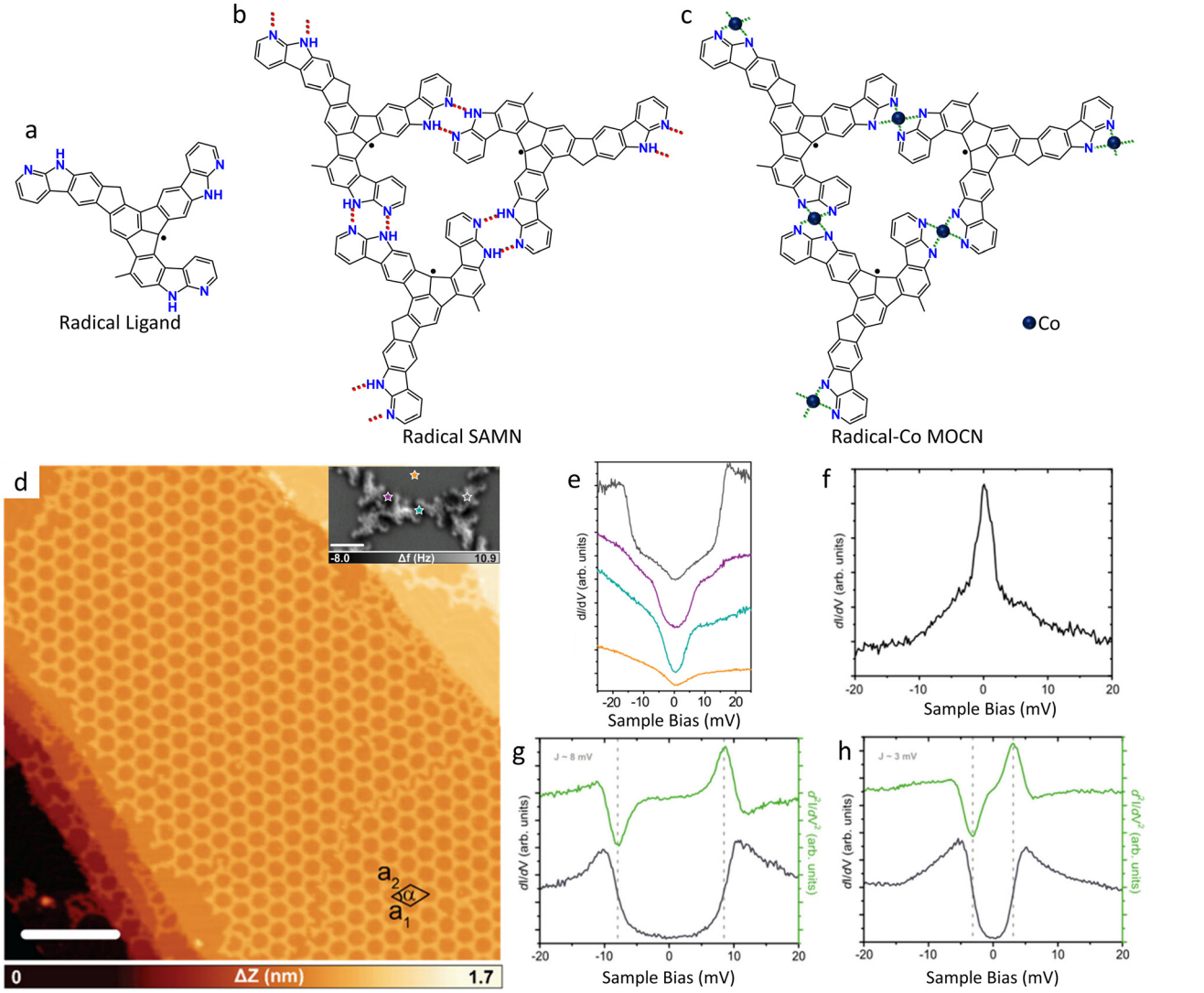

Fig. 7 Magnetic coupling in a radical-based MOCN. (a) Molecular structure of the radical ligand. The arms on the ligand are numbered 1-3. (b) Structure of the hydrogen-bonded SAMN formed by the self-assembly of the radical ligand. (c) Structure of a Co-coordinated trimer of radical ligands in the MOCN formed by addition of Co on the radical ligand SAMN. (d) Constant-current STM image of the radical ligand-Co MOCN (scale bar = 28 nm; lattice parameters: $a_1 = a_2 = 6.4$ nm, $\alpha = 60°$). Inset: nc-AFM of two adjacent Co-coordinated molecular ligand trimers. (e) Long-range differential conductance spectra recorded at different locations, marked in the inset of (d). (f)–(h) Differential conductance spectra in the absence of Co and in the case of Co-coordinated radical ligand dimers connected at the arms 3-3 and 1-2, respectively. Adapted from ref. 167. Copyright©2025 The Authors. Published by American Chemical Society.

ligands coordinated with Co centers (Fig. 7).[167] This two-step strategy, involving initial on-surface formation and supramolecular organization of the radicals (Fig. 7(b)) followed by metalation, yields a high-quality magnetic network with long-range order (Fig. 7(c) and (d)). UHV-STM, STS, and nc-AFM techniques coupled with DFT calculations revealed two distinct magnetic couplings corresponding to different complexes. While no magnetic coupling is observed in the radical ligand SAMN (Fig. 7(f)), magnetic exchange is observed in the Co-coordinated structures, depending on how the ligands are connected within a coordination complex (Fig. 7(e), (g) and (h)). These results evidence strong π–d interactions and the coexistence of antiferromagnetic and ferromagnetic coupling modes. Notably, this methodology maintains porosity while achieving a complex spin texture, expanding the design space for 2D magnets. The radical-as-ligand approach thus offers a powerful pathway to engineer multifunctional MOCNs with tunable electronic and magnetic properties, holding promise for integration in quantum materials and spintronic architectures.

Isoreticular chemistry represents a well-established approach in MOF design that enables the fabrication of frameworks with similar topologies but varying pore dimensions through the systematic use of ligands with analogous shapes and functional groups and different molecular lengths. While this strategy has been extensively employed in 3D MOF synthesis, its application to surface-confined MOCN fabrication remains relatively underexplored.[114,133,159]

A compelling demonstration of this approach is the synthesis of a Dy-based MOCNs on Cu(111) using two isoreticular carboxylate linkers: *p*-terphenyl-4,4′-dicarboxylic acid (**TDA**) and **BDC**.[133] These ligands bring analogous carboxylate groups while having different molecular lengths. Each of the two oxygen atoms of the carboxylates occupies a coordination site around the Dy centers, and the large radius of the lanthanide allows for the accommodation of four ligands around the cation, resulting in an eightfold coordination geometry, regardless of the ligand length. As a result, isoreticular porous MOCNs are obtained with an internodal distance of 11.8(5) Å in the Dy-**BDC** network and 20.5(5) Å in the Dy-**TDA** network, as revealed by UHV-STM measurements. Despite the significant difference in pore dimensions between the two networks, the magnetic properties show only subtle variations. Both systems exhibit similar enhancement of magnetic anisotropy compared to isolated Dy atoms, with the only difference seemingly being a slightly smaller tilting angle of the anisotropy axis for the Dy-**BDC** MOCN. While the authors conclude that magnetic properties result from a delicate balance between oxygen–Dy^{3+} interactions and crystal field geometry, the experimental evidence suggests this balance is largely insensitive to the internodal distance variations achieved through isoreticular design.

A similar investigation of the structure–function relationship in isoreticular MOCNs was presented on the networks based on dicyanobiphenyl (**DCBP**) and dicyanoanthracene (**DCA**) ligands and Co, sequentially deposited on epitaxial graphene grown on Ir(111).[168] Low-temperature UHV-STM and nc-AFM studies revealed that both ligands formed extended honeycomb MOCNs, containing $Ligand_3Co$ complexes. $\mathbf{DCBP_4Co}$ complexes were also observed, whereas **DCA** formed exclusively $\mathbf{DCA_3Co}$ complexes due to steric hindrance. STS measurements supported by DFT calculations demonstrated stronger coupling between the molecular building blocks of $\mathbf{DCA_3Co_2}$ MOCN than in the $\mathbf{DCBP_3Co_2}$ isoreticular analog, resulting in a significant bandwidth in the former network, which could be exploited for engineering new electronic materials.

3.2 MOCNs fabricated and characterized at the liquid–solid interface

In liquid-phase synthesis, a solution of precursors is drop-cast onto a flat surface under ambient atmospheric pressure. This method is fast and cost-effective; however, exposure to ambient conditions increases the risk of contamination.[106,107]

The disparity between the number of reports on MOCNs fabricated in UHV and the ones fabricated at the liquid–solid interface arises from several interconnected experimental challenges. First, the sensitivity of certain metal surfaces to atmospheric conditions can lead to oxidation and surface contamination, compromising both the substrate quality and the fidelity of metal–organic coordination. Second, solubility limitations present a significant obstacle: many metal salts exhibit poor solubility in organic solvents suitable for STM imaging, while conversely, solvents that effectively dissolve metal precursors may be incompatible with ambient STM operation due to high volatility, conductivity, or chemical reactivity with the tip. Third, organic ligands and metal adatoms are constrained to the surface in UHV conditions, guiding the formation of planar complexes more readily than at liquid–solid interfaces. In the latter scenario, three-dimensional complexes may preferentially form in solution, subsequently competing with or impeding the formation of extended 2D monolayers.

Furthermore, ambient-STM studies of MOCNs demand precise control over multiple experimental parameters simultaneously, including deposition protocols, concentration ratios, solution chemistry, and environmental conditions. The complexity of optimizing these interdependent variables often makes liquid–solid interface studies more technically demanding than their UHV counterparts, where individual parameters can be controlled more independently.

Despite these challenges, the liquid-phase environment offers unique advantages that justify the additional experimental complexity. The presence of solvent introduces an additional parameter that can be tuned to direct self-assembly outcomes, through specific solvation effects and solvent–substrate interactions. Moreover, the liquid medium facilitates dynamic processes through continuous adsorption–desorption equilibria, as illustrated in Fig. 8, enabling error correction mechanisms and access to thermodynamically favored structures that may be kinetically inaccessible under vacuum conditions. This dynamic environment also permits real-time observation of assembly evolution and reorganization processes.

Finally, as already noted, MOF thin films and crystal powders are often synthesized using wet chemistry approaches. Consequently, while technically more challenging, liquid–solid interface studies offer complementary information essential for understanding the full scope of MOCN formation mechanisms, their potential for practical applications under ambient conditions, and their correlation with analogues of higher dimensionality.

The introduction of metal ions into SAMNs of coordinating molecules has been shown to induce dramatic structural transformations and promote the formation of new phases templated by metal coordination geometry.[169,170] In addition to these examples, the majority of reported STM studies investigating metal coordination in supramolecular assemblies at the liquid–solid interface have focused on SAMNs exhibiting coordination bonds along a single direction (one-dimensional, 1D).[171–177] These studies have nonetheless provided valuable insights into the fundamental principles governing the formation of metal-coordinated supramolecular structures at liquid–solid interfaces. Key findings have elucidated the role of metal coordination in forming new architectures at the liquid–solid interface, the critical influence of mixing procedures (*ex situ versus in situ* metalation) on polymorph selection, and the effects of metal-to-ligand concentration ratios on assembly outcomes.

This section will first examine these crucial aspects that govern metal–organic assembly at liquid–solid interfaces. Subsequently, we will review reports on more complex 2D MOCNs fabricated under ambient conditions, with particular emphasis on how the liquid environment enables unique structural

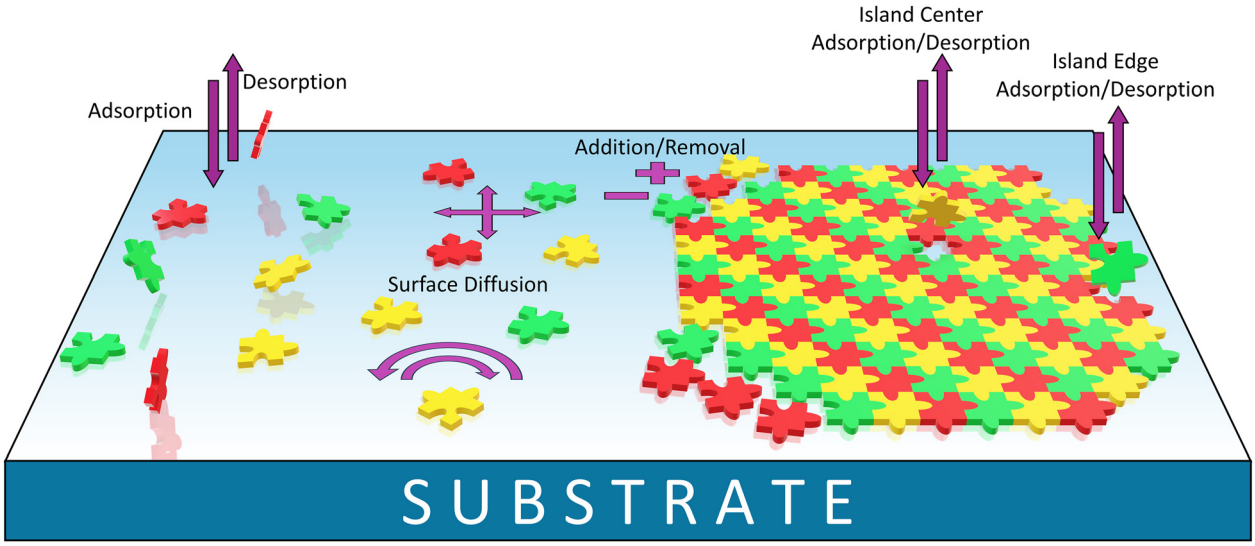

Fig. 8 Cartoon depicting typical interface equilibria during the formation of supramolecular networks, such as MOCNs, at the liquid–solid interface. Puzzle pieces of different colors indicate different building blocks. For example, a three-component equilibrium may involve metal ions, organic ligands, and guest molecules.

control compared to UHV conditions. Throughout this discussion, we will highlight the intrinsic mechanistic differences between liquid-phase and vacuum-based MOCN formation, including the role of solvation effects, dynamic equilibria, and the influence of substrate–solvent interactions on final network architectures.

Real-time monitoring of the formation of 1D metal–organic polymers. The synergistic combination of reversible van der Waals interactions with the strong coordination bonds was used to fabricate nanoribbons of porphyrin derivatives on HOPG.[175] Both pre-mixing and sequential drop-casting of the ligand and Ni(II) precursors onto the substrate resulted in the formation of metal-coordinated ribbons, which laterally interacted *via* interdigitation of alkyl chains. Remarkably, the porphyrin derivative-Ni arrangements fabricated *via in situ* metal addition exhibited dynamic structural evolution over time, ultimately reaching thermodynamic equilibrium within approximately one hour. This temporal evolution underscores a key advantage of liquid–solid interface assembly: the maintenance of sufficient molecular mobility at room temperature to enable error correction and optimization of intermolecular interactions, contrasting sharply with the typically kinetically trapped structures obtained under UHV conditions.

The ability to achieve equilibrium structures through dynamic processes suggests that liquid-phase assembly may provide access to thermodynamically favored coordination geometries and packing arrangements that are otherwise inaccessible through vacuum-based preparation methods. Furthermore, the successful interplay between metal coordination (providing directional bonding) and van der Waals interactions (enabling lateral organization) demonstrates a hierarchical assembly strategy that could be extended to more complex multi-component systems requiring precise structural control across multiple length scales.

Revealing the nanoscale impact of the sample preparation. Different polymorphs may be formed when ligand and metal precursors are pre-mixed *ex situ* or sequentially deposited and mixed *in situ* on the surface. This phenomenon was demonstrated through the investigation of supramolecular coordination assemblies formed by bio-based rufigallol derivatives functionalized with tetradecyloxy chains in combination with Cu(II).[176] Matrix-assisted laser desorption/ionization mass spectrometry (MALDI-MS) carried out on metal–ligand mixtures confirmed ligand metalation and the formation of oligomers. When the reactants were mixed *ex situ*, two different domains were observed at the HOPG/1,2,4-trichlorobenzene interface: one consisting of self-assembly of dimeric coordination complexes and another composed of metal–organic oligomers organized in a columnar structure. Similarly, *in situ* mixing of the precursors initially generated both kinds of domains; however, these dynamically evolved to form exclusively the columnar assembly over time.

These observations reveal substantial differences between in-solution and on-surface coordination-mediated self-assembly processes. As a possible reason for the different outcomes of the two procedures, the authors suggested that when metalation occurs *ex situ*, domains of dimers cannot evolve into columnar structures due to depletion of free Cu(II) ions in solution. Conversely, when metalation proceeds on the surface, sufficient unreacted precursors remain available to facilitate continued oligomer formation. These longer oligomers exhibit enhanced surface affinity due to their increased number of alkyl chains, providing stronger van der Waals interactions with the substrate. Additionally, surface-assisted growth may promote the incorporation of residual monomers into pre-adsorbed oligomers through a templating effect.

Notably, *in situ* addition of excess Cu(II) to samples prepared by pre-mixing did not induce structural changes in the on-

surface assemblies, suggesting that the pathway-dependent polymorphs may represent kinetically trapped states rather than equilibrium structures. This observation raises important mechanistic questions about the role of surface confinement in determining coordination stoichiometry and assembly pathways. A compelling follow-up experiment would involve thermal annealing of the pre-mixed polymorphs to determine whether they constitute metastable states that can be converted to the thermodynamically favored columnar structure. Such studies would elucidate whether *in situ* mixing facilitates the formation of the true thermodynamic product or merely provides kinetic access to alternative assembly pathways. Furthermore, systematic variation of metal-to-ligand ratios and coordination kinetics by exploring different metal ions could provide deeper insights into the competition between solution-phase complexation and surface-mediated assembly processes.

Metal-to-ligand ratio effect. As stated above, metal ions can template the formation of more than one type of distinct supramolecular assembly from a single type of organic molecule, with the final network morphology depending on the absolute and relative concentrations of metal ions and ligands concentration and ligand-to-metal stoichiometry. This structural control on the basis of altering the relative concentration of metal ions and ligands is exemplified by the diverse architectures observed on HOPG when 4,4′,4″-(1,3,5-triazine-2,4,6-triyl)tribenzoic acid (**TATB**) is combined with Cu(II) and Fe(III).[170]

In the absence of metal ions, **TATB** spontaneously forms a porous honeycomb network stabilized by intermolecular hydrogen bonds between carboxylic acid groups. The introduction of Cu(II) ions considerably alters this assembly behavior, and the final architectures depend critically on the Cu(II)/**TATB** molar ratio. At a Cu(II)/**TATB** molar ratio of 1 : 2, **TATB**–Cu(II)–**TATB** dimers form, with these coordination units serving as building blocks for extended structures where adjacent dimers interact through residual hydrogen bonding.

Increasing the relative concentration of Cu(II) ions with respect to the ligand to a Cu(II)/**TATB** 1 : 1 molar ratio produces a markedly different architecture featuring alternating **TATB** and Cu(II) rows, where hydrogen-bonded **TATB** chains are interconnected through Cu(II) coordination bridges.

The structural templating effect becomes even more pronounced with Fe(III) ions. At a 1 : 1 Fe(III)/**TATB** stoichiometry, the system self-assembles into discrete trigonal trimers, where Fe(III) centers template the formation of hydrogen-bonded **TATB** trimers. Further increasing the Fe(III) relative concentration to a 3 : 2 Fe(III)/**TATB** molar ratio triggers a structural transition, yielding chain architectures where Fe(III) ions intercalate between hydrogen-bonded **TATB** rows. These observations underscore how both metal identity and metal-to-ligand ratio serve as powerful tools for directing supramolecular assembly, enabling access to structurally diverse networks from a single organic building block through judicious selection of self-assembly conditions.

Nanoscale characterization of 2D MOCNs at the liquid–solid interface. Breaking away from the predominantly 1D coordination networks described above, the fabrication of truly 2D MOCNs at the liquid–solid interface has been achieved. The molecular tectonics design strategy was employed to construct a 2D MOCN using an asymmetric porphyrin-derived ligand (**P**) in combination with Co(II) on HOPG (Fig. 9).[79] The approach involved premixing of **P** with $CoCl_2$ as the metal precursor in 1-phenyloctane, followed by drop-casting onto HOPG, which successfully yielded an ordered **P**-Co(II) MOCN on the surface, depicted in Fig. 9(c) and (d). The proposed arrangement based on STM images is consistent with the square planar positioning of four **P** ligands in the equatorial plane of octahedral Co(II) complexes, with the coordination of two chloride anions expected to satisfy the octahedral coordination geometry of Co(II). Among the five theoretically possible metal-coordinated networks, the one with the smallest unit cell and highest symmetry is displayed in Fig. 9(f).

Notably, the preparation method proved critical for achieving structural order. While *ex situ* premixing produced the ordered 2D network, *in situ* addition of a $CoCl_2$ solution onto the preformed SAMN of the ligand resulted in disordered structures on the substrate. The authors attributed this difference to the strong interfacial interactions between the substrate and the building block **P**, which likely prevent efficient reorganization when metal coordination occurs after initial surface adsorption. This observation highlights a crucial distinction between liquid–solid interface assembly and UHV-based approaches: the pre-existing molecular organization on the surface can kinetically trap disordered states when subsequent metal addition disrupts established intermolecular contacts. Conversely, *ex situ* coordination allows the system to explore its full configurational space in solution before surface deposition, enabling access to the thermodynamically favored ordered structure. This work thus establishes important guidelines for synthetic strategies targeting 2D MOCNs at liquid–solid interfaces. In a similar way, mellitic acid (**MA**) was pre-mixed with $PdCl_2$ or $ZnCl_2$ in methanol before drop-casting onto HOPG.[178] STM results revealed distinct network structures due to the differing coordination properties of the two metal ions.

Nanoscale characterization of chirality in networks formed from pro-chiral supramolecular building blocks. The liquid–solid interface provides unique opportunities for investigating chiral expression and amplification in coordination networks through solvent-mediated effects that are inaccessible under vacuum conditions. A comprehensive investigation combining STM imaging, X-ray photoelectron spectroscopy (XPS) measurements, and DFT calculations has examined a hybrid hydrogen-bonded, metal-coordinated 2D network based on ethynyl-4-pyridyl guanine-based ligands (**C6G4Py**) coordinated to Pd(II) at the HOPG/heptanoic acid interface (Fig. 10).[80] The precursors were drop-cast onto HOPG from pre-mixed solutions. Notably, **C6G4Py** forms hydrogen-bonded quartets in solution that are prochiral (Fig. 10(a)); however, surface confinement induces symmetry breaking, allowing the quartets to adsorb in two distinct enantiomeric orientations, as illustrated in Fig. 10(b).

In the absence of added metal ions, **C6G4Py** forms a SAMN where **C6G4Py** quartets adsorbed with opposite handedness co-

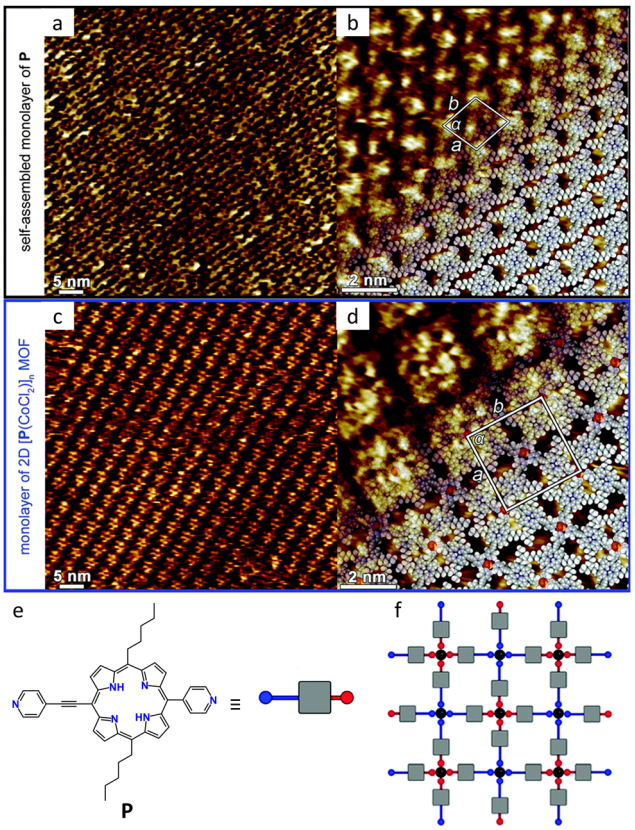

Fig. 9 Porphyrin MOCNs at the 1-phenyloctane/HOPG interface. (a), (b) STM current image of a monolayer of free "tecton" **P**. The proposed molecular model is shown in (b). (c), (d) STM current image of a monolayer of the 2D **P**-Co(II) MOCN. The proposed molecular model is shown in (d). (e) Molecular structure of **P**. (f) Schematic representation of the MOCN with the smallest unit cell that may be formed upon combining the neutral acentric tecton **P** with $CoCl_2$ (black sphere). In (e), (f), the grey square represents the porphyrin core, whereas the red and blue segments correspond to the pyridyl unit directly connected to the porphyrin backbone and the ethynyl pyridyl moiety, respectively. Chloride anions occupying the two apical positions on the octahedron around the Co(II) cation are not presented for clarity. Adapted with permission from ref. 79. Copyright©2014 The Royal Society of Chemistry.

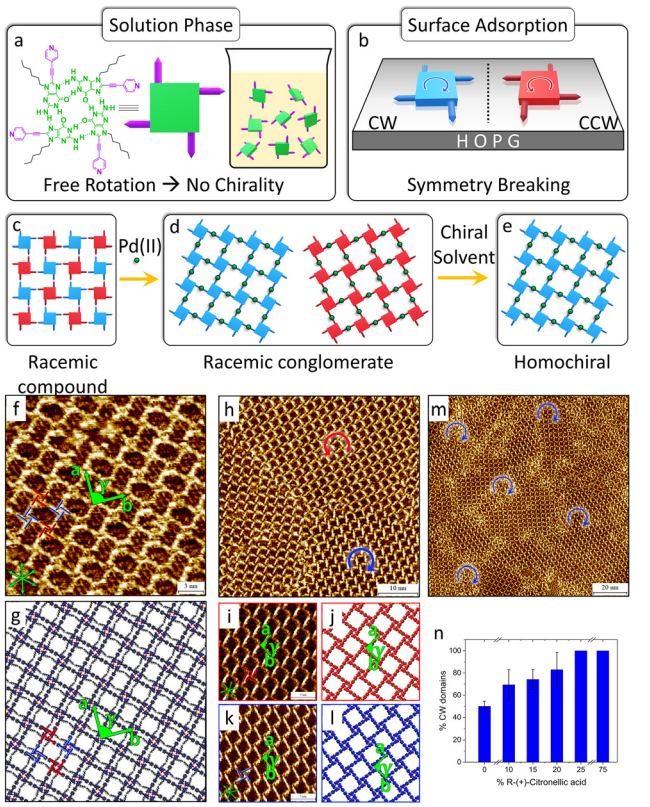

Fig. 10 Enantiomers segregation and solvent induced chiral selection in the **C6G4Py**-Pd(II) MOCN. (a) Molecular structure of the **C6G4Py** hydrogen-bonded quartets. In the solution phase, they are free to rotate and are therefore prochiral. (b) Symmetry breaking in **C6G4Py** quartets upon surface confinement. The opposite enantiomers are indicated as clockwise (CW, blue) and counterclockwise (CCW, red). (c)–(e) Successive chiral transitions observed starting from the **C6G4Py** SAMN, following Pd(II) addition, and the use of an enantiopure solvent. (f) Representative high-resolution STM image of the racemic compound of **C6G4Py** quartets and (g) corresponding molecular model. Lattice parameters: $a = 3.9 \pm 0.1$ nm, $b = 3.9 \pm 0.1$ nm, $\gamma = 90 \pm 1°$ (*p4gm* plane group). (h) Representative large-scale STM image of the racemic conglomerate formed by mixing **C6G4Py** and Pd(II). (i), (k) High-resolution STM images of CCW and CW domains of the **C6G4Py**-Pd(II) MOCN, respectively, and (j), (l) corresponding molecular models (the alkyl chains and the counterions are omitted for clarity). (m) Large-scale STM image showing the formation of homochiral domains in (*R*)-(+)-citronellic acid. (n) Variation in the surface coverage of CW G-quartets as a function of volume % of (*R*)-(+)-citronellic acid in a heptanoic acid/(*R*)-(+)-citronellic acid solution mixture. Adapted with permission from ref. 80. Copyright©2022 American Chemical Society.

crystallize and distribute periodically within the same phase, creating a racemic compound on HOPG, as depicted in Fig. 10(c), (f) and (g). When Pd(II) is introduced into the system, each Pd(II) connects two **C6G4Py** quartets, and spontaneous chiral resolution occurs upon this metal coordination. Enantiomorphous domains, forming racemic conglomerates, are characterized at the HOPG/heptanoic acid interface, as shown in Fig. 10(d), (h)–(l). The resulting chiral MOCN comprises homochiral hydrogen-bonded **C6G4Py** quartets bridged by Pd(II) centers that coordinate to the pyridyl moieties. Remarkably, chiral resolution was also observed following *in situ* addition of Pd(II) salt solution to the pre-formed **C6G4Py** SAMN.

Furthermore, complete chiral selection was achieved using enantiopure (*R*)-(+)-citronellic acid at low concentration (25% v/v, Fig. 10(e), (m) and (n)), while the opposite handedness resulted from using the *S* enantiomer. The possibility of hosting guest molecules inside the pores of the network was also confirmed.

In analogy with the works performed in UHV, STM at the liquid–solid interface offers the opportunity to identify and differentiate domain-specific chirality and even the opposite handedness of enantiomeric building blocks within one domain. Additionally, this work demonstrates the distinct advantages of liquid–solid interface studies: the ability to employ chiral solvents for controlling network handedness and achieving complete chiral amplification through solvent-mediated chirality transfer, which is fundamentally unavailable in UHV environments and provide an inexpensive, generic pathway toward homochiral coordination networks.

Quantification of crystallinity and elucidating structural control. A comprehensive study has systematically addressed multiple factors governing MOCN synthesis at liquid–solid interfaces through investigation of **TPT**-Pd(II) coordination networks (Fig. 11).[81] This work employed both sequential and one-pot synthesis protocols to examine the effects of solvent choice, precursor concentration, and temperature on network formation and crystallinity, providing quantitative analysis of structural ordering and elucidating possible growth mechanisms.

The sequential protocol involved separate drop-casting of **TPT** followed by Pd(II), with annealing at temperatures ranging from 20 to 120 °C. STM characterization at the HOPG/1-phenyloctane interface revealed that increasing the annealing temperature progressively enhanced network ordering, as illustrated by the selection of STM images shown in Fig. 11(a)–(e). Quantitative analysis demonstrated improved crystallinity through measurements of surface coverage, domain number and size distribution, and PH score, introduced in Section 3.1.

In contrast, the one-pot protocol involved premixing **TPT** and Pd(II) in a 2 : 3 ratio at 100 °C in nonanoic acid prior to deposition. Annealing was essential to obtain the **TPT**-Pd(II) MOCN. Compared to the sequential protocol, premixing yielded networks with different morphological characteristics, including vacancy defects and bilayer features (Fig. 11(f) and (g)). Apart from these differences, the porous honeycomb network featuring hexagonal cavities shown in Fig. 11(h) and (i) was obtained through both procedures.

The morphological differences arising from the two fabrication protocols suggest that the two synthetic routes likely operate through distinct growth pathways. The sequential approach appears to follow a chain-growth-like mechanism, wherein crystallization initiates at specific nucleation sites with subsequent binding of neighboring building blocks until grain boundary formation. Conversely, the one-pot synthesis in nonanoic acid likely proceeds through a step-growth-like mechanism, where oligomers are preformed in solution during annealing and subsequently assembled, and connected, on the surface during solvent evaporation.

Crucially, the study demonstrates the presence of accessible pores through STM imaging of guest molecule adsorption. Addition of hexa-*tert*-butyl-hexa-*peri*-hexabenzocoronene (**6tBu-HBC**) as a molecular guest on the pre-formed **TPT**-Pd(II) MOCN confirmed pore accessibility within the honeycomb structure (Fig. 11(j)). Notably, guest adsorption was observed exclusively in networks synthesized *via* the sequential protocol, highlighting notable differences between the two fabrication routes and their impact on pore accessibility.

This comprehensive investigation thus establishes key structure–property relationships governing MOCN synthesis at liquid–solid interfaces while demonstrating the critical role of STM characterization in understanding both underlying assembly mechanisms and functional properties that are potentially relevant to catalysis and molecular recognition applications.

The molecular-level insights provided by STM hold great potential for advancing research on metal–organic coordination systems. The emerging capability to fabricate porous MOCNs at the liquid–solid interface and characterize them under ambient conditions represents a significant methodological advancement, effectively bridging the research domains of MOCNs and MOFs. This methodological convergence enables unprecedented

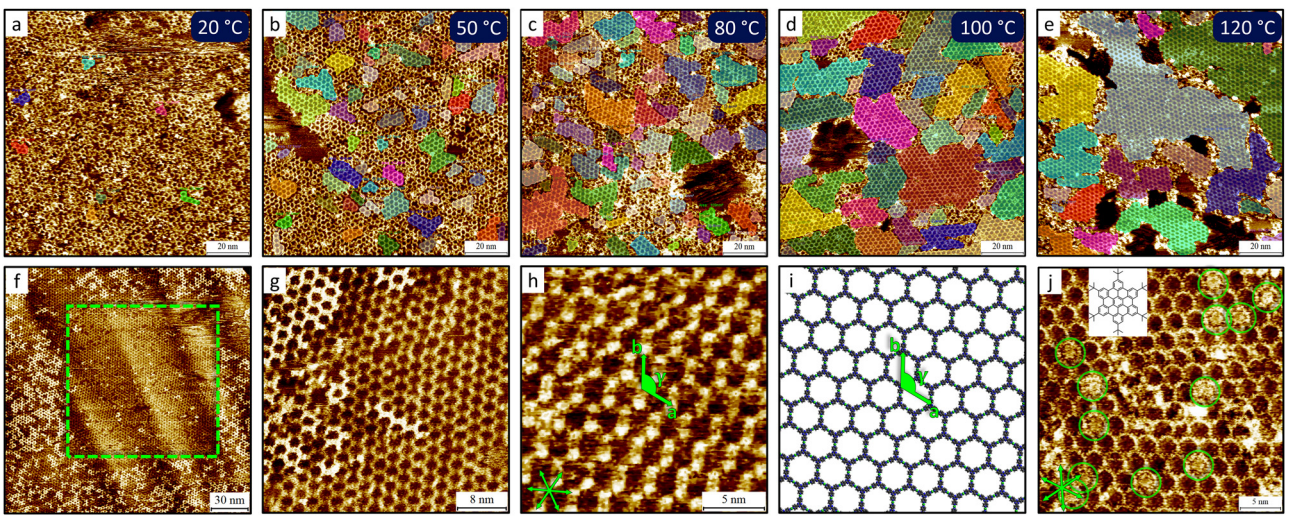

Fig. 11 Molecular insights into the morphological changes of the **TPT**-Pd(II) porous MOCN. (a)–(e) Representative large-scale STM images showing the increase in crystallinity as a function of the annealing temperatures of samples prepared using the sequential protocol. The crystalline domains are marked by the coloured overlays. The images were acquired at the HOPG/1-phenyloctane interface. (f) Large-scale image showing the removal of the top layer of the **TPT**-Pd(II) MOCN prepared with the one-pot protocol within the nanoshaved area, marked by the dashed square; the top layer in the surrounding areas is intact. (g) High-resolution image of the bilayer, revealing the A–A stacking. (h) High-resolution image of the **TPT**-Pd(II) MOCN and (i) corresponding molecular model. The images were obtained at the HOPG/nonanoic acid interface. Lattice parameters: $a = 2.6 \pm 0.1$ nm, $b = 2.6 \pm 0.1$ nm, $\gamma = 120 \pm 1°$. (j) High-resolution STM image of the **TPT**-Pd(II) MOCN hosting **6tBu-HBC** molecules in its pores, as highlighted by the green circles. **6tBu-HBC** molecular structure is shown in the inset. Imaging was carried out at the HOPG/1-phenyloctane interface. Adapted with permission from ref. 81. Copyright©2025 The Authors. Published by American Chemical Society.

comparative investigations, allowing researchers to explore critical material properties across different dimensions. Specifically, STM emerges as a pivotal technique for systematic exploration of:

– Network stability: investigating how structural dimensionality influences material stability.

– Local features: for example, the identification of chiral centers and their differentiation.

– Guest adsorption mechanisms: examining molecular interactions and adsorption dynamics.

– Stimuli responsiveness: analyzing structural and functional changes under various external stimuli (light, chemical).

4. AFM characterization of MOFs

AFM is a powerful technique for characterizing materials, including MOFs, beyond layers that are only one (or a few) atoms thick. Beyond providing structural insights and probing electrical properties, AFM enables the investigation of dynamic phenomena such as crystal growth, phase transitions, and solvent-induced delamination.[68,179–187] The local chemical composition can be analyzed by AFM-IR, offering a complementary method for characterizing MOFs.[95]

This section analyzes recent advances in AFM and AFM-IR techniques for MOF characterization, with particular emphasis on liquid–solid interface studies. A distinction will be made between studies performed on MOF thin films *vs.* single crystals, revealing both similarities and differences between these two material classes.

Many studies are performed on **HKUST-1**, which represents one of the foundational and most extensively studied MOFs, establishing critical benchmarks for the field through its unique combination of chemical tunability and thermal stability up to 240 °C.[188] **HKUST-1** can be synthesized as either a crystalline powder or a thin film, typically using copper acetate ($CuOAc_2$) and **BTC** precursors. Its structure consists of paddlewheel dicopper(II) tetracarboxylate metal nodes interconnected by **BTC** linkers. The framework can be synthesized under a range of different conditions, and it has a well-defined structure, thus positioning **HKUST-1** as an ideal MOF for exploring and advancing unconventional characterization methodologies in MOF research.[189]

The application of AFM to MOF characterization marked a pivotal advancement in understanding crystalline defects and enabled unprecedented real-time monitoring of growth pathways in **HKUST-1** crystals.[82,83] This breakthrough was significantly enhanced by the development of *in situ* growth protocols, which demonstrated substantial advantages over traditional *ex situ* preparation methods.[190] Direct on-substrate growth not only yielded superior structural quality but also facilitated systematic optimization of synthesis procedures and growth conditions, representing a methodological leap forward in MOF fabrication control. Moreover, comparative studies conducted under UHV *vs.* ambient conditions revealed surface erosion phenomena upon air exposure.[190] This finding established the critical importance of environmental control in accurate structural characterization, setting new standards for experimental protocols in the field.

4.1 Epitaxially-grown MOFs

Different synthetic procedures can yield MOFs in the form of thin films.[43,191–196] As mentioned earlier, sample immobilization is a critical requirement to perform AFM characterization. Liquid-phase epitaxy (LPE) has been demonstrated as an efficient strategy for growing MOF thin films on solid substrates. These surface-mounted MOFs (SURMOFs) are synthesized using the layer-by-layer (LbL) technique on Au(111) substrates functionalized with self-assembled monolayers (SAMs) bearing functional groups that can coordinate with the metal nodes in the MOF.[197] As illustrated in Scheme 5, this process involves sequential immersion of the substrates in two discrete solutions: one containing metal nodes and the other comprising organic ligands. A rinsing step is frequently incorporated after each immersion to eliminate unreacted precursors. Alternative approaches employ spray coating or spin coating techniques to deposit the solutions on the substrate. SURMOFs fabricated *via* LPE exhibit specific orientations, and their thickness can be precisely modulated by varying the number of immersion cycles. Furthermore, LPE helps to overcome the interpenetration issue encountered when targeting MOFs with large pore sizes.[197,198] Additionally, as-synthesized SURMOFs are inherently amenable to AFM characterization since they are immobilized on solid substrates.

Using surface patterning to monitor thin film growth. A groundbreaking methodology for tracking epitaxial LbL growth emerged through the innovative application of micro-contact printing to pattern micrometer-sized squares of COOH-terminated SAMs on Au(111) substrates functionalized with CH_3-terminated SAMs (Fig. 12).[84] This approach utilized thiols of identical molecular lengths—16-mercaptohexadecanoic acid (**MHDA**) and hexadecanethiol (**HDT**)—to create chemically distinct regions on Au(111) while maintaining topographical uniformity. AFM topography images (Fig. 12(a)) reveal no height difference between the two molecules; however, their distinct

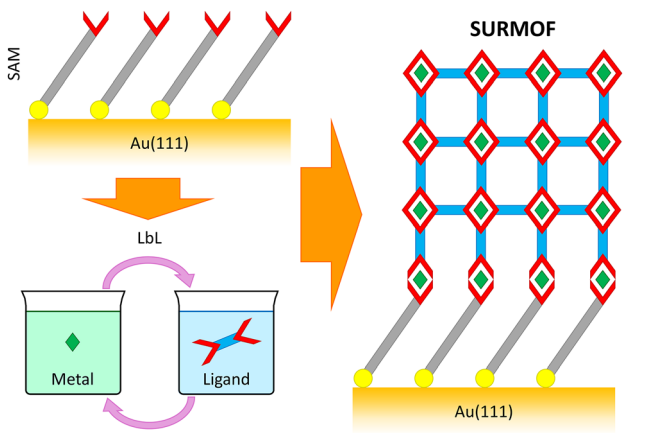

Scheme 5 LPE method for the growth of SURMOFs on SAM-functionalized Au(111).

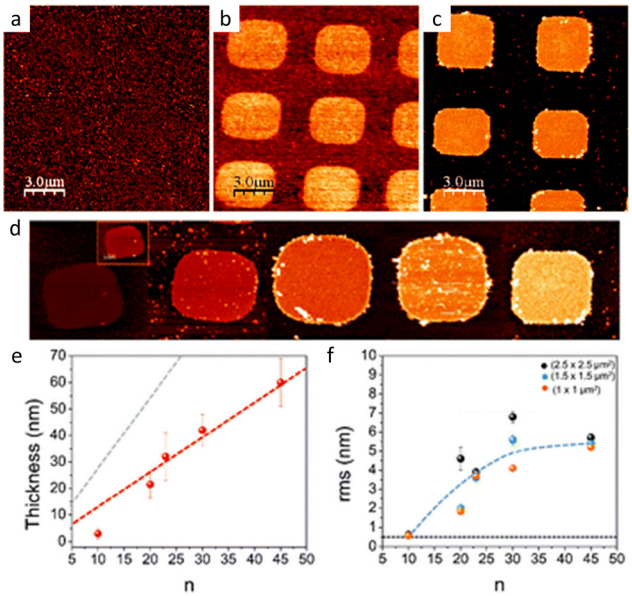

Fig. 12 Selective **HKUST-1** growth with the LbL approach on patterned surfaces. (a) AFM topographic and (b) friction images for the SAM patterned substrate before SURMOF growth. (c) AFM topography for a patterned sample after 45 immersion cycles. (d) Series of topographic AFM images for different samples corresponding to n = 10, 20, 23, 30 and 45 immersion cycles, from left to right, respectively. The total color scale (total height range) is 110 nm for all the images. Due to the low topography of the 10 cycles sample, the inset shows the same image with the vertical scale magnified by a factor of two. (e) Film thickness as a function of the number of immersion cycles. The red dashed line corresponds to the proposed "half-layer" growth whereas the grey one would correspond to a one-unit cell or complete layer growth. (f) Root mean square (rms) surface roughness as a function of the number of immersion cycles calculated for different scan sizes (see inset). The black horizontal line corresponds to the rms of the starting substrate while the blue dashed line has been drawn just as a visual aid. Error bars are the standard deviation values. Adapted with permission from ref. 84. Copyright©2008 The Royal Society of Chemistry.

terminal groups generate measurable variations in lateral friction forces between the sample and AFM tip. As a result, **MHDA** SAM regions display a brighter contrast, whereas **HDT** regions appear darker in AFM friction images (Fig. 12(b)).

HKUST-1 selectively grows on **MHDA** regions, as confirmed by topography AFM images, where the MOF thin films appear as bright squares, as shown in Fig. 12(c). This approach enabled film thickness quantification as a function of LbL cycles by measuring the height of the bright (MOF-covered) squares compared with the dark (MOF-free) areas. Notably, this measurement is impossible for extended films. Systematic thickness analysis across 10, 20, 23, 30, and 45 immersion cycles (Fig. 12(e)) revealed the mechanism underlying the growth process: after 20 cycles, thickness increase follows a strictly linear trend, establishing the existence of a "critical thickness" threshold beyond which a steady LbL growth regime dominates. The measured thickness increase of 1.317 nm per complete cycle, corresponding to half the **HKUST-1** unit cell length (2.634 nm), provided direct experimental validation of the expected growth behavior based on the known crystal structure. This finding confirms the epitaxial relationship between substrate and MOF structure, where every second **BTC** layer is shifted relative to the first, requiring two LbL cycles to complete one crystallographic unit cell. AFM measurements also revealed that surface roughness reaches a steady value for high cycle numbers (Fig. 12(f)), providing direct evidence for LbL completion mechanisms rather than island growth modes.

Building upon this patterning approach, nanografting techniques offered an alternative strategy for *in situ* surface modification through AFM-mediated molecular replacement.[199] This method involves removing matrix molecules in selected areas with an AFM tip while the sample remains immersed in COOH-terminated thiol solutions, enabling precise replacement of alkyl thiols with carboxyl-terminated alternatives. **MHDA** was grafted within a 1-octadecanethiol (**ODT**) matrix on Au(111), with subsequent **HKUST-1** growth on these functionalized surfaces.

The **MHDA/ODT** combination revealed critical limitations, producing SURMOFs with elevated surface roughness (28.9 ± 3.9 nm) and detecting small crystals of comparable height on the **ODT** layer, indicating uncontrolled **ODT** displacement by **MHDA** molecules. This observation established that thiol selection represents a crucial parameter governing SURMOF quality, with molecular compatibility between matrix and patterned regions proving essential for maintaining pattern fidelity. These investigations demonstrated the broader potential of spatially controlled MOF growth while defining critical design principles for multi-component surface functionalization strategies.

Investigating nucleation and growth of SURMOFs. Fundamental insights into **HKUST-1** nucleation and growth mechanisms emerged from systematic investigations of the initial 10 LbL deposition cycles on **MHDA** SAMs at both 25 °C and 50 °C.[200] These studies revealed that nucleation proceeds through island formation across the surface, indicating a Volmer–Weber growth mechanism in the early deposition stages. This finding challenges previous assumptions about uniform layer growth.[201]

Temperature effects proved particularly striking: synthesis conducted at an elevated temperature (50 °C) dramatically increased nucleation density, resulting in enhanced surface coverage and reduced overall roughness compared to ambient temperature conditions. Most significantly, temperature-dependent morphological control was demonstrated through distinct crystallite geometries: trigonal prismatic shapes dominated at 50 °C, while square pyramidal morphologies were characteristic of growth at 25 °C. This discovery challenged the prevailing paradigm that crystal morphology derives exclusively from substrate functionalization, revealing instead that thermal conditions exert equally critical influence over the final crystal architecture. These findings established temperature as a primary control parameter for MOF morphology engineering, expanding the toolkit for tailoring SURMOF properties beyond substrate-based approaches.

***In situ* studies to evaluate SURMOF stability.** Significant insights into SURMOF mechanical and thermal stability

emerged through the development of specialized autoclave-inserted AFM systems capable of *in situ* investigations under varying temperature and pressure conditions.[202] **HKUST-1** SURMOF stability studies revealed remarkable pressure tolerance, with thin films maintaining structural integrity under nitrogen pressures of up to 20 bar while exhibiting approximately 22% reversible shrinkage at 10 bar. The observed shrinkage behavior was attributed to physical compression of **BTC** linkers. This finding established the mechanical robustness of SURMOFs under high-pressure conditions.

Thermal stability investigations yielded unexpected results that challenged established assumptions about **HKUST-1** thermal properties. Material degradation occurred at surprisingly low temperatures (40–60 °C), despite reported bulk thermal stability. Critical methodological insights emerged from comparing *in situ versus ex situ* characterization: while *in situ* AFM revealed ~65% reduction in grain features, *ex situ* measurements showed only ~10% decrease. This discrepancy was attributed to scanning artifacts arising from enhanced thin film mobility at elevated temperatures, causing AFM tip-induced removal of surface features. It must be noted that the films used in this study were grown for just 5 LbL cycles and were intentionally made inhomogeneous through incomplete washing steps, which likely made them less stable than fully grown crystals. Nonetheless, these investigations demonstrated *in situ* AFM to be a potentially important tool for understanding MOF stability under realistic operating conditions while revealing the critical importance of experimental methodology in stability assessments.

Exploring alternative thin films synthesis routes. Alternative synthesis methodologies emerged through the development of vapor-assisted approaches, combined with solution processing techniques. The epitaxial growth of copper-5,10,15,20-tetrakis(4-carboxyphenyl)-porphyrin (**Cu-H2TCPP**) MOF thin films on HOPG was achieved through alternating vapor treatment with acetic acid and spin-coating of precursors.[203] AFM investigations revealed that acetic acid vapor effectively catalyzes the reorganization of ligand and metal precursors into single-layered structures, with successive cycles producing multilayered architectures. Although the crystal structure of these layered features has not been explored in detail, phase images revealed differences in contrast, suggesting that crystalline layers with varying orientations were adsorbed on the substrate. This vapor-solution hybrid approach demonstrates significant potential for controlling MOF thin film growth, representing a departure from traditional liquid-phase synthesis methods while highlighting the need for comprehensive structural analysis of the resulting films.

AFM-IR for the investigation of MOF dynamics. The coupling of AFM with IR spectroscopy proved particularly valuable for addressing questions about SURMOF growth mechanisms that remained unresolved through morphological studies alone. AFM-IR investigations of **HKUST-1** growth dynamics revealed that epitaxial development does not proceed *via* the previously assumed strict LbL mechanism.[85] Instead, growth occurs through a partial in-solution process involving **Cu-BTC** SBU formation, with these preformed units subsequently incorporating into the SURMOF structure.

The chemical sensitivity of AFM-IR enabled detection of (partially) unexchanged $[Cu_2(OAc)_4]$ paddlewheels within **HKUST-1** films. These paddlewheels, likely physisorbed onto the crystal even after washing and drying, contribute to defects in the SURMOF. To address this issue, the study suggests using $Cu(NO_3)_2$ as the metal precursor instead of $Cu(OAc)_2$, as the former exhibits lower steric hindrance and weaker surface affinity, reducing defect formation.

Building upon these mechanistic insights, AFM-IR enabled sophisticated investigations of guest–host interactions through the fabrication of bifunctional surfaces containing both hydrophilic and hydrophobic MOF domains.[204] Patterned Au(111) surfaces functionalized with 4-(mercaptomethyl)-benzoic acid (**MMBA**) and 4-mercaptopyridine (**MPyr**) SAMs, separated by 1-undecanethiol (**UDT**) SAM regions, were fabricated to epitaxially grow two different MOFs: the hydrophilic **HKUST-1** and the hydrophobic **ZIF-8**, the latter composed of 2-methylimidazolate ligands and Zn^{2+} cations (Fig. 13(a)). The distinct morphologies of these MOFs allowed for differentiation in AFM topography, with **HKUST-1** forming triangular {100} surfaces and **ZIF-8** presenting octahedral crystals (indicated by the yellow and red markers in Fig. 13(c), respectively). AFM-IR provided definitive chemical confirmation of these assignments and revealed framework-specific responses to environmental changes.

Water adsorption studies demonstrated the power of AFM-IR for probing guest–host dynamics: **HKUST-1** exhibited spectral changes upon N_2 purging attributed to water desorption, while **ZIF-8** domains remained spectroscopically unchanged (Fig. 13(d)). D_2O backfilling experiments provided molecular-level insights into hydration mechanisms, with new bands at 890 cm^{-1} (adsorbed D_2O) and 1725 cm^{-1} (deuterated carboxylic acid groups) confirming water adsorption in **HKUST-1** while **ZIF-8** remained unaffected (Fig. 13(f)). These findings provide direct experimental validation of a previously proposed water adsorption mechanism, which can occur either at the axial or equatorial positions at Cu(II) centers. The latter instance promotes D_2O dissociative adsorption, which eventually leads to the cleavage of metal–carboxylate bonds, contributing to the hydrolytic degradation of the framework. In summary, this work presents an efficient method to fabricate a bifunctional surface using epitaxial MOFs and provides new insights into the molecular processes occurring in MOF-based materials.

The integration of external stimuli with AFM-IR opened up new frontiers in understanding dynamic MOF behavior under operational conditions. Investigations of rotor dynamics in **Cu_2(F-BDC)$_2$(DABCO)** (**F-BDC** = 2-fluorobenzene-1,4-dicarboxylate and **DABCO** = 1,4-diazabicyclo[2.2.2]octane) thin films under external electric fields demonstrated the technique's versatility for probing stimuli-responsive behavior.[205] Thin films of **Cu_2(F-BDC)$_2$(DABCO)** were epitaxially grown on gold wafers functionalized with **MHDA** as well as $SrTiO_3$ substrates. By connecting both the substrate and AFM probe to an external power supply, force modulation through AFM setpoint adjustment enabled precise control over measurement conditions. AFM-IR measurements conducted under an applied electric field revealed inhibition of rotational motions parallel to the field direction, with this effect tunable through mechanical force exerted by the AFM

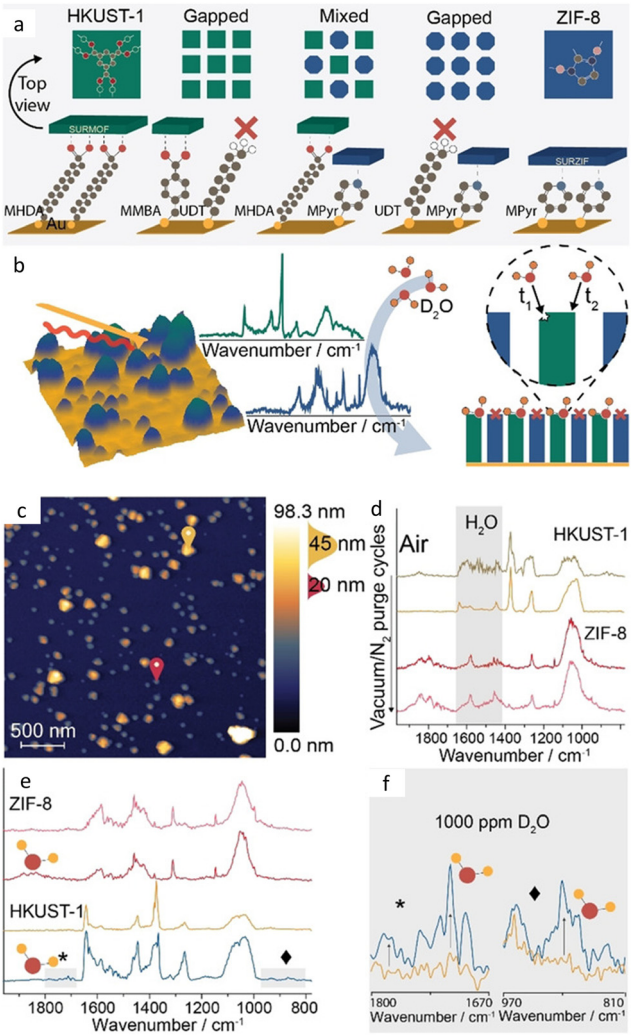

Fig. 13 Top: Outline of the mixed MOF approach. (a) Different thiol compositions were used for Au substrate functionalization prior to LbL synthesis of SURMOFs. **HKUST-1** (green) selectively grows on carboxylic acid-terminating SAMs, whereas **ZIF-8** (blue) growth is promoted on pyridine-terminating SAMs. Methyl-thiols were used to suppress growth. (b) Left: *In situ* AFM-IR was carried out on these SURMOFs to deduce their interaction with D_2O at the nanoscale. Right: Amphiphilic nature of the mixed **HKUST-1**/**ZIF-8** surface revealed by *in situ* AFM-IR. (c) AFM image of 10 layers of **HKUST-1**/**ZIF-8** grown on **MPyr**/**MHDA**. Point spectra were taken before and after vacuum/N_2 purge cycles at the locations marked yellow for **HKUST-1** and red for **ZIF-8**. (d) IR spectra showing the removal of water from **HKUST-1** and the water-independent IR spectra of **ZIF-8**. (e) IR spectra of **HKUST-1** and **ZIF-8** after the introduction of 1000 ppm D_2O. (f) Zoom-in IR spectra of the two areas marked in (e) highlighting the appearance of new peaks in the **HKUST-1** spectrum. Adapted from ref. 204.©2020 The Authors. Angewandte Chemie International Edition published by Wiley-VCH GmbH.

probe. This work established direct correlations between external stimuli and molecular rotor dynamics, demonstrating AFM-IR as a powerful tool for understanding responsive MOF behavior under realistic operating conditions.

4.2 MOF nanoparticles

3D MOFs are commonly synthesized *via* solution-based methods at temperatures ranging from 25 to 220 °C, often using solvothermal conditions. The precursors are typically mixed in a reaction vessel or an autoclave for several hours or even days until crystals are formed. Alternative synthesis methods, such as microwave-assisted, mechanochemical, electrochemical, or ultrasound techniques, offer more efficient and environmentally friendly options by avoiding direct heating of the precursor mixture. These methods enable reactions to occur at lower temperatures, offering more economical and sustainable alternatives to solvothermal approaches.[206,207]

The investigation of MOF crystal surfaces provides critical insights into material structure and structure–function relationships, as surface transformations may be indicative of related bulk processes occurring within the framework. Characterizing MOF nanoparticles with SPM techniques presents unique challenges, in particular, the immobilization of small crystals on substrates for high-resolution imaging. This limitation has driven the development of innovative approaches, including the use of SAM-functionalized substrates for direct crystal growth, enabling unprecedented real-time observations of nucleation and growth dynamics. In contrast with the LbL approach described in the previous section, growth of 3D MOFs on functionalized substrates occurs by immersing the substrates in a solution of both the metal and ligand precursors.

Investigating nucleation and growth of MOF crystals. The observation of real-time MOF crystal growth through liquid AFM imaging of **HKUST-1** nanoparticles that were set on metal alloy substrates revealed the dynamic nature of two-dimensional secondary nucleation.[83] By imaging the {111} facet of **HKUST-1** crystals immersed in their growth solution, it was demonstrated that surface nuclei formation and lateral spreading initially occur simultaneously. After nine minutes, the reduction in supersaturation shifted the dominant process from nucleation to lateral growth of existing nuclei. Notably, the study revealed how line defects initially impede lateral growth but ultimately become incorporated into the bulk crystal through island coalescence, establishing a direct link between surface growth dynamics and final material properties. Cross-section profiles of **HKUST-1** hillocks showed that most step edges corresponded to the stable 1.5 nm d_{111} crystal spacing, although multiples of the 0.76 nm d_{222} crystal spacing were also observed.

Building upon these observations, the authors employed SAM-functionalized gold substrates to gain deeper insights into the growth mechanism for **HKUST-1**.[208] The key discovery was that crystal growth can initiate from single nucleation points rather than multiple simultaneous sites. The authors attributed this difference to the smaller variations in crystal size and lower defect concentration in the present study, which, in contrast, were both larger in the earlier studies. Furthermore, the discrepancy may stem from differences in the solvent system: the initial experiments used an *N*,*N*-dimethylformamide (DMF) solution, while the later investigations employed a water–ethanol mixture, highlighting the importance of the solvent as a critical parameter for controlling growth pathway selection.

The influence of temperature on MOF nucleation was systematically elucidated through AFM-IR imaging of **HKUST-1** growth on **MHDA** SAMs across three distinct temperature

regimes—13, 25, and 50 °C.[209] This comprehensive study established that crystallization follows the Volmer–Weber model, producing 3D islands rather than uniform films. The temperature-dependent behavior revealed three distinct growth regimes: continuous nucleation and growth at 25 °C, creating both large grains and background ''carpet'' layers, incomplete growth at 13 °C due to kinetic limitations, and premature nucleation termination at 50 °C caused by SAM desorption.

From this work emerges an important limitation of SAM functionalization for anchoring MOF crystals to substrates, which is the thermal stability of the SAM. This moderate thermal stability limits the possibility of exploring various experimental conditions, including performing temperature-dependent studies.

Developing alternative anchoring strategies to obtain mechanistic insights. An elegant alternative to SAM-functionalized substrates is the immersion of glass slides into the MOF growth solution for obtaining surface-anchored MOFs. **ZIF-8** and **MOF-5**, a cubic MOF composed of $(Zn_4O)^{6+}$ metal nodes linked by **BDC**, were characterized by *in situ* liquid AFM using this approach.[210,211] The study on **ZIF-8** revealed that crystal growth occurs through the correlated incorporation of individual monomeric species, where the attachment of one ligand influences the positioning of subsequent ligands. This discovery highlighted the previously underappreciated role of non-framework species, particularly solvent molecules, in mediating binding interactions and facilitating ordered growth processes.[210]

MOF-5 was observed to follow a similar growth process.[211] Additionally, it was found that the ligand-to-metal stoichiometry of the growth solution plays a crucial role in determining the morphology of the resulting crystals through differential directional growth rates. When the metal-to-ligand ratio is greater than 1, the growth rate along the [111] direction is slower than along the [110] direction, and large square terraces are formed. When the metal-to-ligand ratio is approximately 1, the growth rate along the [111] direction remains slower than along the [110] direction, and the resulting morphology consists of rhombus-shaped terraces; however, these are not squares. This indicates that subtle variations in the precursor ratio can significantly influence the final crystal structure and surface topography of **MOF-5**, opening up possibilities for MOF crystal shape engineering.

The controlled SBU approach (CSA) for MOF synthesis was validated through systematic liquid AFM studies of surface nucleation of **MOF-5**.[212] This approach consists of the use of monotopic ligands and metal ions to form pre-assembled coordination complexes. Such pre-organization results in faster reaction times during MOF growth. To elucidate the mechanism of this process, nucleation seeds were grown on glass substrates, and 2D surface nucleation was investigated using liquid AFM in diluted **MOF-5** growth solution. This study revealed that the CSA does not proceed through direct substitution of surface dangling **BDC** ligands by $[ZnO_4(O_2CC_6H_5)_6]$ SBUs as initially hypothesized. Instead, topographical measurements revealed that partial SBU dissociation precedes framework incorporation, substantially revising the understanding of how pre-assembled building blocks participate in MOF construction.

Investigating the mismatch effects. The complexity of MOF interfacial growth was further elucidated through investigations of core–shell heterostructures, where **Zn_2(NDC)$_2$(DABCO)** (**NDC** = 1,4-naphthalenedicarboxylate) cores were used as templates for **Cu_2(NDC)$_2$(DABCO)** shell growth.[213] This study revealed the impact of slight lattice mismatches in core–shell MOF growth. It was found that core–shell MOF growth proceeds through in-plane rotational epitaxy rather than perfect lattice matching, with the Cu framework exhibiting a systematic 5.9° rotational misalignment relative to the Zn-MOF core structure.

The study established that supersaturation conditions play a decisive role in directing this unconventional growth mode, providing quantitative parameters for interfacial engineering in MOF heterostructures. Moreover, these results show that isostructural MOFs exhibit nearly identical growth mechanisms.

By controlling lattice mismatch, it becomes possible to engineer specific interfacial orientations and properties in core–shell architectures. This mechanistic insight bridges the gap between single-phase MOF growth and complex multicomponent systems, establishing a framework for the design of MOF heterostructures with tailored interfacial properties.

Direct observation of framework flexibility mechanism. The first nanoscale visualization of MOF flexibility dynamics was achieved through *in situ* high-speed AFM imaging of **Ga-MIL-53** [Ga(OH)(**BDC**)] during guest exchange transformations between DMF and EtOH-containing phases (Fig. 14).[68] This pioneering study established that flexible MOFs undergo structural transformations through an LbL shear mechanism, addressing long-standing questions about the nanoscale origins of framework flexibility. The critical breakthrough was demonstrating that flexing occurs through propagating wavefronts of cooperatively transforming unit cell layers, rather than uniform or random structural changes throughout the crystal.

The expansion transformation from **Ga-MIL-53**·0.96DMF to **Ga-MIL-53**·*x*EtOH revealed wavefronts traveling at constant velocities of approximately 0.9 μm min^{-1} across {011} facets, shown in the image sequence in Fig. 14(a)–(h). This image sequence indicated Case II non-Fickian diffusion behavior, where transformation kinetics are controlled by framework expansion rather than guest diffusion. Quantitative analysis demonstrated that individual wavefronts involve at least 76 unit cells in depth and 1429 unit cells laterally, establishing the cooperative scale of structural transformations. The observation that consecutive rows of unit cells parallel to the (011) plane transform cooperatively, followed by adjacent row transformation in the [100] direction (Fig. 14(i)), provided direct evidence for the row-by-row shear mechanism underlying framework flexibility.

The reverse contraction transformation from **Ga-MIL-53**·*x*EtOH to **Ga-MIL-53**·0.96DMF proceeded through a crystallographically distinct mechanism involving shearing parallel to the $(01Mx\bar{0}31;)$ at 0.6 μm min^{-1} (Fig. 14(r)). The image

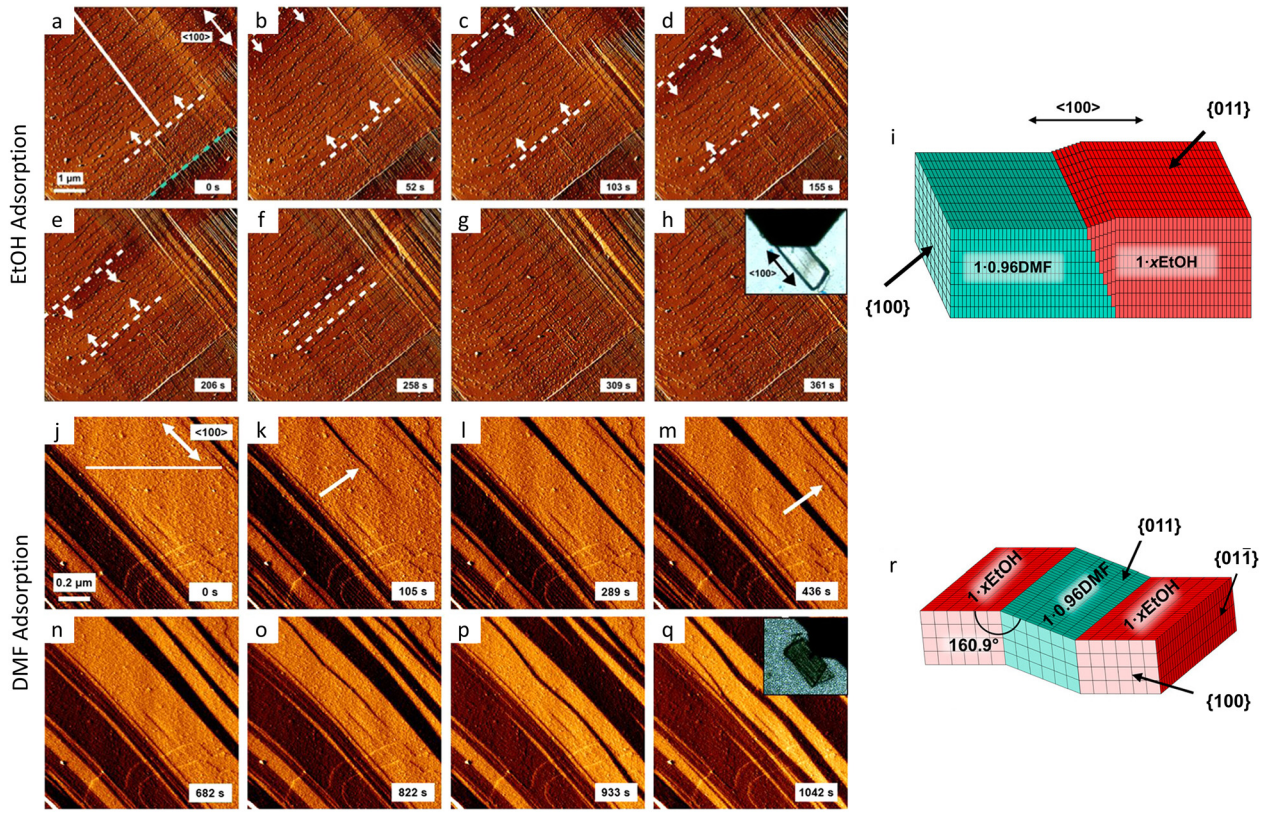

Fig. 14 Real-time *in situ* imaging of guest-induced flexing mechanism in **Ga-MIL-53**. (a)–(h) Error signal AFM images of a {011} facet during pore expansion induced by EtOH adsorption. Image size: 6.0 × 6.0 μm^2. The white dashed lines in (a)–(f) indicate the wavefronts and the white arrows their propagation directions. The green dashed line in (a) indicates a defect. Inset in (h) is an optical microscope image of a **Ga-MIL-53** immerged in DMF prior to transformation. (i) Schematic representation of the expansion process. (j)–(q) Error signal AFM images of a {011} facet during pore contraction induced by DMF. Transforming parts of the crystals are indicated by white arrows in (k) and (m). Inset in (q) is an optical microscope image of a **Ga-MIL-53** immerged in EtOH prior to transformation. (r) Schematic representation of the contraction process. Adapted from ref. 68.

sequence of the transformation is presented in Fig. 14(j)–(q). The measured interface angle of 162.1° ± 1.1° between coexisting phases showed excellent agreement with crystallographically predicted values (160.9°), validating the coexistence of phases with different expansion degrees within single crystals. This phase coexistence represents a paradigm shift in understanding MOF flexibility, demonstrating that transformation gradients rather than uniform phase changes characterize flexible framework behavior.

The study revealed that structural transformations create characteristic surface textures, including ridges formed by opposing shears on adjoining unit cell layers parallel to (011) planes. These features serve as stress relief mechanisms accommodating volume changes during transformation and provide diagnostic signatures of flexibility mechanisms.

The ability demonstrated in this work to visualize phase boundaries, measure transformation kinetics, and quantify structural parameters during dynamic processes establishes *in situ* AFM as a valuable technique for understanding framework flexibility. These insights have profound implications for designing flexible MOFs with controlled transformation properties and predicting their behavior in applications requiring reversible structural changes.

Molecular-resolution imaging of surface dynamics. The achievement of molecular-resolution imaging of MOF surfaces under dynamic conditions represents a pivotal advancement in understanding surface-specific phenomena that differ markedly from bulk behavior. High-speed liquid AFM imaging of **Zn_2(1,4-NDC)$_2$(DABCO)** surfaces enabled real-time observation of guest-induced structural transformations at the liquid–solid interface. (Fig. 15).[69] This breakthrough demonstrated that MOF surfaces exhibit remarkable responsiveness to guest molecules under conditions that barely affect bulk crystal structure, revealing a dichotomy between surface and bulk framework behavior.

In this work, a MOF crystal was glued on a steel disk and imaged in DMF. A representative high-resolution AFM image is shown in Fig. 15(b), while Fig. 15(c) is the corresponding 2D fast Fourier transform (2D FFT). Subsequently, a solution of biphenyl was injected into the AFM liquid cell. During real-time imaging, it was found that biphenyl guest injection induced reversible unit cell transformations from tetragonal (α = 89.6°) to rhombohedral ($\alpha \approx 87°$) structures exclusively at the crystal surface, while powder XRD analysis confirmed that bulk crystals remained unchanged even after extended exposure. This surface-selective responsiveness demonstrates that the reactivity of framework surfaces is different from bulk phases,

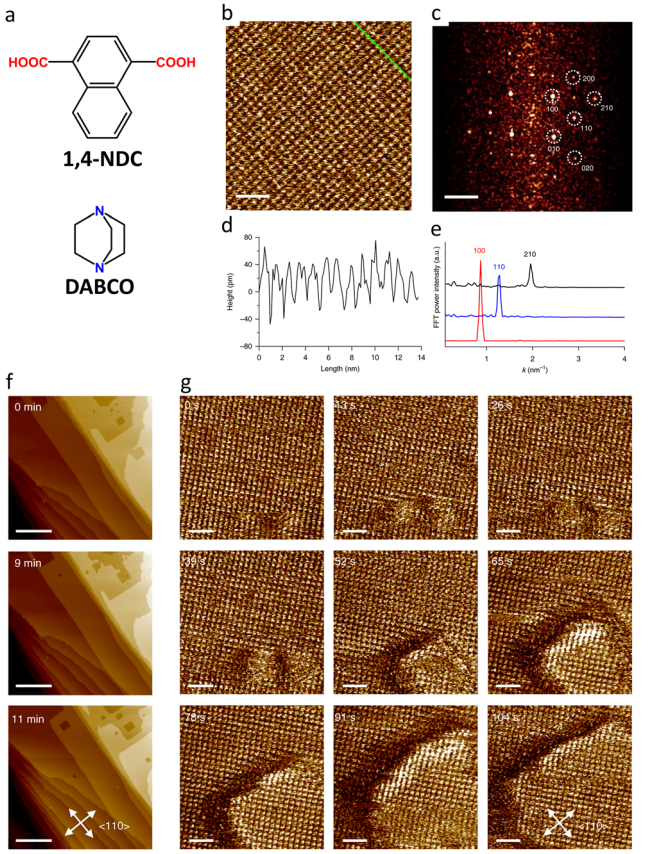

Fig. 15 *In Situ* molecular resolution AFM imaging of **Zn_2(1,4-NDC)$_2$-(DABCO)**. (a) Molecular structures of **DABCO** and **1,4-NDC** (b) High-resolution AFM topography of **Zn_2(1,4-NDC)$_2$(DABCO)** imaged in DMF (scale bar: 5 nm) and (c) corresponding 2D FFT spectrum (scale bar: 1 nm^{-1}). (d) Height profile along the green line in (b). (e) 1D FFT power spectra. (f) Large scale AFM topography images captured 0, 9, and 11 minutes after the injection of a 200 mM **BPY** solution (scale bars: 250 nm). (g) High-resolution AFM phase images of the **Zn_2(1,4-NDC)$_2$(DABCO)** surface under the same conditions as in (g) collected 13 seconds apart, depicting the **BPY**-induced layer-by-layer exfoliation at the molecular level (scale bar: 5 nm). Adapted with permission from ref. 69. Copyright©2018, The Author(s), under exclusive license to Springer Nature Limited.

experiencing dynamic coordination equilibria and enhanced structural flexibility due to reduced bonding connectivity at interfaces.

These observations suggest that surface structural changes possibly follow stochastic rather than cooperative mechanisms, contrasting sharply with the cooperative LbL shear transformations observed in bulk flexible frameworks. Deformation events occurred within approximately 10 minutes of guest concentration changes, with statistical analysis indicating that individual, competing adsorption/desorption of guest and solvent molecules seemingly trigger localized lattice modifications. Perhaps most remarkably, the introduction of competing ligands (4,4′-bipyridine (**BPY**) and 1,2-di(4-pyridyl)ethylene (**DPYE**)) enabled real-time visualization of LbL delamination processes along specific crystallographic directions. The delamination process is evident from the large-scale AFM topography images shown in Fig. 15(f), where pits with regular edges form and grow with time. The phase images presented in Fig. 15(g) show the formation of a delamination pit with molecular resolution. The directional preference for ⟨110⟩ delamination was rationalized through surface energy considerations based on sub-building unit saturation numbers, where {110} planes with two unsaturated coordination sites exhibit higher surface energies than {100} planes with single unsaturated sites.

This work provides a new perspective on our understanding of MOF surface behavior, demonstrating that surfaces represent distinct chemical environments with unique responsiveness and transformation mechanisms that complement but differ from the cooperative bulk flexibility mechanisms observed in framework transformations.

From the works reviewed in this section, it emerges that AFM characterization of MOF thin films and nanoparticles is well-established. This technique enables not only the determination of crystal morphological features—such as roughness and height—but also the elucidation of dynamic processes essential to MOF research, including crystal growth, guest adsorption, phase transitions, solvent-induced degradation, and delamination. In most studies, epitaxial growth and MOF immobilization have been performed on gold substrates functionalized with SAMs. Despite experimental evidence highlighting the influence of the substrate on MOF morphology, the exploration of alternative substrates and anchoring strategies remains limited. Moreover, manually gluing a single crystal onto a sample disk is only feasible when relatively large crystals can be obtained.

The potential for molecular-resolution imaging of MOF surfaces remains largely unexplored, likely due to the technical challenges associated with the approach. Achieving molecular resolution in liquid AFM requires firm immobilization of the crystals on the substrate in such a way that the crystal surface remains parallel to the scan direction.

5. Discrete metallosupramolecular architectures

Like for extended MOCNs, DMSAs have been investigated by SPM. In this section, studies will be presented that can be broadly categorized into two groups. Firstly, the use of ambient STM to investigate the on-surface self-assembly of preformed metal–organic architectures that have already been structurally characterized. Secondly, seminal work primarily demonstrating how UHV-STM can be employed to structurally characterize metal–organic architectures will be discussed.

5.1 Self-assembled networks of DMSAs

Pre-formed metal–organic architectures, structurally characterized in solution, the gas phase, and the solid-state by techniques such as NMR spectroscopy, MS, and SC-XRD, respectively, have been demonstrated to self-assemble into networks at the liquid–solid interface, which can be characterized by STM under ambient conditions.[76–78,214–218] On-surface assemblies characterized by STM (performed in solution or in air) include

those consisting of 2D—rhombic (Fig. 16(a))[76–78] and rectangular (Fig. 16(b))[78,215]—metallosupramolecular species and also 3D—trigonal bipyramidal (Fig. 16(c))[78] and trigonal prismatic[218]—architectures.

Impact of assembly conditions on SAMNs of DMSAs. The (sub)molecular level spatial resolution of the STM imaging was exploited to reveal the difference in the orientation of a metallosupramolecular rectangle upon changing the substrate from HOPG to Au(111).[215] On HOPG, the rectangles are oriented edge-on, whereas they orient face-on when assembled on Au(111).

In work investigating the on-surface organization of metal–organic squares, the opening of these squares to form short oligomer chains under acidic conditions was revealed by STM and further supported by NMR studies.[76] The high resolution of the STM images made the inspection of individual metal–organic species possible, and thus each species could be assigned as either the closed metal–organic square or oligomer chain.

Unravelling the structures of assembled networks formed by the co-adsorption of different types of DMSAs. The ability to distinguish between different species on an individual basis provides a platform for analyzing assembled networks containing more than one component. In three different studies, a variety of outcomes were observed. The simultaneous assembly of 2D metallosupramolecular rectangles and 3D trigonal bipyramids on a Au(111) surface formed separate domains of each structure type.[78] In contrast, upon co-deposition onto an HOPG surface of 1,3,5-tris(10-carboxydecyloxy)-benzene and a metal–organic rectangle, a multicomponent network was observed.[217] This network, observed by STM, was attributed to consist of the metal–organic rectangles residing within the pores of a network formed by 1,3,5-tris(10-carboxydecyloxy)-benzene. When the same metallosupramolecular rectangle was deposited onto an assembled molecular network of shape-persistent macrocycles, the rectangles formed a second layer by residing on top of the macrocyclic moieties.[216] Confinement of the metal–organic rectangles within the pores of the macrocycles was not expected due to the diameter of the macrocyclic pores being seemingly smaller than the metal–organic rectangle dimensions, particularly along the long rectangular axis.

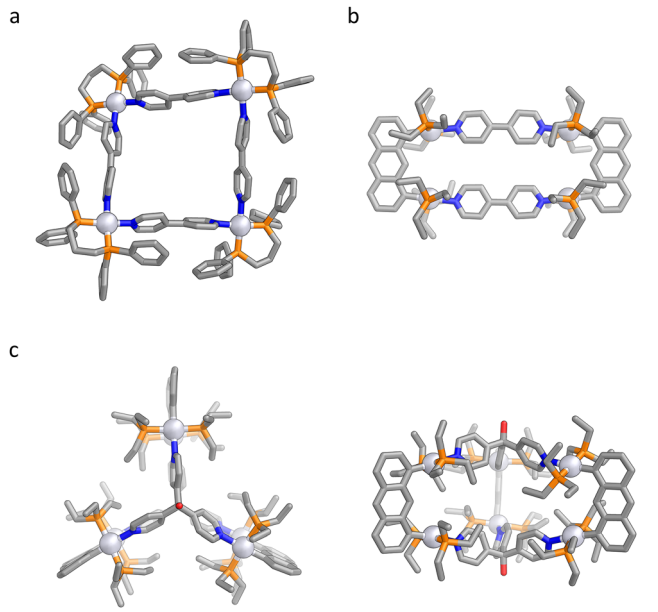

Fig. 16 X-ray crystal structures of discrete metallosupramolecular species assembled into SAMNs on surfaces and studied by ambient STM. (a) Square.[219] (b) Rectangle.[220] (c) Trigonal bipyramidal cage.[221] Solvent, counterions, disorder and hydrogen atoms are omitted for clarity. Pt(II): silver, C: grey, N: blue, P: orange, O: red.

5.2 Structural characterization of DMSAs

In the above examples, the metal–organic architectures had been structurally characterized prior to their assembly on the surface; it is the on-surface assembly of these species that is then characterized by STM. SPM techniques have, however, also been used to structurally characterize discrete metal–organic species, which in some cases have highly complex structures.

Structure-type characterization. UHV low-temperature STM (UHV-LT-STM) has been employed, alongside NMR spectroscopy and MS techniques, to structurally characterize discrete metal–organic hexagonal wreaths.[222,223] In these cases, sample preparation mainly consisted of adding a droplet of a solution of the pre-formed hexagonal wreath to a freshly cleaned and annealed Ag(111) surface. In work demonstrating the formation of distinct structure types from ligands with the same core geometry, STM and AFM provided supporting evidence for the formation of metal–organic species with discrete hexagonal wreath and polymeric—helical or ladder—structures, depending on the conditions used for their preparation.[224]

Assignment of isomers arising from reduced-symmetry ligands. The geometry of tetrakis(tridentate) ligand **DLL1** (Fig. 17(a)) is key to its preference for forming hexameric double-layered metal–organic macrocycles (**DLM1**), when combined with $Zn(NO_3)_2{\cdot}6H_2O$ in the ratio 1 : 2.[225] Two of the **DLL1** ligand arms form part of the outer ring of the double-layered macrocycle, and the remaining two arms form part of the inner ring. When six **DLL1** ligands and twelve Zn(II) cations combine to form the double-layered macrocycle **DLM1**, four distinct isomers (Fig. 17(b)–(i)) arise from two conformational isomers of ligand **DLL1** (Fig. 17(a)). Individual ligand units are in the same conformation (conformer 1 in Fig. 17(a)) within three of the isomers (Fig. 17(b), (d) and (f)); their difference comes from the relative orientation, and thus connectivity, of the six **DLL1** units that form the double-layered hexagon. In the fourth **DLM1** isomer (Fig. 17(h)), the ligand units adopt a different conformation (conformer 2 in Fig. 17(a)) compared with the conformations in the first three **DLM1** isomers.

UHV-LT-STM studies enabled the determination of the isomeric configuration of individual double-layered macrocycles (Fig. 17(c), (e), (g) and (i)), which was not possible using NMR spectroscopy and MS techniques. The authors assigned the isomeric configuration of a given **DLM1** on the basis of the angles between the straight lines connecting the two nearest neighbor "inner" and "outer" **TPY**-Zn(II)-**TPY** (where, **TPY** = 2,2′:6′,2″-terpyridine moiety) junctions (red dashed lines in Fig. 17), which

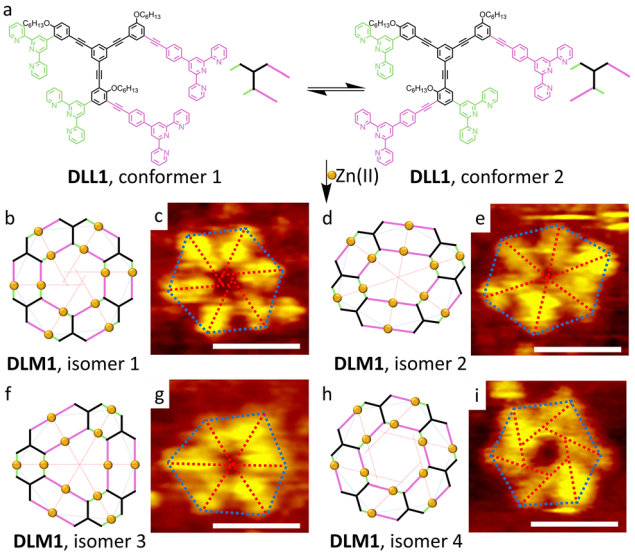

Fig. 17 Isomer assignment of individual metal–organic double-layered hexagons. (a) Ligand **DLL1** can exist in two distinct two-dimensional conformations. Ligand **DLL1** reacts with $Zn(NO_3)_2{\cdot}6H_2O$ to form Zn_{12}**DLL1**$_6$ double-layered macrocycles (**DLM1**). (b), (d), (f), (h) Schematic representations of the four isomers of the metallosupramolecular complex **DLM1**. (c), (e), (g), (i) STM images containing the double-layered macrocycle **DLM1** isomers displayed in b, d, f and h, respectively. The red and blue dashed lines are used to guide isomer assignment. Scale bars: 5 nm. Adapted with permission from ref. 225. Copyright©2021 American Chemical Society.

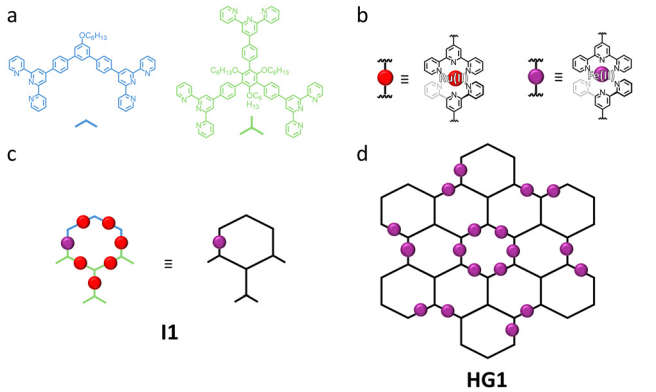

Fig. 18 Metal–organic hexagonal grid **HG1**; the relative positions of Ru(II) and Fe(II) cations, and thus the isomeric configuration, can be assigned for individual hexagonal grids.[226] (a) Molecular structures of the organic ligands used to assemble metal–organic intermediate **I1** and thus grid **HG1**. (b) **TPY**-Ru(II)-**TPY** and **TPY**-Fe(II)-**TPY** junctions. (c) Schematic representation of metal–organic intermediate **I1**. (d) Schematic representation of one of the several possible isomeric configurations of metal–organic grid **HG1**.

appear as bright spots in the STM images, and the lines describing a polygon by connecting the "outer" Zn(II) cations (blue dashed lines in Fig. 17).

Electrospray ionization-MS (ESI-MS) studies indicated that a hexamer:heptamer:octamer mixture formed when ligand **DLL1** was replaced by a ligand in which all three arms of the central core (colored black in the structures in Fig. 17(a)) were shortened. STM studies confirmed the presence of all three of these $Zn_{2x}L_x$ double-layered macrocycles. The formation of metal–organic structures, including the species with higher nuclearity, containing the ligand in conformation 2 only was attributed to the reduction in unfavorable steric clashes between **TPY**-Zn(II)-**TPY** junctions on the outer and inner rings.

Assignment of isomers arising from the relative positions of metal cations. In the case of hexagonal grid **HG1**, distinct isomers do not arise from the relative orientation and connectivity of reduced-symmetry ligands, instead, the relative positioning of Fe(II) cations gives rise to distinct isomers.[226] The hexagonal grid **HG1**, consisting of thirteen hexagons, is formed by joining together six preformed **I1** units (Fig. 18) using Fe(II) cations. The intermediate **I1** contains seven metal ions, six of these are Ru(II) and the remaining cation is Fe(II), as schematically depicted in Fig. 18(c). Although the position of this Fe(II) cation is fixed to one of four types of metal cation binding site in intermediate **I1**, the symmetry of **I1** is reduced, compared with if this Fe(II) was Ru(II).

When six intermediate **I1** units are combined to form a hexagonal grid **HG1**, distinct isomers form based upon the relative position of the six Fe(II) cations in the aforementioned site type. A schematic representation of one isomer of hexagonal grid **HG1** is displayed in Fig. 18(d). The presence of multiple isomers was hypothesized to broaden the signals in the ^{1}H NMR spectrum of **HG1**, due to the overlapping of signals for the different isomers. Distinct sets of signals for each isomer could not be identified in the ^{1}H NMR spectrum. UHV-LT-STM studies indicated the presence of hexagonal grid structures and the identification of the isomeric configuration adopted by a given **HG1** complex was achieved by combining STM with STS. STS was used to determine the energy gap between the HOMO (highest occupied molecular orbital) and LUMO (lowest unoccupied molecular orbital) at each metal center, which allowed each to be assigned as either Fe(II) or Ru(II), in turn allowing the assignment of the isomeric configuration of the complex being investigated. In a separate study, distinct isomers of hexagonal grids containing three different metal cations were similarly distinguished by using a combination of STM and STS data.[227] Hexameric units, with a similar core structure to intermediate **I1** before metalation with Fe(II), were used to form (metallo-)polymers.[228] These units were appended with two azide functional groups and underwent a copper(I)-catalyzed azide–alkyne cycloaddition (CuAAC) "click" reaction with a pentaethylene glycol derivative, terminated at each end by alkyne groups. Combined STM and STS studies similar to those conducted in the above work provided insights into the metal–organic species formed after the addition of Fe(II) cations to the (metallo-)polymers. The study demonstrated that species formed in which the Fe(II) cation was chelated by **TPY** units in the same hexameric unit to close the hexagon. It also occurred that hexameric units in a linear conformation were instead joined together.

The combination of synchrotron X-rays with STM (SX-STM) can provide detailed information about a single atom/ion.[229] The elemental identities of a Fe(II) cation chelated by two **TPY**

units in intermediate **I1**, and Tb(III) coordinated by three brominated pyridine-2,6-dicarboxamide ligands, were confirmed using STM-X-ray absorption spectroscopy (STM-XAS). Furthermore, the chemical states of Fe(II) and Tb(III) were confirmed by STM-near-edge X-ray absorption fine structure (STM-NEXAFS) spectra.

This section has demonstrated the power of SPM, in particular STM and STS, for the structural characterization of discrete metal–organic assemblies. The work discussed above indicates that UHV-LT-STM can be employed as a complementary technique to solution and gas-phase characterization techniques, namely NMR spectroscopy and MS, respectively. In several cases, it appears that the structures present in solution are the same as those observed on the surface, following their deposition.

6. Conclusions

This review has examined the current state and methodological advances in SPM techniques for the characterization of MOCNs, MOFs at various length scales, and DMSAs, summarized in Table 1. The analysis reveals that SPM methodologies have emerged as indispensable tools for elucidating structure–function relationships in these materials, complementary to X-ray and electron diffraction techniques. They offer unparalleled molecular-resolution insights into material surfaces that bridge

Table 1 Overview of the examples included in this review

Technique	Material	Experimental conditions	Information	Examples	Ref.
STM	MOCNs	UHV	Connectivity of the building blocks	Imaging of distinct crystalline and amorphous phases, coordination geometries, Kagome lattices, and quasicrystalline networks.	104, 105, 115, 123–127
			Chirality	Distinction of single enantiomers and enantiomorphous phases	71, 74, 145, 146
			Concentration and temperature	Exploit temperature and concentration as tunable parameters to fabricate distinct surface-supported MOCNs	125, 147–150
			Stability	Competition between kinetic and thermodynamic factors	151–153
			Substrate effect	Formation of new phases favored by substrate-building block interactions	114–157
			Quantification of crystallinity	Distinction and quantification of crystalline and amorphous phases in multicomponent systems	159
			Structure–function relationship	Magnetic anisotropy and magnetic coupling; tuning the magnetic properties using the isoreticular approach.	96, 119, 124–126, 128, 132, 133
		Liquid–solid interface	Structural control	Effect of synthesis protocol on the self-assembly outcome, control in the formation and quantification of amorphous and crystalline phases.	79–81
			Chirality	Metal-induced enantiomers separation and fabrication of enantiopure MOCNs aided by solvent selection.	80
			Porosity	Adsorption of guest molecules in the MOCN free pores	80, 81
	DMSAs	UHV	Structural characterization of DMSAs	Structure-type characterization	222–224
				Isomers assignment	225–227
		Liquid–solid and air–solid interface	Self-assembled networks of DMSAs	Impact of assembly conditions on SAMNs of DMSAs	76, 215
				Co-adsorption of different types of discrete architectures	78, 217
AFM	MOF thin films	Liquid–solid interface	Epitaxial growth	Use of patterned substrates	84, 199
			Nanoscale insights into nucleation and growth mechanisms	Temperature dependence of the LPE outcome	200, 201
			Stability	High-temperature and high-pressure tests	202
			Alternative synthesis routes	Vapor-assisted epitaxial growth of MOF thin films	203
	MOF nanoparticles		Observation of nucleation and growth	Distinction between nucleation and growth processes	83
				Relationship between nucleation and growth processes and experimental conditions	83, 208
			Elucidating the nucleation and growth mechanisms	Molecular insights into the nucleation and growth mechanisms and comparative studies across different MOFs	210–213
			Real-time observation of surface processes	Framework flexibility	68
				Molecular-resolution imaging of surface dynamics	69
AFM-IR	MOF thin films	Liquid–solid interface	Nanoscale Insights into nucleation and growth mechanisms	Elucidation of the LPE mechanism	85
			Chemical information	Water adsorption in samples patterned with different MOFs	85, 204
	MOF nanoparticles		Stimuli responsiveness	Characterization of molecular motion under an applied electric field	201
			Mechanistic insights	Temperature dependence of nucleation and growth processes	209

the gap between 2D surface-supported networks and 3D bulk frameworks.

The integration of STM and AFM techniques has considerably transformed our understanding of metal–organic coordination systems at the nanoscale. STM characterization under UHV conditions has demonstrated exceptional capabilities in providing molecular-level structural information for MOCNs, enabling the identification of local features and polymorphs, chirality differentiation, and the characterization of complex architectures, including quasicrystalline and amorphous phases. Similarly, UHV-STM has been demonstrated to be a valuable tool for the characterization of DMSAs, including complex mixtures of isomers. Notably, the extension of STM investigations of MOCNs to the liquid–solid interface represents a significant methodological advancement, allowing for real-time monitoring of solvent effects on network formation and guest adsorption and providing the capability to employ synthetic conditions that align with conventional MOF synthesis approaches.

AFM has proven to be valuable for characterizing MOF thin films and single crystals, offering unique capabilities for investigating dynamic processes such as crystal growth, guest adsorption, phase transitions, and structural degradation. The AFM-IR combination has further expanded the SPM analytical toolkit, enabling simultaneous topographical and chemical characterization of surface-supported MOF thin films and crystal surfaces with nanoscale spatial resolution.

Despite these remarkable advances, several challenges remain that limit the full potential of SPM characterization of metal–organic systems. The limited number of successful demonstrations of porous MOCN fabrication and STM characterization at the liquid–solid interface underscores the need for systematic methodological development in this area, which include targeting the control of molecular dynamics at the interface and achieving reproducible network formation in the presence of competing solvation and surface interactions. Such insights would be beneficial because MOCNs fabricated at the liquid–solid interface are more closely related to MOFs and in-depth studies on the structures and dynamics of the former can be relevant to advance our understanding of the latter.

An additional challenge relates to the statistical analysis using such local, small-scale techniques. The field currently lacks standardized methodologies for quantitatively assessing structural order and crystallinity in surface-supported monolayers, including MOCNs. This limitation hinders reproducible comparisons across different studies and impedes the development of structure–property correlations that are essential for rational material design.

The immobilization of MOF samples on solid substrates remains the primary technical barrier to achieving consistent molecular-resolution imaging of MOF particles. Current anchoring strategies, predominantly relying on SAMs on gold substrates, lack the versatility required for comprehensive investigations across diverse MOF systems. Furthermore, the substrate influence on MOF morphology and properties, while documented, remains inadequately understood and it would be beneficial for it to be explored in future works.

The convergence of experimental SPM techniques with computational modelling and machine learning approaches presents promising perspectives for advancing MOF characterization. Computational methods will be crucial for providing mechanistic insights into observed structural phenomena and for interpreting complex experimental data. Machine learning integration holds potential for the development of automated quantification algorithms and establishment of standardized analytical protocols for objective structural assessments of both extended networks and discrete supramolecules.

The continued refinement of SPM methodologies, coupled with the integration of complementary analytical techniques and computational approaches, will undoubtedly unlock new frontiers in our understanding of metal–organic systems, ultimately contributing to the design of materials with unprecedented functionality and performance in applications.

Conflicts of interest

There are no conflicts to declare.

Data availability

No primary research results, software or code have been included and no new data were generated or analyzed as part of this review.

Acknowledgements

This work was in part supported by Research Foundation – Flanders (FWO) (G0H2122N) and FNRS under the Excellence of Science (EOS) program (40007495). Additional support by FWO (G0A4120N, G0A5U24N, I006922N, G0K9822N) is acknowledged. A. C. acknowledges financial support through a FWO Fellowship (1159922N), J. A. D. acknowledges funding by the European Union under Horizon Europe, grant agreement ID: 101155157 (SURF-2DHYB). Financial support from KU Leuven-Internal Funds (C14/23/093) is acknowledged. S. D. F. acknowledges funding by the European Union under the Horizon Europe grant 101046231 (FantastiCOF) and M-ERA.NET 2021 (SuperSuper, FWO G0K9822N).

Notes and references

1 J. Anastassopoulou and T. Theophanides, *Bioinorg. Chem.*, 1995, 209–218.
2 J. A. Cotruvo, *ACS Cent. Sci.*, 2019, **5**, 1496–1506.
3 G. Rando, S. Sfameni and M. R. Plutino, *Gels*, 2022, **9**, 9.
4 D. Pathania, A. K. Srivastava and A. Sharma, *Curr. Res. Green Sustainable Chem.*, 2021, **4**, 100073.
5 J. Wang, T. Feng, J. Chen, V. Ramalingam, Z. Li, D. M. Kabtamu, J. H. He and X. Fang, *Nano Energy*, 2021, **86**, 106088.

6 S. R. Batten, N. R. Champness, X.-M. Chen, J. Garcia-Martinez, S. Kitagawa, L. Öhrström, M. O'Keeffe, M. Paik Suh and J. Reedijk, *Pure Appl. Chem.*, 2013, **85**, 1715–1724.
7 E. Miguel-Casañ, G. R. F. Orton, D. E. Schier and N. R. Champness, *Adv. Mater.*, 2025, 2414509.
8 S. L. Griffin and N. R. Champness, *Coord. Chem. Rev.*, 2020, **414**, 213295.
9 H. Furukawa, K. E. Cordova, M. O'Keeffe and O. M. Yaghi, *Science*, 2013, **341**, 1230444.
10 S. Kitagawa and R. Matsuda, *Coord. Chem. Rev.*, 2007, **251**, 2490–2509.
11 S. Kitagawa, R. Kitaura and S. Noro, *Angew. Chem., Int. Ed.*, 2004, **43**, 2334–2375.
12 O. M. Yaghi, H. Li, C. Davis, D. Richardson and T. L. Groy, *Acc. Chem. Res.*, 1998, **31**, 474–484.
13 S. Kitagawa and M. Kondo, *Bull. Chem. Soc. Jpn.*, 1998, **71**, 1739–1753.
14 R. Freund, S. Canossa, S. M. Cohen, W. Yan, H. Deng, V. Guillerm, M. Eddaoudi, D. G. Madden, D. Fairen-Jimenez, H. Lyu, L. K. Macreadie, Z. Ji, Y. Zhang, B. Wang, F. Haase, C. Wöll, O. Zaremba, J. Andreo, S. Wuttke and C. S. Diercks, *Angew. Chem., Int. Ed.*, 2021, **60**, 23946–23974.
15 M. S. Lohse and T. Bein, *Adv. Funct. Mater.*, 2018, **28**, 1705553.
16 R. B. Lin, Y. He, P. Li, H. Wang, W. Zhou and B. Chen, *Chem. Soc. Rev.*, 2019, **48**, 1362–1389.
17 L. H. Chen, M. H. Sun, Z. Wang, W. Yang, Z. Xie and B. L. Su, *Chem. Rev.*, 2020, **120**, 11194–11294.
18 M. Eddaoudi, D. B. Moler, H. Li, B. Chen, T. M. Reineke, M. O'Keeffe and O. M. Yaghi, *Acc. Chem. Res.*, 2001, **34**, 319–330.
19 J. Ha, J. H. Lee and H. R. Moon, *Inorg. Chem. Front.*, 2020, **7**, 12–27.
20 F. M. Amombo Noa, M. Abrahamsson, E. Ahlberg, O. Cheung, C. R. Göb, C. J. McKenzie and L. Öhrström, *Chem*, 2021, **7**, 2491–2512.
21 Y. Luo, M. Ahmad, A. Schug and M. Tsotsalas, *Adv. Mater.*, 2019, **31**, 1901744.
22 G. Chakraborty, I.-H. Park, R. Medishetty and J. J. Vittal, *Chem. Rev.*, 2021, **121**, 3751–3891.
23 P. Payamyar, B. T. King, H. C. Öttinger and A. D. Schlüter, *Chem. Commun.*, 2016, **52**, 18–34.
24 O. Shekhah, J. Liu, R. A. Fischer and C. Wöll, *Chem. Soc. Rev.*, 2011, **40**, 1081–1106.
25 C. Simms, A. Mullaliu, S. Swinnen, F. de Azambuja and T. N. Parac-Vogt, *Mol. Syst. Des. Eng.*, 2023, **8**, 270–288.
26 R. Freund, O. Zaremba, G. Arnauts, R. Ameloot, G. Skorupskii, M. Dincă, A. Bavykina, J. Gascon, A. Ejsmont, J. Goscianska, M. Kalmutzki, U. Lächelt, E. Ploetz, C. S. Diercks and S. Wuttke, *Angew. Chem., Int. Ed.*, 2021, **60**, 23975–24001.
27 H. G. T. Ly, G. Fu, A. Kondinski, B. Bueken, D. De Vos and T. N. Parac-Vogt, *J. Am. Chem. Soc.*, 2018, **140**, 6325–6335.
28 P. Wu, Y. Li, J. J. Zheng, N. Hosono, K. ichi Otake, J. Wang, Y. Liu, L. Xia, M. Jiang, S. Sakaki and S. Kitagawa, *Nat. Commun.*, 2019, **10**, 1–8.
29 L. J. Murray, M. Dincă and J. R. Long, *Chem. Soc. Rev.*, 2009, **38**, 1294.
30 Y. Gu, J. Zheng, K. Otake, M. Shivanna, S. Sakaki, H. Yoshino, M. Ohba, S. Kawaguchi, Y. Wang, F. Li and S. Kitagawa, *Angew. Chem., Int. Ed.*, 2021, **60**, 11688–11694.
31 J. Navarro-Sánchez, A. I. Argente-García, Y. Moliner-Martínez, D. Roca-Sanjuán, D. Antypov, P. Campíns-Falcó, M. J. Rosseinsky and C. Martí-Gastaldo, *J. Am. Chem. Soc.*, 2017, **139**, 4294–4297.
32 V. Rubio-Giménez, S. Tatay and C. Martí-Gastaldo, *Chem. Soc. Rev.*, 2020, **49**, 5601–5638.
33 D. Sheberla, J. C. Bachman, J. S. Elias, C. J. Sun, Y. Shao-Horn and M. Dinca, *Nat. Mater.*, 2017, **16**, 220–224.
34 L. Sun, M. G. Campbell and M. Dincă, *Angew. Chem., Int. Ed.*, 2016, **55**, 3566–3579.
35 Y.-H. Xiao, Z.-G. Gu and J. Zhang, *Nanoscale*, 2020, **12**, 12712–12730.
36 G. Genesio, J. Maynadié, M. Carboni and D. Meyer, *New J. Chem.*, 2018, **42**, 2351–2363.
37 P. De Luna, W. Liang, A. Mallick, O. Shekhah, F. P. García De Arquer, A. H. Proppe, P. Todorović, S. O. Kelley, E. H. Sargent and M. Eddaoudi, *ACS Appl. Mater. Interfaces*, 2018, **10**, 31225–31232.
38 L. Dong, Z. A. Gao and N. Lin, *Prog. Surf. Sci.*, 2016, **91**, 101–135.
39 A. Dmitriev, H. Spillmann, N. Lin, J. V. Barth and K. Kern, *Angew. Chem., Int. Ed.*, 2003, **42**, 2670–2673.
40 X. B. Wang, B. Xia, C. K. Lyu, D. Kim, E. Li, S. Q. Fu, J. Y. Chen, P. N. Liu, F. Liu and N. Lin, *Commun. Chem.*, 2023, **6**, 73.
41 C. Lyu, Y. Gao, Z. Gao, S. Mo, M. Hua, E. Li, S. Fu, J. Chen, P. Liu, L. Huang and N. Lin, *Angew. Chem., Int. Ed.*, 2022, **134**, 1–5.
42 W. Pang, B. Shao, X. Q. Tan, C. Tang, Z. Zhang and J. Huang, *Nanoscale*, 2020, **12**, 3623–3629.
43 R. Dong, M. Pfeffermann, H. Liang, Z. Zheng, X. Zhu, J. Zhang and X. Feng, *Angew. Chem., Int. Ed.*, 2015, **54**, 12058–12063.
44 S. Stepanow, M. Lingenfelder, A. Dmitriev, H. Spillmann, E. Delvigne, N. Lin, X. Deng, C. Cai, J. V. Barth and K. Kern, *Nat. Mater.*, 2004, **3**, 229–233.
45 K. E. Plass, A. L. Grzesiak and A. J. Matzger, *Acc. Chem. Res.*, 2007, **40**, 287–293.
46 R. Chakrabarty, P. S. Mukherjee and P. J. Stang, *Chem. Rev.*, 2011, **111**, 6810–6918.
47 H. Wang, Y. Li, N. Li, A. Filosa and X. Li, *Nat. Rev. Mater.*, 2020, **6**, 145–167.
48 B. S. Pilgrim and N. R. Champness, *ChemPlusChem*, 2020, **85**, 1842–1856.
49 T. R. Cook, Y.-R. Zheng and P. J. Stang, *Chem. Rev.*, 2013, **113**, 734–777.
50 C. Gropp, S. Canossa, S. Wuttke, F. Gándara, Q. Li, L. Gagliardi and O. M. Yaghi, *ACS Cent. Sci.*, 2020, **6**, 1255–1273.
51 E. Ploetz, H. Engelke, U. Lächelt and S. Wuttke, *Adv. Funct. Mater.*, 2020, **30**, 1909062.

52 M. M. Modena, B. Rühle, T. P. Burg and S. Wuttke, *Adv. Mater.*, 2019, **31**, 1–26.
53 D. Y. Kang, J. S. Lee and L. C. Lin, *Langmuir*, 2022, **38**, 9441–9453.
54 M. A. Soldatov, A. Martini, A. L. Bugaev, I. Pankin, P. V. Medvedev, A. A. Guda, A. M. Aboraia, Y. S. Podkovyrina, A. P. Budnyk, A. A. Soldatov and C. Lamberti, *Polyhedron*, 2018, **155**, 232–253.
55 S. Øien-ØDegaard, G. C. Shearer, D. S. Wragg and K. P. Lillerud, *Chem. Soc. Rev.*, 2017, **46**, 4867–4876.
56 X. Gong, K. Gnanasekaran, Z. Chen, L. Robison, M. C. Wasson, K. C. Bentz, S. M. Cohen, O. K. Farha and N. C. Gianneschi, *J. Am. Chem. Soc.*, 2020, **142**, 17224–17235.
57 Y. Zhou, X. Xu, A. Carlsson, S. Lazar, Z. Pan, Y. Ma, O. Terasaki and H. Deng, *Chem. Mater.*, 2020, **32**, 4966–4972.
58 X. Gong, H. Noh, N. C. Gianneschi and O. K. Farha, *J. Am. Chem. Soc.*, 2019, **141**, 6146–6151.
59 S. Pu, C. Gong and A. W. Robertson, *R. Soc. Open Sci.*, 2020, **7**, 191204.
60 J. W. M. Osterrieth, J. Rampersad, D. Madden, N. Rampal, L. Skoric, B. Connolly, M. D. Allendorf, V. Stavila, J. L. Snider, R. Ameloot, J. Marreiros, C. Ania, D. Azevedo, E. Vilarrasa-Garcia, B. F. Santos, X. Bu, Z. Chang, H. Bunzen, N. R. Champness, S. L. Griffin, B. Chen, R. Lin, B. Coasne, S. Cohen, J. C. Moreton, Y. J. Colón, L. Chen, R. Clowes, F. Coudert, Y. Cui, B. Hou, D. M. D'Alessandro, P. W. Doheny, M. Dincă, C. Sun, C. Doonan, M. T. Huxley, J. D. Evans, P. Falcaro, R. Ricco, O. Farha, K. B. Idrees, T. Islamoglu, P. Feng, H. Yang, R. S. Forgan, D. Bara, S. Furukawa, E. Sanchez, J. Gascon, S. Telalović, S. K. Ghosh, S. Mukherjee, M. R. Hill, M. M. Sadiq, P. Horcajada, P. Salcedo-Abraira, K. Kaneko, R. Kukobat, J. Kenvin, S. Keskin, S. Kitagawa, K. Otake, R. P. Lively, S. J. A. DeWitt, P. Llewellyn, B. V. Lotsch, S. T. Emmerling, A. M. Pütz, C. Martí-Gastaldo, N. M. Padial, J. García-Martínez, N. Linares, D. Maspoch, J. A. Suárez del Pino, P. Moghadam, R. Oktavian, R. E. Morris, P. S. Wheatley, J. Navarro, C. Petit, D. Danaci, M. J. Rosseinsky, A. P. Katsoulidis, M. Schröder, X. Han, S. Yang, C. Serre, G. Mouchaham, D. S. Sholl, R. Thyagarajan, D. Siderius, R. Q. Snurr, R. B. Goncalves, S. Telfer, S. J. Lee, V. P. Ting, J. L. Rowlandson, T. Uemura, T. Iiyuka, M. A. van der Veen, D. Rega, V. Van Speybroeck, S. M. J. Rogge, A. Lamaire, K. S. Walton, L. W. Bingel, S. Wuttke, J. Andreo, O. Yaghi, B. Zhang, C. T. Yavuz, T. S. Nguyen, F. Zamora, C. Montoro, H. Zhou, A. Kirchon and D. Fairen-Jimenez, *Adv. Mater.*, 2022, **34**, 2201502.
61 S. Krause, N. Hosono and S. Kitagawa, *Angew. Chem., Int. Ed.*, 2020, **59**, 15325–15341.
62 S. Horike, S. Shimomura and S. Kitagawa, *Nat. Chem.*, 2009, **1**, 695–704.
63 A. J. McConnell, *Chem. Soc. Rev.*, 2022, **51**, 2957–2971.
64 K. Bian, C. Gerber, A. J. Heinrich, D. J. Müller, S. Scheuring and Y. Jiang, *Nat. Rev. Methods Primers*, 2021, **1**, 36.
65 D. Wang, T. Haposan, J. Fan, A. Arramel and A. T. S. Wee, *ACS Nano*, 2024, **18**, 30919–30942.
66 G. Zhan, Z. F. Cai, K. Strutyński, L. Yu, N. Herrmann, M. Martínez-Abadía, M. Melle-Franco, A. Mateo-Alonso and S. De Feyter, *Nature*, 2022, **603**, 835–840.
67 K. S. Mali, J. Adisoejoso, E. Ghijsens, I. De Cat and S. De Feyter, *Acc. Chem. Res.*, 2012, **45**, 1309–1320.
68 M. Trueman, R. J. S. Pooley, A. R. B. J. Lutton-Gething, A. Hasija, G. F. S. Whitehead, S. J. O'Shea, M. W. Anderson and M. P. Attfield, *J. Am. Chem. Soc.*, 2025, **147**, 17201–17208.
69 N. Hosono, A. Terashima, S. Kusaka, R. Matsuda and S. Kitagawa, *Nat. Chem.*, 2019, **11**, 109–116.
70 T. Ando, T. Uchihashi and S. Scheuring, *Chem. Rev.*, 2014, **114**, 3120–3188.
71 P. Messina, A. Dmitriev, N. Lin, H. Spillmann, M. Abel, J. V. Barth and K. Kern, *J. Am. Chem. Soc.*, 2002, **124**, 14000–14001.
72 N. Lin, A. Dmitriev, J. Weckesser, J. V. Barth and K. Kern, *Angew. Chem., Int. Ed.*, 2002, **41**, 4779–4783.
73 M. A. Lingenfelder, H. Spillmann, A. Dmitriev, S. Stepanow, N. Lin, J. V. Barth and K. Kern, *Chem. – Eur. J.*, 2004, **10**, 1913–1919.
74 A. Dmitriev, H. Spillmann, M. Lingenfelder, N. Lin, J. V. Barth and K. Kern, *Langmuir*, 2004, **20**, 4799–4801.
75 D. Kühne, F. Klappenberger, R. Decker, U. Schlickum, H. Brune, S. Klyatskaya, M. Ruben and J. V. Barth, *J. Am. Chem. Soc.*, 2009, **131**, 3881–3883.
76 C. Safarowsky, L. Merz, A. Rang, P. Broekmann, B. A. Hermann and C. A. Schalley, *Angew. Chem., Int. Ed.*, 2004, **43**, 1291–1294.
77 K. S. Jeong, S. Y. Kim, U.-S. Shin, M. Kogej, N. T. M. Hai, P. Broekmann, N. Jeong, B. Kirchner, M. Reiher and C. A. Schalley, *J. Am. Chem. Soc.*, 2005, **127**, 17672–17685.
78 Q.-H. Yuan, L.-J. Wan, H. Jude and P. J. Stang, *J. Am. Chem. Soc.*, 2005, **127**, 16279–16286.
79 M. El Garah, A. Ciesielski, N. Marets, V. Bulach, M. W. Hosseini and P. Samorì, *Chem. Commun.*, 2014, **50**, 12250–12253.
80 A. Cucinotta, C. Kahlfuss, A. Minoia, S. Eyley, K. Zwaenepoel, G. Velpula, W. Thielemans, R. Lazzaroni, V. Bulach, M. W. Hosseini, K. S. Mali and S. De Feyter, *J. Am. Chem. Soc.*, 2023, **145**, 1194–1205.
81 A. Cucinotta, S. Eyley, J. A. Davies, W. Thielemans, K. S. Mali and S. De Feyter, *J. Am. Chem. Soc.*, 2025, **147**, 7682–7693.
82 M. Shöâeè, J. R. Agger, M. W. Anderson and M. P. Attfield, *CrystEngComm*, 2008, **10**, 646–648.
83 M. Shoaee, M. W. Anderson and M. P. Attfield, *Angew. Chem., Int. Ed.*, 2008, **47**, 8525–8528.
84 C. Munuera, O. Shekhah, H. Wang, C. Wöll and C. Ocal, *Phys. Chem. Chem. Phys.*, 2008, **10**, 7257–7261.
85 G. Delen, Z. Ristanović, L. D. B. Mandemaker and B. M. Weckhuysen, *Chem. – Eur. J.*, 2018, **24**, 187–195.
86 G. Binnig, H. Rohrer, C. Gerber and E. Weibel, *Appl. Phys. Lett.*, 1982, **40**, 178–180.

87 G. Binnig and H. Rohrer, *Rev. Mod. Phys.*, 1987, **59**, 615–625.
88 E. Meyer, R. Bennewitz and H. J. Hug, *Scanning Probe Microscopy*, Springer, Cham, 2021.
89 B. Voigtländer, *Non-Destructive Material Characterization Methods*, Springer, 2015.
90 J. Atkins and P. W. de Paula, *Atkins' Physical Chemistry*, Oxford University Press, 9th edn, 2010.
91 H. J. W. Zandvliet and A. van Houselt, *Annu. Rev. Anal. Chem.*, 2009, **2**, 37–55.
92 W. Mamdouh, H. Uji-I, J. S. Ladislaw, A. E. Dulcey, V. Percec, F. C. De Schryver and S. De Feyter, *J. Am. Chem. Soc.*, 2006, **128**, 317–325.
93 K. S. Mali, N. Pearce, S. De Feyter and N. R. Champness, *Chem. Soc. Rev.*, 2017, **46**, 2520–2542.
94 G. Binnig, C. F. Quate and C. Gerber, *Phys. Rev. Lett.*, 1986, **56**, 930–933.
95 J. J. Schwartz, D. S. Jakob and A. Centrone, *Chem. Soc. Rev.*, 2022, **51**, 5248–5267.
96 A. Dazzi and C. B. Prater, *Chem. Rev.*, 2017, **117**, 5146–5173.
97 Q. Xie and X. G. Xu, *Langmuir*, 2023, **39**, 17593–17599.
98 V. Rose, K. Wang, T. Chien, J. Hiller, D. Rosenmann, J. W. Freeland, C. Preissner and S. Hla, *Adv. Funct. Mater.*, 2013, **23**, 2646–2652.
99 L. Sosa-Vargas, E. Kim and A.-J. Attias, *Mater. Horiz.*, 2017, **4**, 570–583.
100 X. Zhao and X. Miao, *iScience*, 2024, **27**, 109392.
101 Y. Wang, X. Li, Q. Yang, Q. Shen, Y. He, Y. Zhang and Y. Wang, *Fundam. Res.*, 2025, **5**, 1524–1537.
102 J. Liu and N. Lin, *ChemPlusChem*, 2023, **88**, e202200359.
103 H. Liang, Y. He, Y. Ye, X. Xu, F. Cheng, W. Sun, X. Shao, Y. Wang, J. Li and K. Wu, *Coord. Chem. Rev.*, 2009, **253**, 2959–2979.
104 S. O. Parreiras, J. M. Gallego and D. Écija, *Chem. Commun.*, 2023, **59**, 8878–8893.
105 D. Écija, J. I. Urgel, A. P. Seitsonen, W. Auwärter and J. V. Barth, *Acc. Chem. Res.*, 2018, **51**, 365–375.
106 A. Ciesielski, C. Palma, M. Bonini and P. Samorì, *Adv. Mater.*, 2010, **22**, 3506–3520.
107 D. P. Goronzy, M. Ebrahimi, F. Rosei, A. Arramel, Y. Fang, S. De Feyter, S. L. Tait, C. Wang, P. H. Beton, A. T. S. Wee, P. S. Weiss and D. F. Perepichka, *ACS Nano*, 2018, **12**, 7445–7481.
108 K. G. Nath, O. Ivasenko, J. M. MacLeod, J. A. Miwa, J. D. Wuest, A. Nanci, D. F. Perepichka and F. Rosei, *J. Phys. Chem. C*, 2007, **111**, 16996–17007.
109 U. Mazur and K. W. Hipps, *Chem. Commun.*, 2015, **51**, 4737–4749.
110 R. Gutzler, L. Cardenas and F. Rosei, *Chem. Sci.*, 2011, **2**, 2290–2300.
111 O. Ochs, M. Hocke, S. Spitzer, W. M. Heckl, N. Martsinovich and M. Lackinger, *Chem. Mater.*, 2020, **32**, 5057–5065.
112 I. Destoop, A. Minoia, O. Ivasenko, A. Noguchi, K. Tahara, Y. Tobe, R. Lazzaroni and S. De Feyter, *Faraday Discuss.*, 2017, **204**, 215–231.
113 M. Lackinger, S. Griessl, W. M. Heckl, M. Hietschold and G. W. Flynn, *Langmuir*, 2005, **21**, 4984–4988.
114 S. Stepanow, N. Lin, J. V. Barth and K. Kern, *J. Phys. Chem. B*, 2006, **110**, 23472–23477.
115 Z. Shi and N. Lin, *J. Am. Chem. Soc.*, 2009, **131**, 5376–5377.
116 S. Vijayaraghavan, D. Ecija, W. Auwärter, S. Joshi, K. Seufert, M. Drach, D. Nieckarz, P. Szabelski, C. Aurisicchio, D. Bonifazi and J. V. Barth, *Chem. – Eur. J.*, 2013, **19**, 14143–14150.
117 J. I. Urgel, D. Ecija, W. Auwärter, D. Stassen, D. Bonifazi and J. V. Barth, *Angew. Chem., Int. Ed.*, 2015, **54**, 6163–6167.
118 J. F. Schultz, B. Yang and N. Jiang, *J. Chem. Phys.*, 2021, **154**, 1–10.
119 S. Kowarik, A. Gerlach and F. Schreiber, *J. Phys.: Condens. Matter*, 2008, **20**, 184005.
120 A. Dmitriev, N. Lin, J. Weckesser, J. V. Barth and K. Kern, *J. Phys. Chem. B*, 2002, **106**, 6907–6912.
121 T. Classen, M. Lingenfelder, Y. Wang, R. Chopra, C. Virojanadara, U. Starke, G. Costantini, G. Fratesi, S. Fabris, S. de Gironcoli, S. Baroni, S. Haq, R. Raval and K. Kern, *J. Phys. Chem. A*, 2007, **111**, 12589–12603.
122 U. Schlickum, R. Decker, F. Klappenberger, G. Zoppellaro, S. Klyatskaya, M. Ruben, I. Silanes, A. Arnau, K. Kern, H. Brune and J. V. Barth, *Nano Lett.*, 2007, **7**, 3813–3817.
123 F. Bischoff, Y. He, K. Seufert, D. Stassen, D. Bonifazi, J. V. Barth and W. Auwärter, *Chem. – Eur. J.*, 2016, **22**, 15298–15306.
124 N. Lin, S. Stepanow, F. Vidal, J. V. Barth and K. Kern, *Chem. Commun.*, 2005, 1681–1683.
125 U. Schlickum, F. Klappenberger, R. Decker, G. Zoppellaro, S. Klyatskaya, M. Ruben, K. Kern, H. Brune and J. V. Barth, *J. Phys. Chem. C*, 2010, **114**, 15602–15606.
126 Z. Shi and N. Lin, *J. Am. Chem. Soc.*, 2010, **132**, 10756–10761.
127 X. F. Mao, T. Lin, J. Adisoejoso, Z. Shi, X. S. Shang, P. N. Liu and N. Lin, *Phys. Chem. Chem. Phys.*, 2013, **15**, 12447.
128 D.-D. Zhou, J. Wang, P. Chen, Y. He, J.-X. Wu, S. Gao, Z. Zhong, Y. Du, D. Zhong and J.-P. Zhang, *Chem. Sci.*, 2021, **12**, 1272–1277.
129 D. Moreno, S. O. Parreiras, S. K. Mathialagan, M. Tenorio, K. Lauwaet, J. I. Urgel, J. M. Gallego and D. Écija, *Chem. – Eur. J.*, 2025, **31**, 2–7.
130 L.-X. Kang, B.-X. Wang, X.-Y. Zhang, Y.-C. Zhu, D.-Y. Li and P.-N. Liu, *J. Phys. Chem. Lett.*, 2024, **15**, 6108–6114.
131 R. Adhikari, J. Kuliga, M. Ruppel, N. Jux, H. Marbach and H.-P. Steinrück, *J. Phys. Chem. C*, 2021, **125**, 7204–7212.
132 D. Kumar, J. Hellerstedt, B. Field, B. Lowe, Y. Yin, N. V. Medhekar and A. Schiffrin, *Adv. Funct. Mater.*, 2021, **31**, 1–9.
133 S. O. Parreiras, D. Moreno, B. Cirera, M. A. Valbuena, J. I. Urgel, M. Paradinas, M. Panighel, F. Ajejas, M. A. Niño, J. M. Gallego, M. Valvidares, P. Gargiani, W. Kuch, J. I. Martínez, A. Mugarza, J. Camarero, R. Miranda, P. Perna and D. Écija, *Small*, 2021, **17**, e2102753.
134 J. I. Urgel, B. Cirera, Y. Wang, W. Auwärter, R. Otero, J. M. Gallego, M. Alcamí, S. Klyatskaya, M. Ruben,

F. Martín, R. Miranda, D. Ecija and J. V. Barth, *Small*, 2015, **11**, 6358–6364.
135 D. Écija, J. I. Urgel, A. C. Papageorgiou, S. Joshi, W. Auwärter, A. P. Seitsonen, S. Klyatskaya, M. Ruben, S. Fischer, S. Vijayaraghavan, J. Reichert and J. V. Barth, *Proc. Natl. Acad. Sci. U. S. A.*, 2013, **110**, 6678–6681.
136 E. Rheinfrank, M. Pörtner, M. del C. Nuñez Beyerle, F. Haag, P. S. Deimel, F. Allegretti, K. Seufert, J. V. Barth, M. L. Bocquet, P. Feulner and W. Auwärter, *J. Am. Chem. Soc.*, 2021, **143**, 14581–14591.
137 J. I. Urgel, D. Écija, G. Lyu, R. Zhang, C.-A. Palma, W. Auwärter, N. Lin and J. V. Barth, *Nat. Chem.*, 2016, **8**, 657–662.
138 S. M. Barlow and R. Raval, *Surf. Sci. Rep.*, 2003, **50**, 201–341.
139 J. A. A. W. Elemans, I. De Cat, H. Xu and S. De Feyter, *Chem. Soc. Rev.*, 2009, **38**, 722–736.
140 F. Vidal, E. Delvigne, S. Stepanow, N. Lin, J. V. Barth and K. Kern, *J. Am. Chem. Soc.*, 2005, **127**, 10101–10106.
141 T. G. Gopakumar, F. Matino, B. Schwager, A. Bannwarth, F. Tuczek and R. Berndt, *J. Phys. Chem. C*, 2010, **114**, 18247–18251.
142 I. Destoop, E. Ghijsens, K. Katayama, K. Tahara, K. S. Mali, Y. Tobe and S. De Feyter, *J. Am. Chem. Soc.*, 2012, **134**, 19568–19571.
143 M. Schöck, R. Otero, S. Stojkovic, F. Hümmelink, A. Gourdon, E. Lægsgaard, I. Stensgaard, C. Joachim and F. Besenbacher, *J. Phys. Chem. B*, 2006, **110**, 12835–12838.
144 J. Seibel, L. Verstraete, B. E. Hirsch, A. M. Bragança and S. De Feyter, *J. Am. Chem. Soc.*, 2018, **140**, 11565–11568.
145 H. Spillmann, A. Dmitriev, N. Lin, P. Messina, J. V. Barth and K. Kern, *J. Am. Chem. Soc.*, 2003, **125**, 10725–10728.
146 B. Yang, N. Cao, H. Ju, H. Lin, Y. Li, H. Ding, J. Ding, J. Zhang, C. Peng, H. Zhang, J. Zhu, Q. Li and L. Chi, *J. Am. Chem. Soc.*, 2019, **141**, 168–174.
147 J. Liu, T. Lin, Z. Shi, F. Xia, L. Dong, P. N. Liu and N. Lin, *J. Am. Chem. Soc.*, 2011, **133**, 18760–18766.
148 M. Lischka, R. Dong, M. Wang, N. Martsinovich, M. Fritton, L. Grossmann, W. M. Heckl, X. Feng and M. Lackinger, *Chem. – Eur. J.*, 2019, **25**, 1975–1983.
149 Z. Gao, C.-H. Hsu, J. Liu, F.-C. Chuang, R. Zhang, B. Xia, H. Xu, L. Huang, Q. Jin, P. N. Liu and N. Lin, *Nanoscale*, 2019, **11**, 878–881.
150 F. Gu, S. Shu, C. E. Patrick and M. R. Castell, *J. Phys. Chem. C*, 2024, **128**, 17797–17805.
151 H. Walch, J. Dienstmaier, G. Eder, R. Gutzler, S. Schlögl, T. Sirtl, K. Das, M. Schmittel and M. Lackinger, *J. Am. Chem. Soc.*, 2011, **133**, 7909–7915.
152 C. Lyu, Y. Gao, K. Zhou, M. Hua, Z. Shi, P.-N. Liu, L. Huang and N. Lin, *ACS Nano*, 2024, **18**, 19793–19801.
153 Z. Shi, J. Liu, T. Lin, F. Xia, P. N. Liu and N. Lin, *J. Am. Chem. Soc.*, 2011, **133**, 6150–6153.
154 S. Stepanow, N. Lin, D. Payer, U. Schlickum, F. Klappenberger, G. Zoppellaro, M. Ruben, H. Brune, J. V. Barth and K. Kern, *Angew. Chem., Int. Ed.*, 2007, **46**, 710–713.
155 S. L. Tait, A. Langner, N. Lin, R. Chandrasekar, O. Fuhr, M. Ruben and K. Kern, *ChemPhysChem*, 2008, **9**, 2495–2499.
156 C. S. Kley, J. Čechal, T. Kumagai, F. Schramm, M. Ruben, S. Stepanow and K. Kern, *J. Am. Chem. Soc.*, 2012, **134**, 6072–6075.
157 H. Grove, J. Sletten, M. Julve and F. Lloret, *J. Chem. Soc., Dalton Trans.*, 2001, 1029–1034.
158 A. Gutierrez, M. Buchet and S. Clair, *ChemPhysChem*, 2019, **20**, 2286–2291.
159 J. Lu, D. Nieckarz, H. Jiang, Z. Zhu, Y. Yan, F. Zheng, W. Rżysko, J. Lisiecki, P. Szabelski and Q. Sun, *ACS Nano*, 2023, **17**, 20194–20202.
160 S. L. Tait, Y. Wang, G. Costantini, N. Lin, A. Baraldi, F. Esch, L. Petaccia, S. Lizzit and K. Kern, *J. Am. Chem. Soc.*, 2008, **130**, 2108–2113.
161 P. Gambardella, S. Stepanow, A. Dmitriev, J. Honolka, F. M. F. De Groot, M. Lingenfelder, S. Sen Gupta, D. D. Sarma, P. Bencok, S. Stanescu, S. Clair, S. Pons, N. Lin, A. P. Seitsonen, H. Brune, J. V. Barth and K. Kern, *Nat. Mater.*, 2009, **8**, 189–193.
162 K. M. L. Taylor-Pashow, J. Della Rocca, Z. Xie, S. Tran and W. Lin, *J. Am. Chem. Soc.*, 2009, **131**, 14261–14263.
163 C. Martín-Fuentes, S. O. Parreiras, J. I. Urgel, V. Rubio-Giménez, B. Muñiz Cano, D. Moreno, K. Lauwaet, M. Valvidares, M. A. Valbuena, P. Gargiani, W. Kuch, J. Camarero, J. M. Gallego, R. Miranda, J. I. Martínez, C. Martí-Gastaldo and D. Écija, *J. Am. Chem. Soc.*, 2022, **144**, 16034–16041.
164 M. Hmadeh, Z. Lu, Z. Liu, F. Gándara, H. Furukawa, S. Wan, V. Augustyn, R. Chang, L. Liao, F. Zhou, E. Perre, V. Ozolins, K. Suenaga, X. Duan, B. Dunn, Y. Yamamto, O. Terasaki and O. M. Yaghi, *Chem. Mater.*, 2012, **24**, 3511–3513.
165 A. Mahringer, A. C. Jakowetz, J. M. Rotter, B. J. Bohn, J. K. Stolarczyk, J. Feldmann, T. Bein and D. D. Medina, *ACS Nano*, 2019, **13**, 6711–6719.
166 V. Baltz, A. Manchon, M. Tsoi, T. Moriyama, T. Ono and Y. Tserkovnyak, *Rev. Mod. Phys.*, 2018, **90**, 15005.
167 F. Frezza, M. Kumar, A. Sánchez-Grande, D. Soler-Polo, M. Carrera, O. Stetsovych, P. Mutombo, D. Curiel and P. Jelínek, *J. Am. Chem. Soc.*, 2025, **147**, 19575–19582.
168 A. Kumar, K. Banerjee, A. S. Foster and P. Liljeroth, *Nano Lett.*, 2018, **18**, 5596–5602.
169 S. Yoshimoto, Y. Ono, K. Nishiyama and I. Taniguchi, *Phys. Chem. Chem. Phys.*, 2010, **12**, 14442–14444.
170 S. Li, C. Gong, Y. Zhang, S. Fu, Z. Wang, Y. Lu, S. Gu, X. Liu and L. Wang, *RSC Adv.*, 2022, **12**, 3892–3896.
171 D. J. Díaz, G. D. Storrier, S. Bernhard, K. Takada and H. D. Abruña, *Langmuir*, 1999, **15**, 7351–7354.
172 H. M. Zhang, W. Zhao, Z. X. Xie, L. S. Long, B. W. Mao, X. Xu and L. S. Zheng, *J. Phys. Chem. C*, 2007, **111**, 7570–7573.
173 Y. Kikkawa, E. Koyama, S. Tsuzuki, K. Fujiwara, K. Miyake, H. Tokuhisa and M. Kanesato, *Surf. Sci.*, 2007, **601**, 2520–2524.

174 M. Surin, P. Samorì, A. Jouaiti, N. Kyritsakas and M. W. Hosseini, *Angew. Chem., Int. Ed.*, 2007, **46**, 245–249.
175 M. A. Carvalho, H. Dekkiche, M. Nagasaki, Y. Kikkawa and R. Ruppert, *J. Am. Chem. Soc.*, 2019, **141**, 10137–10141.
176 Y. Kikkawa, M. Nagasaki, S. Tsuzuki, T. N. J. Fouquet, S. Nakamura, Y. Takenaka, Y. Norikane and K. Hiratani, *Chem. Commun.*, 2022, **58**, 1752–1755.
177 M. El Garah, N. Marets, M. Mauro, A. Aliprandi, S. Bonacchi, L. De Cola, A. Ciesielski, V. Bulach, M. W. Hosseini and P. Samorì, *J. Am. Chem. Soc.*, 2015, **137**, 8450–8459.
178 V. Mishra, S. H. Mir, J. K. Singh and T. G. Gopakumar, *ACS Appl. Mater. Interfaces*, 2020, **12**, 51122–51132.
179 J. Liu, M. Paradinas, L. Heinke, M. Buck, C. Ocal, V. Mugnaini and C. Wöll, *ChemElectroChem*, 2016, **3**, 713–718.
180 S. Goswami, M. Rimoldi, R. Anderson, C. Lee, X. Li, A. Li, P. Deria, L. X. Chen, R. D. Schaller, D. A. Gómez-Gualdrón, O. K. Farha and J. T. Hupp, *Chem. Mater.*, 2022, **34**, 9446–9454.
181 A. J. Brandt, D. M. Shakya, K. Metavarayuth, E. Dolgopolova, L. Hensley, A. S. Duke, S. Farzandh, M. Stefik, N. B. Shustova and D. A. Chen, *Langmuir*, 2020, **36**, 9900–9908.
182 O. Lugier, U. Pokharel and S. Castellanos, *Cryst. Growth Des.*, 2020, **20**, 5302–5309.
183 L. G. S. Albano, T. P. Vello, D. H. S. de Camargo, R. M. L. da Silva, A. C. M. Padilha, A. Fazzio and C. C. B. Bufon, *Nano Lett.*, 2020, **20**, 1080–1088.
184 A. J. Cruz, I. Stassen, M. Krishtab, K. Marcoen, T. Stassin, S. Rodríguez-Hermida, J. Teyssandier, S. Pletincx, R. Verbeke, V. Rubio-Giménez, S. Tatay, C. Martí-Gastaldo, J. Meersschaut, P. M. Vereecken, S. De Feyter, T. Hauffman and R. Ameloot, *Chem. Mater.*, 2019, **31**, 9462–9471.
185 L. Pan, G. Liu, W. Shi, J. Shang, W. R. Leow, Y. Liu, Y. Jiang, S. Li, X. Chen and R.-W. Li, *Nat. Commun.*, 2018, **9**, 3813.
186 S. Rana, R. Rajendra, B. Dhara, P. K. Jha and N. Ballav, *Adv. Mater. Interfaces*, 2016, **3**, 1–8.
187 I. Christodoulou, T. Bourguignon, X. Li, G. Patriarche, C. Serre, C. Marlière and R. Gref, *Nanomaterials*, 2021, **11**, 722.
188 S. S. Y. Chui, S. M. F. Lo, J. P. H. Charmant, A. G. Orpen and I. D. Williams, *Science*, 1999, **283**, 1148–1150.
189 T. Wang, H. Zhu, Q. Zeng and D. Liu, *Adv. Mater. Interfaces*, 2019, **6**, 1–27.
190 K. Szelagowska-Kunstman, P. Cyganik, M. Goryl, D. Zacher, Z. Puterova, R. A. Fischer and M. Szymonski, *J. Am. Chem. Soc.*, 2008, **130**, 14446–14447.
191 C. Crivello, S. Sevim, O. Graniel, C. Franco, S. Pane, J. Puigmarti-Luis and D. Munoz-Rojas, *Mater. Horiz.*, 2021, **8**, 168–178.
192 Y. Zhang and C.-H. Chang, *Processes*, 2020, **8**, 377.
193 V. Chernikova, O. Shekhah and M. Eddaoudi, *ACS Appl. Mater. Interfaces*, 2016, **8**, 20459–20464.
194 P. Su, M. Tu, R. Ameloot and W. Li, *Acc. Chem. Res.*, 2022, **55**, 186–196.
195 R. Ameloot, F. Vermoortele, W. Vanhove, M. B. J. Roeffaers, B. F. Sels and D. E. De Vos, *Nat. Chem.*, 2011, **3**, 382–387.
196 V. Rubio-Giménez, S. Tatay, F. Volatron, F. J. Martínez-Casado, C. Martí-Gastaldo and E. Coronado, *J. Am. Chem. Soc.*, 2016, **138**, 2576–2584.
197 L. Heinke and C. Wöll, *Adv. Mater.*, 2019, **31**, 1806324.
198 J. Liu and C. Wöll, *Chem. Soc. Rev.*, 2017, **46**, 5730–5770.
199 T. Ladnorg, A. Welle, S. Heißler, C. Wöll and H. Gliemann, *Beilstein J. Nanotechnol.*, 2013, **4**, 638–648.
200 M. L. Ohnsorg, C. K. Beaudoin and M. E. Anderson, *Langmuir*, 2015, **31**, 6114–6121.
201 E. Biemmi, C. Scherb and T. Bein, *J. Am. Chem. Soc.*, 2007, **129**, 8054–8055.
202 R. P. Brand, L. D. B. Mandemaker, G. Delen, N. Rijnveld and B. M. Weckhuysen, *ChemPhysChem*, 2018, **19**, 2397–2404.
203 K. Sakata, S. Kashiyama, G. Matsuo, S. Uemura, N. Kimizuka and M. Kunitake, *ChemNanoMat*, 2015, **1**, 259–263.
204 G. Delen, M. Monai, F. Meirer and B. M. Weckhuysen, *Angew. Chem., Int. Ed.*, 2021, **60**, 1620–1624.
205 D. Shu, R. Fan, S. Yao, H. Jiang, X. Zhang and Y. Zheng, *J. Phys. Chem. C*, 2024, **128**, 12551–12557.
206 D. Sud and G. Kaur, *Polyhedron*, 2021, **193**, 114897.
207 N. Stock and S. Biswas, *Chem. Rev.*, 2012, **112**, 933–969.
208 N. S. John, C. Scherb, M. Shöâeè, M. W. Anderson, M. P. Attfield and T. Bein, *Chem. Commun.*, 2009, 6294–6296.
209 L. D. B. Mandemaker, M. Filez, G. Delen, H. Tan, X. Zhang, D. Lohse and B. M. Weckhuysen, *J. Phys. Chem. Lett.*, 2018, **9**, 1838–1844.
210 P. Y. Moh, P. Cubillas, M. W. Anderson and M. P. Attfield, *J. Am. Chem. Soc.*, 2011, **133**, 13304–13307.
211 P. Cubillas, M. W. Anderson and M. P. Attfield, *Chem. – Eur. J.*, 2012, **18**, 15406–15415.
212 P. Cubillas, K. Etherington, M. W. Anderson and M. P. Attfield, *CrystEngComm*, 2014, **16**, 9834–9841.
213 F. I. Pambudi, M. W. Anderson and M. P. Attfield, *Faraday Discuss.*, 2021, **231**, 112–126.
214 S. S. Li, B. H. Northrop, Q.-H. Yuan, L.-J. Wan and P. J. Stang, *Acc. Chem. Res.*, 2009, **42**, 249–259.
215 J.-R. Gong, L.-J. Wan, Q.-H. Yuan, C.-L. Bai, H. Jude and P. J. Stang, *Proc. Natl. Acad. Sci. U. S. A.*, 2005, **102**, 971–974.
216 T. Chen, G.-B. Pan, H. Wettach, M. Fritzsche, S. Höger, L.-J. Wan, H.-B. Yang, B. H. Northrop and P. J. Stang, *J. Am. Chem. Soc.*, 2010, **132**, 1328–1333.
217 S.-S. Li, H.-J. Yan, L.-J. Wan, H.-B. Yang, B. H. Northrop and P. J. Stang, *J. Am. Chem. Soc.*, 2007, **129**, 9268–9269.
218 Q.-H. Yuan, C.-J. Yan, H.-J. Yan, L.-J. Wan, B. H. Northrop, H. Jude and P. J. Stang, *J. Am. Chem. Soc.*, 2008, **130**, 8878–8879.
219 P. J. Stang, D. H. Cao, S. Saito and A. M. Arif, *J. Am. Chem. Soc.*, 1995, **117**, 6273–6283.
220 C. J. Kuehl, C. L. Mayne, A. M. Arif and P. J. Stang, *Org. Lett.*, 2000, **2**, 3727–3729.
221 C. J. Kuehl, Y. K. Kryschenko, U. Radhakrishnan, S. R. Seidel, S. D. Huang and P. J. Stang, *Proc. Natl. Acad. Sci. U. S. A.*, 2002, **99**, 4932–4936.
222 P. Su, B. Wei, C. Guo, Y. Hu, R. Tang, S. Zhang, C. He, J. Lin, X. Yu, Z. Chen, H. Li, H. Wang and X. Li, *J. Am. Chem. Soc.*, 2023, **145**, 3131–3145.

223 Y. Li, G.-F. Huo, B. Liu, B. Song, Y. Zhang, X. Qian, H. Wang, G.-Q. Yin, A. Filosa, W. Sun, S. W. Hla, H.-B. Yang and X. Li, *J. Am. Chem. Soc.*, 2020, **142**, 14638–14648.

224 F. Su, S. Zhang, Z. Chen, Z. Zhang, Z. Li, S. Lu, M. Zhang, F. Fang, S. Kang, C. Guo, C. Su, X. Yu, H. Wang and X. Li, *J. Am. Chem. Soc.*, 2022, **144**, 16559–16571.

225 J. Shi, Y. Li, X. Jiang, H. Yu, J. Li, H. Zhang, D. J. Trainer, S. W. Hla, H. Wang, M. Wang and X. Li, *J. Am. Chem. Soc.*, 2021, **143**, 1224–1234.

226 Z. Zhang, Y. Li, B. Song, Y. Zhang, X. Jiang, M. Wang, R. Tumbleson, C. Liu, P. Wang, X.-Q. Hao, T. Rojas, A. T. Ngo, J. L. Sessler, G. R. Newkome, S. W. Hla and X. Li, *Nat. Chem.*, 2020, **12**, 468–474.

227 L. Wang, B. Song, Y. Li, L. Gong, X. Jiang, M. Wang, S. Lu, X.-Q. Hao, Z. Xia, Y. Zhang, S. W. Hla and X. Li, *J. Am. Chem. Soc.*, 2020, **142**, 9809–9817.

228 Z. Li, Y. Li, Y. Zhao, H. Wang, Y. Zhang, B. Song, X. Li, S. Lu, X.-Q. Hao, S.-W. Hla, Y. Tu and X. Li, *J. Am. Chem. Soc.*, 2020, **142**, 6196–6205.

229 T. M. Ajayi, N. Shirato, T. Rojas, S. Wieghold, X. Cheng, K. Z. Latt, D. J. Trainer, N. K. Dandu, Y. Li, S. Premarathna, S. Sarkar, D. Rosenmann, Y. Liu, N. Kyritsakas, S. Wang, E. Masson, V. Rose, X. Li, A. T. Ngo and S.-W. Hla, *Nature*, 2023, **618**, 69–73.